INVESTIGATIONS OF GAS/ELECTRODE INTERACTIONS IN SOLID OXIDE FUEL CELLS USING VIBRATIONAL SPECTROSCOPY

A Dissertation
Presented to
The Academic Faculty

By

Harry Wilson Abernathy III

In Partial Fulfillment
Of the Requirements for the Degree
Doctor of Philosophy in Materials Science and Engineering

Georgia Institute of Technology

April 2008

INVESTIGATIONS OF GAS/ELECTRODE INTERACTIONS IN SOLID OXIDE FUEL CELLS USING VIBRATIONAL SPECTROSCOPY

Approved by:

Dr. Meilin Liu, Advisor
School of Materials Science and Engineering
Georgia Institute of Technology

Dr. Mostafa A. El-Sayed
School of Chemistry and Biochemistry
Georgia Institute of Technology

Dr. Thomas H. Sanders, Jr.
School of Materials Science and Engineering
Georgia Institute of Technology

Dr. Lane Wilson
Office of Basic Energy Sciences
US Department of Energy

Dr. Robert Speyer
School of Materials Science and Engineering
Georgia Institute of Technology

Date Approved: March 6, 2008

An experiment is a question which science poses to Nature, and a measurement is the recording of Nature's answer.

-- Max Planck

ACKNOWLEDGEMENTS

I first acknowledge the enormous debt for the work and sacrifice of my parents to help get me where I am today. Always putting their children first, they provided me with a loving environment that put the highest priority on family, education, and hard work. They taught me that the right decisions are rarely the easiest, but that anything worth doing is always worth doing right. I hope to instill these same values in my own children. I dedicate the work presented here to my mother and my father's spirit.

I would also like to acknowledge my high school chemistry teacher Mr. Tom Merritt and guidance counselor Mr. Peter Andell, who helped open my eyes to big world outside of Roanoke Rapids, NC. They encouraged me to enter a discipline that would not only stimulate me, but also allow me to educate and help others.

Most of the results in this dissertation would not have been possible without the hard work and collaboration of my fellow research group members. I would like to mention especially my officemates Erik and Chuck (now Drs. Koep and Compson), who, besides providing a large number of my samples, made sitting for years in a four person office much more tolerable. Special thanks also go to Bill, Robert, Zhe, and Dr. Choi (now Drs. Rauch, Williams, Cheng, and, well, Choi), who provided valuable scientific input as well as a healthy dose of perspective.

My advisor Dr. Meilin Liu deserves special recognition: not just for paying the bills, but also for taking a chance on me and for letting me keep at my work even after

coming into his office time and after time with often negative results. I hope the positive results that emerged only in the last few years have sufficiently rewarded his patience.

Special thanks must be given to my partner Robyn for adapting to my ever-changing work schedule and for tolerating me even when overwhelmed with her own teaching job, with taking care of our son, and with preparing for the arrival of our daughter. Finally, I want to mention my inspiration for the past two years, my son Colin Robert. Everyday he reminds me to be a better person, and I hope to one day become the father he deserves.

The research presented here was partially supported by the Department of Energy Solid State Energy Conversion Alliance, the Defense Advanced Research Projects Agency, the Office of Naval Research, and the National Science Foundation.

TABLE OF CONTENTS

LIST OF TABLES

LIST OF FIGURES

LIST OF SYMBOLS AND ABBREVIATIONS

Symbols

α	Polarizability
μ	Induced dipole
λ	Wavelength
cm^{-1}	Wavenumber
Δcm^{-1}	Raman shift

Abbreviations

CCVD	Chemical combustion vapor deposition
EDS	Energy dispersive spectroscopy
EXAFS	Extended x-ray absorption fine structure
GDC	Gadolinia-doped ceria (SOFC electrolyte)
IR	Infra red
LSC	Lanthanum strontium cobalt oxide (SOFC cathode)
LSCF	Lanthanum strontium cobalt iron oxide (SOFC cathode)
LSF	Lanthanum strontium iron oxide (SOFC cathode)
LSM	Lanthanum strontium manganese oxide (SOFC cathode)
PEMFC	Polymer electrolyte membrane fuel cell
RC	Resistor and capacitor (here, in parallel)
SDC	Scandia-doped ceria (SOFC electrolyte)
SEM	Scanning electron microscopy
SERS	Surface-enhanced Raman spectroscopy
SIMS	Secondary ion mass spectroscopy
SOFC	Solid oxide fuel cell
SSC	Strontium samarium cobalt oxide (SOFC cathode)
TERS	Tip-enhanced Raman spectroscopy
TPB	Triple phase boundary
TEM	Transmission electron microscopy
UV	Ultraviolet
YSZ	Yttria-stabilized zirconia (SOFC electrolyte)
XRD	X-ray diffractometry (or X-ray diffraction)
XPS	X-ray photoemission spectroscopy

SUMMARY

The goal of current solid oxide fuel cell (SOFC) research is to design electrode materials and other system components that permit the fuel cell to be operated in the 400-700ºC range instead of the conventional 800-1000ºC. Cell performance in this lower temperature range is limited by the oxygen reduction process at the SOFC cathode. Also, the long time performance of the cell is affected by multiple contamination processes, from Cr poisoning of the cathode from the stainless steel interconnect between individual cells in a fuel cell stack to the deposition of carbon on the anode when hydrocarbon fuels are used instead of hydrogen. Impedance spectroscopy, the *in situ* performance measurement technique of choice among fuel cell scientists, can provide a significant amount of *electrochemical* information about an operating cell; however, it is limited in the amount of specific *chemical* information it can give. The work presented here demonstrates that Raman spectroscopy, a form of vibrational spectroscopy, can provide structural and compositional information complementary to that from impedance spectroscopy and from various other *ex situ* characterization methods.

An *in situ* Raman characterization system was assembled that included a temperature- and atmosphere-controlled sample chamber that allowed for Raman measurements from an SOFC sample under a variety of conditions. Most SOFC components and possible contaminants were shown to be Raman-active with distinguishable Raman signals. Initial experiments into the oxygen reduction mechanism on SOFC cathodes were unable to detect surface oxygen species on selected perovksite-based SOFC cathode materials.

It may still be possible to increase Raman signal from surface species on these materials through surface-enhanced Raman scattering (SERS). To create a SERS effect, metal nanoparticles (usually silver or gold) were deposited onto cathode materials using either 20 nm metal colloids or combustion chemical vapor deposition (CCVD). Both methods were able to enhance the measured Raman signal from the material lattice by at least one order of magnitude. Heat treatment of the silver colloid nanoparticles caused the emergence of up to 21 previously unobserved peaks to appear in the Raman spectrum of an SSC surface. Peak assignments for these new peaks have not yet been completed.

Raman spectroscopy was able to monitor *in situ* the deposition of carbon on nickel and copper anodes. The deposited carbon was found to be amorphous, and nickel was more susceptible to carbon formation than copper.

The Cr poisoning of an LSM cathode was studied by exposing LSM to Cr-containing vapor. The vapor was generated by flowing humidified oxygen over the surface of a pellet of Cr_2O_3 powder. With 24 hrs exposure to the Cr vapor, the LSM surface had converted to $SrCrO_4$. When silver is present in the cathode, as a current collector or as catalytically-active surface, it reacts quickly with chromium to form silver chromate, Ag_2CrO_4. Silver chromate melts at 658ºC, and by 625ºC, it will volatilize and deposit preferentially on an LSM cathode surface. Since Ag_2CrO_4 contaminates both the LSM and silver surface, silver should only be used within an SOFC cathode if the leaching of Cr out of the metallic interconnect layer can be prevented.

Overall, Raman spectroscopy was shown to be useful in many areas crucial to the development of practical, cost-effective SOFCs.

CHAPTER 1: MOTIVATION

1.1 Fuel Cells and Future Energy Needs

While disagreement exists about the longevity of the world's supply of fossil fuels, the fact that there is a finite source cannot be refuted. Coupling this ultimate limitation with the ever-increasing demand for energy as the developing world strives to energy-intensive standard of living present in countries such as the United States, it is prudent – if not essential – to seek alternatives to fossil fuels whenever possible for a given application or at least to use fossil fuels as efficiently as possible. Figure 1.1 shows that two of the largest uses of energy in the United States are transportation and power generation.[1] Transportation relies almost exclusively on petroleum (and some natural gas), and almost 70% of U.S. power is generated from coal or natural gas. Advances in solar, geothermal, wind, and biomass technologies and/or a stronger commitment to nuclear power may meet the world's energy needs in the far future; however, most nations will remain heavily dependent upon fossil fuels for decades to come. As such, the onus on today's scientists and engineer is to develop and implement technologies that use fossil fuels as efficiently as possible. For current combustion-based transportation and power systems, the chemical energy in the fuel (coal, natural gas, gasoline, diesel, etc.) is transformed to thermal energy, which is then converted into mechanical energy *or* into mechanical energy *and then* into electrical energy for power. At each point in the process, there is a loss in efficiency. The goal is to remove as many conversions as possible and to increase the efficiency of the remaining steps.

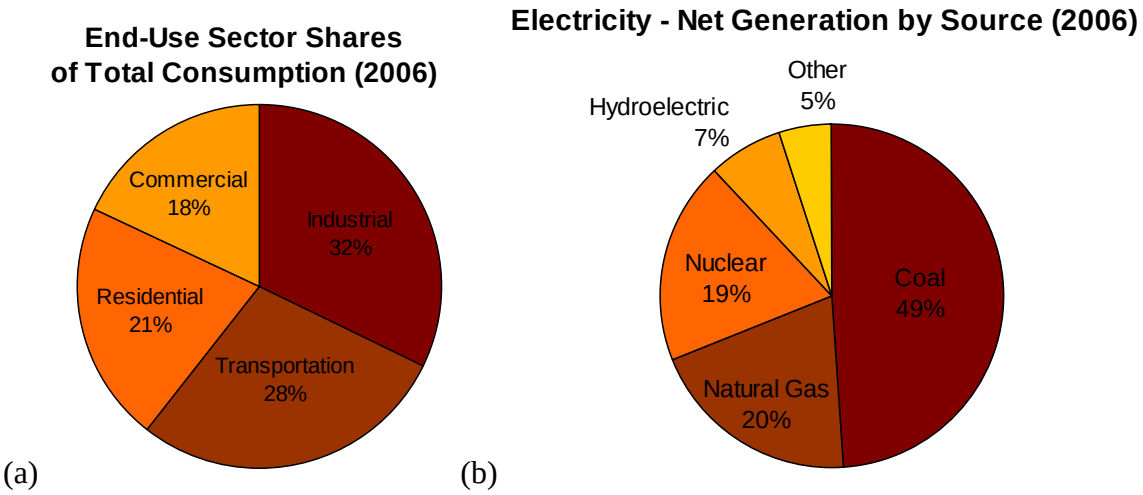

Figure 1.1. (a) Energy use by sector in the United States and (b) sources of electrical power in the United States for 2006. Statistics provided by DOE Annual Energy Review.[1]

Fuel cells have a distinct advantage over combustion-based systems in that fuel cells convert chemical energy directly into electricity. In their ability to generate electricity more efficiently than current combustion methods and to generate electricity using alternative fuel sources (hydrogen, methane, ethanol, etc.), fuel cells have been demonstrated to be part of the solution to reducing society's dependence on oil.

1.2. Background – Solid oxide fuel cells

Historically, many different fuel cell systems have been proposed, but current research mainly focuses on two: the polymer electrolyte membrane (PEM) fuel cell and the solid oxide fuel cell (SOFC).[2] The PEM fuel cell, which currently operates below 100ºC due to material constraints, is the main candidate for use in fuel cell vehicles, while the more efficient SOFC, which currently operates between 800º-1000ºC, is considered the best fuel cell system for mass stationary power generation.[3] As power

generation consumes more energy overall in the United States than transportation, the research presented in this volume is directed towards concerns with SOFC systems.

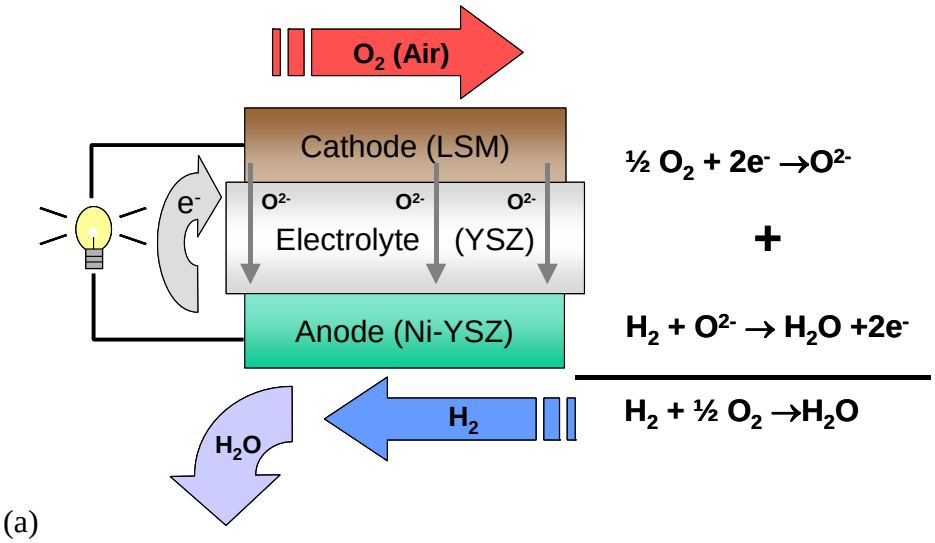

Figure 1.2. Schematic, typical materials, and electrode reactions for a solid oxide fuel cell.

Figure 1.2 shows a schematic of a typical SOFC. At the cathode, oxygen is reduced to the oxygen anion and incorporated into the lattice of the electrolyte. The oxygen ion is then conducted through the electrolyte (by necessity, an oxygen ion conductor) to the anode, where the oxygen ion combines with hydrogen to produce water and two electrons. If carbon-containing fuels such as methane or ethanol are used instead of hydrogen, the anode exhaust becomes a mixture of water and carbon dioxide. Not shown in the figure is the interconnect layer, an electronically-conductive material which rests between the cathode and anode when multiple individual fuel cells are stacked in series. The interconnect serves a two-fold purpose: (1) as a barrier between the cathode and anode of adjacent cells to avoid shorting out the fuel cell stack, and (2) as a current

collector, transporting electrons between successive cathodes and anodes and eventually to the external circuit.

The standard SOFC system, developed over twenty years ago, consists of a perovskite $La_{1-x}Sr_xMnO_3$ (LSM) cathode, a yttria-stabilized zirconia (YSZ) electrolyte, and a cermet anode comprised of a mixture of nickel and YSZ.[4] LSM is an excellent electronic conductor and YSZ a strong oxygen ion conductor in the 800º-1000ºC operating regime. The biggest obstacle in the commercialization of this system is cost. Not the cost of electrode and electrolyte materials *per se*, but rather for the interconnect materials and other balance-of-plant components, which must be exotic ceramics due to the thermal expansion requirements for operating the system at such high temperatures.[5]

1.3. Current materials issues facing SOFCs

Less expensive components, such as stainless steel interconnect layers, can be used if the SOFC could be operated in the 400º-700ºC temperature range. Unfortunately, lowering the operating temperature also lowers the cell performance, as the conductivity and catalytic activity of the electrodes and electrolyte decrease. Conductivity losses in the electrolyte have been overcome by choosing different electrolyte materials and by making the electrolyte layer thinner.[6] With an electrolyte better suited for lower operating temperatures, the limiting factor in the cell performance becomes the interfacial polarization resistance between the cathode and the electrolyte.[7] Phenomenologically, cathodic interfacial polarization involves the reduction of an oxygen molecule to the oxygen anion (O^{2-}) and its incorporation into the electrolyte (an oxygen ion conductor). Piecewise, the mechanism requires, in some order, the following processes: adsorption,

reduction, dissociation, and incorporation.[8] Since the cathode interfacial resistance limits fuel cell performance in the desired temperature range, understanding the exact oxygen reduction mechanism at the cathode – which oxygen species are present and which step in the mechanism is rate-limiting – is one of the keys to designing the optimal cathode for a low temperature SOFC. The initial driving force behind the work presented here was the desire to better understand the oxygen reduction mechanism on SOFC cathodes in order to design better cathode materials and microstructures.

Besides having a lower performance in the lower temperature regime, the cathode suffers some performance degradation when used in fuel cell stacks with stainless steel interconnect layers. Studies have found that the chromium in stainless steel leaches out and deposits throughout the cathode as Cr_2O_3 or other Cr-containing compounds (depending on the cathode material).[9] These contaminants cover the cathode surface, blocking conduction and reducing the amount of active catalytic surface available for oxygen reduction. Debate exists over which particular phases form, where they form, and whether their formation is chemically- or electrochemically-driven.[10, 11] Identifying the exact species involved and the driving forces behind their evolution aids in the material design and selection for the cathode and interconnect layer.

Cathode performance is the largest concern for low temperature SOFCs as long as hydrogen is used for the fuel; however, if carbon-containing fuels such as methane or propane are supplied to the anode, then the performance of the cell can become limited by the anode. First, as the carbon content of the fuel increases, the amount of carbon deposited on the anode increases, as not all of the carbon oxidizes to CO_2. The deposited carbon can quickly deactivate the typical nickel anode.[12] Second, when using natural gas

or coal gas as a fuel source, the anode may become poisoned over time by the presence of H_2S contaminants and lose catalytic activity.[13] Both carbon deposition and sulfur poisoning can be controlled or eliminated by treating the fuel supply. Humidifying the fuel streams reverses carbon deposition, but it can lower fuel utilization while requiring the addition of a water management system to the fuel cell stack. Desulfurizing the fuel will stop sulfur poisoning by removing the sulfur pollutant, but adding pretreatment steps to the fuel line further increases system costs. The cheaper alternative is to develop anode materials that can tolerate small amounts of H_2S in the fuel stream and are less prone to carbon deposition. To add in the evaluation of new anode materials and microstructures, fuel cell engineers seek a quick and reliable method to monitor sulfur and carbon contamination.

1.4. Conventional SOFC characterization methods and their drawbacks

All of the problems listed in the previous section involve chemical (and electro-chemical) reactions that occur during normal fuel cell operation. To evaluate the species involved in any of the reactions and to gauge the extent of the reaction, scientists rely upon a mixture of *in situ* and *ex situ* characterization methods, none of which can provide all of the desired information and all of which have significant limitations.

The most common *in situ* characterization method is impedance spectroscopy.[14] Impedance measurements are used mainly as a quantitative measure of the electrochemical performance of a fuel cell. As a fuel cell is meant to be a practical device, the current-voltage relation and/or power output of a cell is a clear objective measure of its performance. In terms of scientific data, impedance spectroscopy is also a

valuable tool, as multiple processes within a cell (surface reactions, interfacial effects, grain boundary conduction) can theoretically be separated out by measuring the frequency dependence of the impedance and fitting the impedance data using an equivalent circuit approximation.[15] For example, Figure 1.3 shows a theoretical curve impedance curve for a circuit composed of a two RC units (a resistor and capacitor placed in parallel) placed in series. The time constants (the product of the resistance and capacitance in each RC unit) of the two RC units are such that the impedance curve reveals two distinct semi-circles, or "loops". Ideally, a given sample would have processes occurring over distinct frequency ranges so that each process could be easily discerned and analyzed (i.e., the diameter of each "loop" could be quickly calculated).

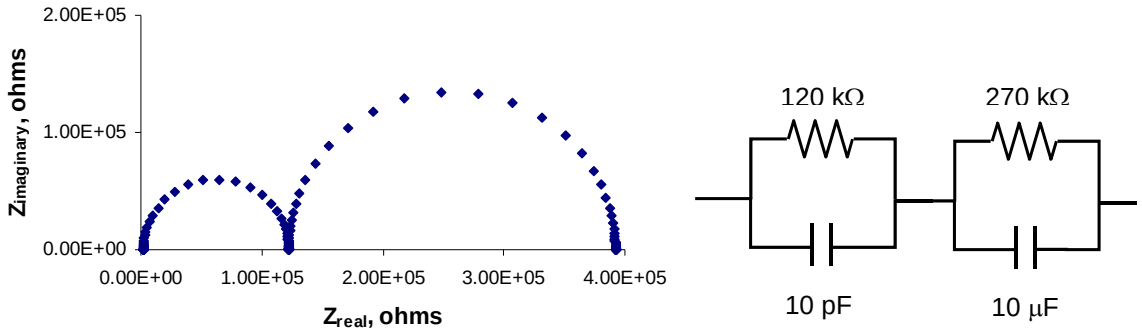

Figure 1.3. Theoretical impedance curve for the ideal circuit shown. The particular resistance and capacitance values were chosen so as to generate an impedance curve with two distinct semicircles.

Real fuel cell samples rarely give such ideal data. Figure 4 shows more typical impedance curves. These curves, measured by Koyama *et al.*, were taken from a platinum/SDC (samarium-doped ceria)/SSC ($Sm_{0.5}Sr_{0.5}CoO_3$) cell in air (P_{02}=0.2) at two different pressures (1 atm and 0.1 atm).[16] These measurements were taken to evaluate the reaction mechanism on the SSC cathode. The open circles and squares are the actual data points, and the solid lines are the theoretical loops generated through equivalent circuit

analysis to match the data. Ostensibly, the pressure-dependence of the diameters of the different loops reveals the dependence of the cathode performance on the gas phase diffusion of oxygen. The measured data is not comprised of easily separated loops. The authors assumed each curve contained three loops, and the pressure dependence of each of the three loops was analyzed. One could have just as well used two or four (or more) loops to fit the measured data, as long as one could phenomenologically rationalized the need for each loop. Further, after deciding on the number of loops, there will exist a significant error from deconvoluting the one broad impedance curve into multiple loops. Unless one is absolutely sure of what processes are occurring with a sample, interpreting impedance data and assigning specific processes to specific portions of an impedance curve can be a difficult procedure.

Also, since impedance spectroscopy is an electrochemical technique, specific reactions that are purely chemically-driven are lost within the data, attached to the nearest electrochemical step within the overall reaction mechanism. This is a major limitation when trying to solve a reaction mechanism, or at least determine a rate-limiting step within the mechanism. Chemical reactions can sometimes be monitored using impedance methods by varying the operating conditions (e.g., changing the O_2 partial pressure at the cathode); however, when other steps in the mechanism also show some variance with the same change in conditions, one is left again with trying to deconvolute complex data from non-ideal data. Thus, while impedance spectroscopy is an excellent *in situ* technique for measuring cell performance, it does not lend itself readily to exacting reaction mechanisms or identifying chemical species.

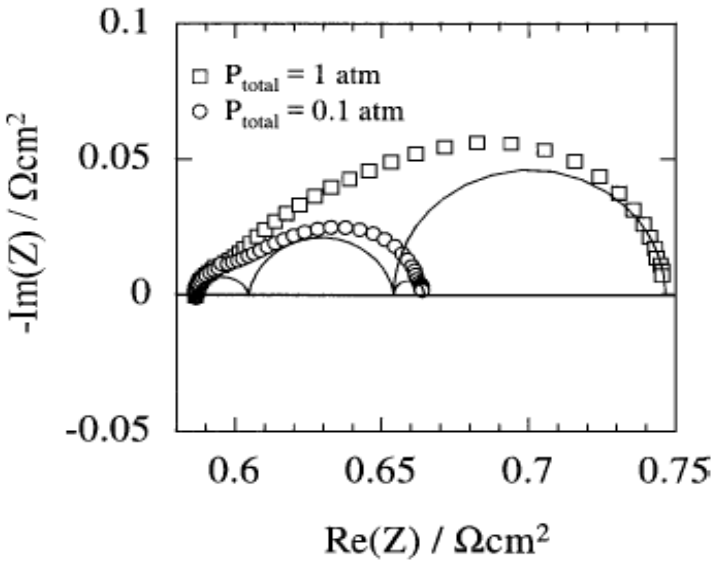

Figure 1.4. Impedance measurements from a Pt/SDC/SSC cell at different pressures. The solid lines show the theoretical loops calculated to model the impedance data. Plot reproduced from Koyama *et al.*[16]

For SOFCs, typically chemical analysis is performed *ex situ* through conventional techniques such as SEM/TEM, EDS, XPS, SIMS, and XRD. These techniques are able, to some extent, identify the chemical composition or structure of the different components of an SOFC (cathode, electrolyte, anode) and any contaminants found on the surfaces of these components. Some techniques, such as EDS, are only roughly quantitative (making it hard to positively identify specific stoichiometries) and have difficulty distinguishing some elements that are similar in atomic mass or radius. Other techniques, such as XRD, cannot easily detect trace amounts (such as monolayers) of a species, especially if it is noncrystalline. A variety of techniques usually must be combined to generate a more comprehensive picture.

A major disadvantage common to all *ex situ* techniques lies in the fact that they are *ex situ*, meaning the data obtained is not necessarily indicative of what occurs while

the cell is operating. To perform an *ex situ* measurement, the sample must be cooled down to at least room temperature and must often be placed in a high vacuum (e.g., for XPS). Any measurements are thus subject to artifacts of the cooling (and, if necessary, evacuation) process. Species present *operando* may undergo secondary reactions, decompositions, or phase changes at lower temperatures. For example, *ex situ* analysis done on the sulfur poisoning of SOFC anodes by Cheng *et al.* has revealed the presence of nickel sulfide Ni_3S_2 on nickel anodes exposed to H_2S-containing fuel.[17] However, under normal fuel cell operating temperatures, Ni_3S_2 would be a liquid, so the contaminating sulfur phase that lowers the cell performance is probably different.

A characterization method that can give chemical and structural data and can be used for *ex situ* **and** *in situ* analysis is desired. There are techniques available for *in situ* chemical analysis: EXAFS, small-angle x-ray scattering, mass spectrometry (for gas phases), FTIR spectroscopy, and Raman spectroscopy.[18] From these methods, this author believes that Raman spectroscopy, due to its (relative) ease of measurement and versatility, is the most promising technique for generating data that will complement data gained by conventional methods already used within the fuel cell community.

1.5. Research objectives and impact of research

The work presented here involves using Raman spectroscopy to analyze reactions occurring on SOFC electrodes. The objectives of this research are the following:

(1) To develop an experimental setup that would allow for *in situ* Raman spectroscopic measurements from the surfaces of SOFC electrodes;

(2) To demonstrate that Raman spectroscopy can generate specific spectroscopic data that can complement electrochemical performance data and confirm chemical analysis data obtained through other characterization methods;

(3) To use Raman spectroscopy to observe species involved in the oxygen reduction mechanism at the SOFC, so as to determine the rate-limiting step;

(4) To monitor the rate and location of carbon on SOFC anodes running on hydrocarbon fuels;

(5) To identify the identity and location of Cr-containing contaminants that form within an SOFC cathode used in conjunction with a stainless steel interconnect layer.[*]

Meeting the above objectives helps determine the individual importance of material selection, operating condition, and electrode microstructure in overcoming drawbacks associated with operating an SOFC in the 400º-700ºC temperature range. Further, the results introduce Raman spectroscopy as a viable **and** valuable characterization technique in the area of SOFCs, providing *in situ* data that has not heretofore been obtainable using standard impedance methods. The techniques presented in the following chapters can also be adapted for other high temperature catalysis applications.

[*] While sulfur poisoning was mentioned earlier as a serious concern for the anode, this volume contains no research on that particular. For a thorough analysis of this topic and of the applicability of Raman spectroscopy towards its study, please consult the thesis of my research colleague Zhe Cheng.19. Cheng, Z. Investigation into the Interactions between Sulfur and Anodes for Solid Oxide Fuel Cells. Ph.D., Georgia Institute of Technology, Atlanta, GA, 2008.

CHAPTER 2: RAMAN SPECTROSCOPY

Raman spectroscopy, like infrared spectroscopy (IR), is a form of vibrational spectroscopy, in that the bulk of the information obtained from a Raman spectrum is related to vibrational modes of a molecule or the lattice phonon modes of a crystal. There are many excellent textbooks, both science- and application-driven, that cover the history and various applications of Raman spectroscopy.[20-24] In this chapter, an introduction to the Raman scattering will be presented, along with a discussion of the applicability of Raman spectroscopy to SOFCs.

2.1. Raman scattering

Raman spectroscopy is a measurement of inelastically-scattered light. Figure 2.1 presents a simple schematic of the Raman scattering process. When light of wavelength λ strikes the surface of a sample, most of the light that is scattered is scattered elastically (i.e., at wavelength λ). This elastic scattering is called Rayleigh scattering. A small percentage of the light, typically less than 0.01%, is *inelastically* scattered at some wavelength $\lambda+\Delta\lambda$ (or $\lambda-\Delta\lambda$). The small change in energy of the inelastically, or Raman, scattered light is called the Raman shift. This change in energy corresponds to the energy required to excite a vibration or phonon mode in a molecule or crystal, respectively.

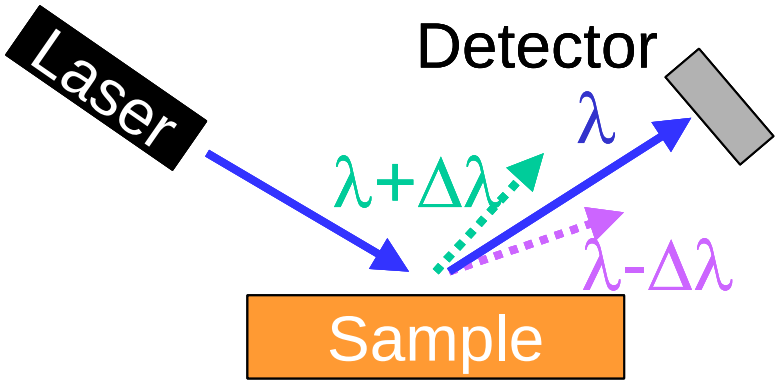

Figure 2.1. The Raman scattering process showing light inelastically scattered by the sample surface with a Stokes shift (-Δλ) and an anti-Stokes shift (+Δλ).

To generate a Raman spectrum, a sample is illuminated by a monochromatic light source (usually a laser) and the scattered light is collected, separated by energy, and read by a detector (usually a CCD). A Raman spectrum is thus a plot of the intensity of the light signal striking the detector as a function of Raman shift. By convention, the unit of Raman shift is the change in wavenumber from the incident light (Δcm^{-1}); however, most publications simply use wavenumber (cm^{-1}), with the (Δ) being implied.

The distinction between the mechanism for Raman spectroscopy and that for IR spectroscopy should be noted. For IR spectroscopy, the incident light is of the exact energy necessary, in the IR region, to excite vibration modes, and the IR detector is reading the same wavelength as the incident wavelength. For Raman spectroscopy, the incident light can be from the IR, visible, or UV region, and the detector is reading a signal near the wavelength of the incident light.

Since Raman relies upon a different mechanism to gather information about vibration modes, the selection rules for which vibration modes can be detected are different for Raman spectroscopy than for those associated with IR spectroscopy. A short

derivation is necessary to develop the selection rule. For an electric field **E** interacting with a molecule with polarizability α, the field will induce a dipole $\boldsymbol{\mu_{ind}}$ in the molecule

$$\mu_{ind} = \alpha E \tag{2.1}$$

The field associated with a light of frequency υ is given by $\mathbf{E_o cos 2\pi\upsilon t}$. Substituting this expression for **E** into (2.1) gives

$$\mu_{ind} = \alpha E_o \cos 2\pi\upsilon t \tag{2.2}$$

If the polarizability varies with position, then one can express α as $\boldsymbol{\alpha_o + (\Delta\alpha)\cos 2\pi\upsilon_o t}$. Thus (2.2) can be rewritten as

$$\mu_{ind} = (\alpha_o + (\Delta\alpha)\cos 2\pi\upsilon_o t)E_o \cos 2\pi\upsilon t \tag{2.3}$$

Using trigonometric identities, this expression expands into

$$\mu_{ind} = \alpha_o E_o \cos 2\pi\upsilon t + \tfrac{1}{2}(\Delta\alpha)E_o[\cos 2\pi(\upsilon - \upsilon_o t) + \cos 2\pi(\upsilon + \upsilon_o)t] \tag{2.4}$$

The first term in (2.4) represent Rayleigh scattering, while the second and third terms represent Stokes and anti-Stokes Raman shifts, respectively. The selection rule for Raman scattering is thus that the polarizability tensor α must change with position during a vibration, or stated mathematically

$$\frac{d\alpha}{dx} \neq 0 \tag{2.5}$$

For IR spectroscopy, the selection rule is that the induced dipole must be nonzero during a vibration. For Raman spectroscopy, the change in the material property responsible for that dipole must be nonzero during a vibration. Raman scattering can be viewed as the slight deconvolution of a light signal into frequencies υ_o, $\upsilon - \upsilon_o$, and $\upsilon + \upsilon_o$.

2.2. Determination of Raman-active modes

As the selection rules for the two methods are different, vibration modes that are observable using one method are not necessarily observable using the other. In fact, the two techniques are usually complementary, in that vibration modes that are IR-active are usually *not* Raman-active, and vice versa. A rule of thumb (i.e., true for simple geometries) is that vibration modes that are noncentrosymmetric are IR-active. If the charge distribution around the center of a vibration is not symmetric, then a noncentrosymmetric vibration will further distort the charge distribution, creating a change in dipole moment in the molecule. The rule of thumb for a Raman-active mode is that the vibration mode should be centrosymmetric. If the polarizability tensor is centrosymmetric around the center of the vibration mode, then a centrosymmetric vibration will thus elongate the tensor along the various axes, changing α during the vibration.

These general rules do not necessarily hold as the molecules (or unit cells) become larger and as the symmetry becomes lower (from cubic down to monoclinic). Some vibrations can be *both* IR- and Raman-active, while some vibrations are *neither*. While these exceptions may sound complicated, one need not fret, as group theory can be used to theoretically predict the number of possible vibration modes for a species and the activity of each of the modes. Simple group theory can be directly applied to molecules to quickly identify the number of vibration modes and which modes are Raman- or IR-active.[25] For solid materials, more complicated methods such as factor group analysis, molecular site group analysis, or nuclear site group analysis exist to predict the number and activity of normal phonon modes.[26, 27]

As an example, Figure 2.2 shows the three vibration modes for the linear molecule CO_2. Of the three modes, (a) and (b) are noncentrosymmetric and thus IR-active. Vibration mode (c), which is centrosymmetric, is Raman active.

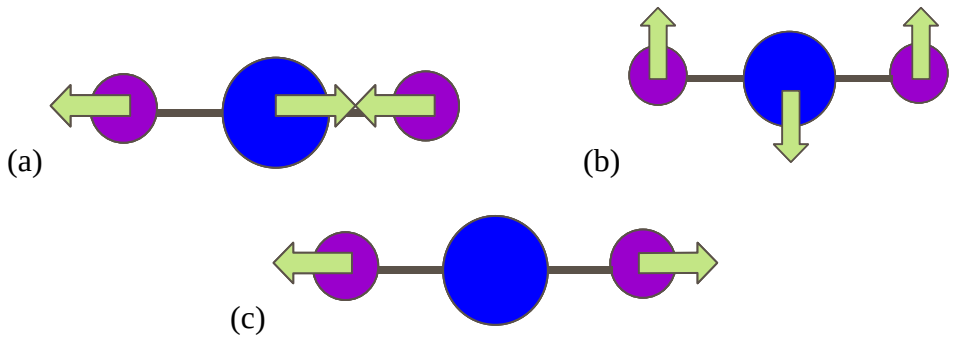

Figure 2.2. Three vibration modes of the CO_2 molecule. Blue atoms are carbon; purple atoms are oxygen.

For an example of a crystalline material, consider CeO_2, which has the fluorite structure (space group 225 – $Fm\overline{3}m$, or O^5_h). Having one molecule per Bravais lattice, and thus three ions (1 Ce^{+4}, 2 O^{2-}), CeO_2 is predicted to have 6 lattice phonon modes (calculated by multiplying the number of atoms per Bravais lattice by three and subtracting three). The cerium cation occupies Wyckoff position (a), with site symmetry O_h, while the oxygen anions occupy Wyckoff position (b), with site symmetry T_d.[28] Factor group analysis thus predicts two triply degenerate phonon modes, F_{1u} and F_{2g}, giving six total phonon modes.[27] Searching standard character tables for space groups with O_h symmetry reveals that the F_{1u} mode is IR-active and the F_{2g} mode is Raman-active.[26] One would thus expect to see only one strong (first order) Raman peak in the Raman spectrum of pure CeO_2. The Raman spectrum of CeO_2 shown in Figure 2.3 confirms this prediction, with the 462 cm^{-1} peak assigned to the F_{2g} mode.

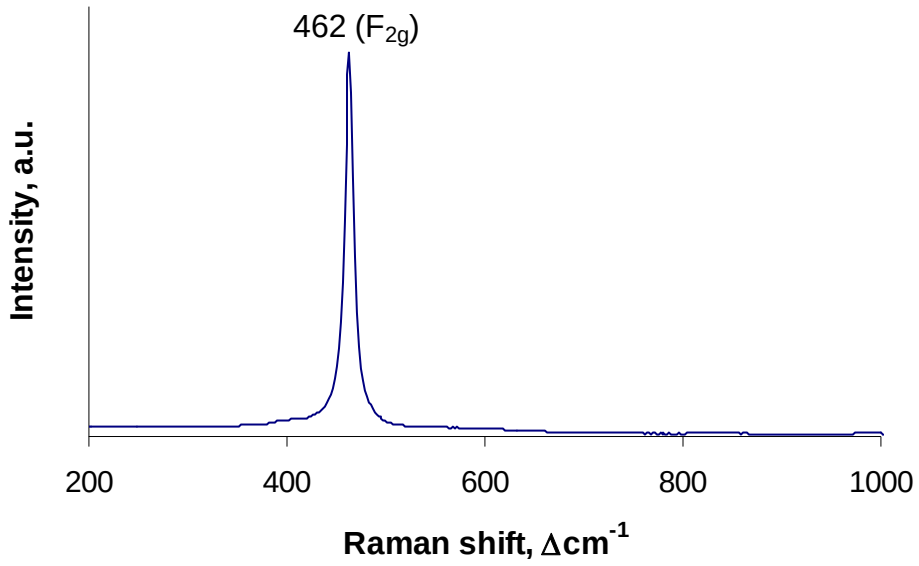

Figure 2.3. Raman spectrum of CeO_2, collected in air at room temperature using a 514 nm laser source.

It must be pointed out that group theory allows only for the determination of the theoretical number and activity of vibrational modes. In reality, the number of detected modes may differ significantly from the number predicted. There are many factors that ultimately impact the number of discernible peaks in a given spectrum, including temperature, nonstoichiometry, orientation, Raman scattering cross-section, and instrument resolution.

2.3. Raman spectroscopy and SOFCs

Before beginning an in-depth Raman study of a given system, it is necessary to ask if Raman spectroscopy can be used to analyze the desired species within the system. Although Raman spectroscopy has not been widely used to analyze SOFC components, it is not because those components are not Raman-active. In fact, a few quick measurements reveal the wide range of SOFC issues that lend themselves to Raman analysis. Figure 2.4 contains Raman spectra from two common fluorite-based SOFC electrolyte materials, YSZ and GDC. Both are strongly Raman-active, and similar to the fluorite CeO_2, both exhibit one main first order peak. The main peak for GDC, which is CeO_2 doped with 10 mol% Gd_2O_3, is close in position to that of CeO_2; however, the peak is broader and it contains a shoulder at 483 cm^{-1}, due to the presence of the gadolinium in the structures and the corresponding oxygen vacancies formed. The YSZ peak is blue-shifted (at a higher wavenumber) since zirconium is lighter than cerium. Besides peak broadening, Pomfret *et al.*, have shown that the overall spectrum intensity of YSZ can vary depending on the oxidation state of the zirconium cations on the electrolyte surface.[29] The implication of their research is that besides being a measure of stoichiometry and structure, Raman spectroscopy can be used to measure, to some degree, the surface reactivity of some common SOFC materials.

While YSZ and GDC are strongly Raman-active, many current cathode compositions based on perovskite structures are not. Figure 2.5 shows typical Raman spectra collected from five candidate cathode materials: $La_{0.6}Sr_{0.4}CoO_{3-\delta}$ (LSC), $La_{0.6}Sr_{0.4}Co_{0.2}Fe_{0.8}O_{3-\delta}$ (LSCF), $La_{0.6}Sr_{0.4}FeO_{3-\delta}$ (LSF), $Sr_{0.5}Sm_{0.5}CoO_{3-\delta}$ (SSC), and $La_{0.85}Sr_{0.15}MnO_{3-\delta}$ (LSM). All five spectra have a low signal-to-noise ratio. A perfect

cubic perovskite (space group 221 – $Pm\overline{3}m$) has no Raman-active phases, which explains the tendency for these compositions to have a weak signal.

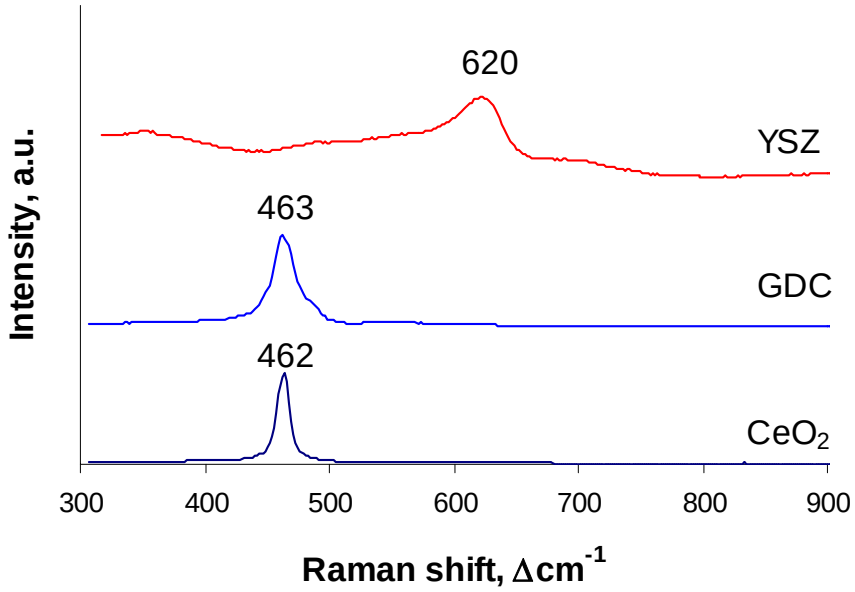

Figure 2.4. Raman spectra of fluorite-based electrolyte materials GDC and YSZ compared to CeO_2.

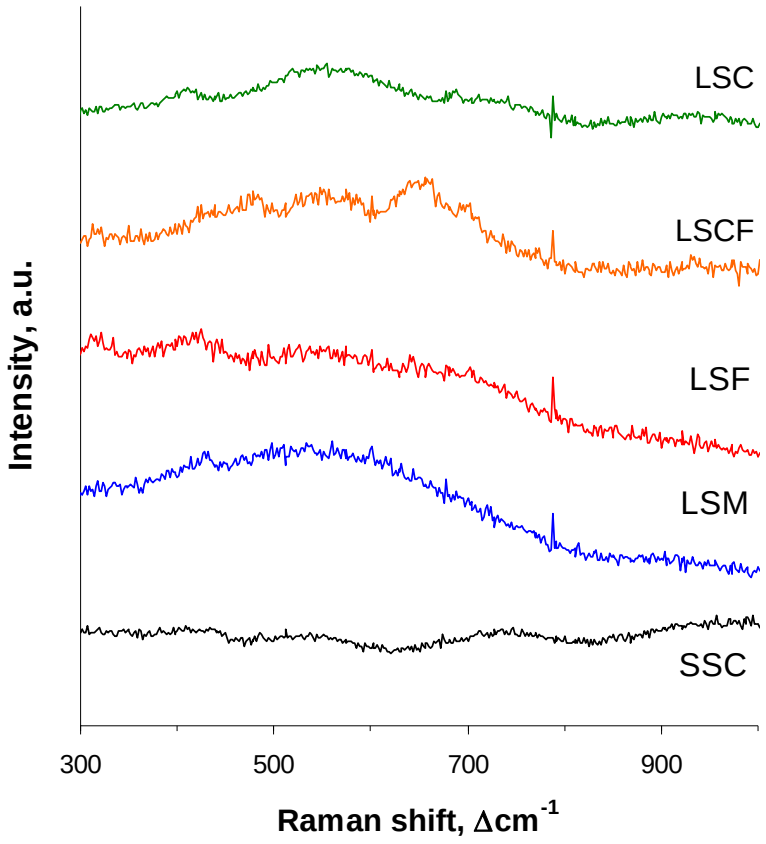

Figure 2.5. Raman spectra of candidate perovskite-based cathode materials collected in air at room temperature. SSC, LSM, and LSF are orthorhombic perovskites, while LSC and LSCF are rhombohedral.

However, of the five compositions, SSC, LSM, and LSF are orthorhombic perovskites (space group 62 – Pnma), and LSC and LSCF are rhombohedrally-distorted perovskites (space group 167 – R $\overline{3}$ c). Factor group analysis reveals that orthorhombic perovskites have 24 predicted lattice modes and rhombohedral perovskites have 5 (see Appendix A for full listing). While one would expect to see a large amount of peaks, what one observes instead are few broad signatures, although one can come close to identifying five weak, broad peaks in the LSCF spectrum. The lack of identifiable peaks in the orthorhombic-based compositions is explained by temperature effects (more numerous and sharper peaks can be observed at lower temperatures), a low Raman

scattering cross section of the base components, and a weakening of the orthorhombic distortion of the lattice brought about by defects caused by the complex composition of the material.[30-32]

The weakness of the Raman signal from candidate cathode materials is not necessarily a bad thing. Mainly, it doesn't mean that Raman analysis of cathode materials cannot be done, but rather only that longer collection times are needed to collect a satisfactory spectrum. Rough compositional analysis could still be performed on some materials, as evidenced by the Raman spectra shown in Figure 2.6 that were collected from three slightly different SSC compositions. The relative intensities of the broad peaks centered around 400 cm^{-1} and 490 cm^{-1} vary with changes in the ratio of samarium to strontium. The weak signal can also be an advantage when studying surface species and contaminants on the cathode surface, as the material offers no strong substrate signal that could possibly bury the signal from the species of interest.

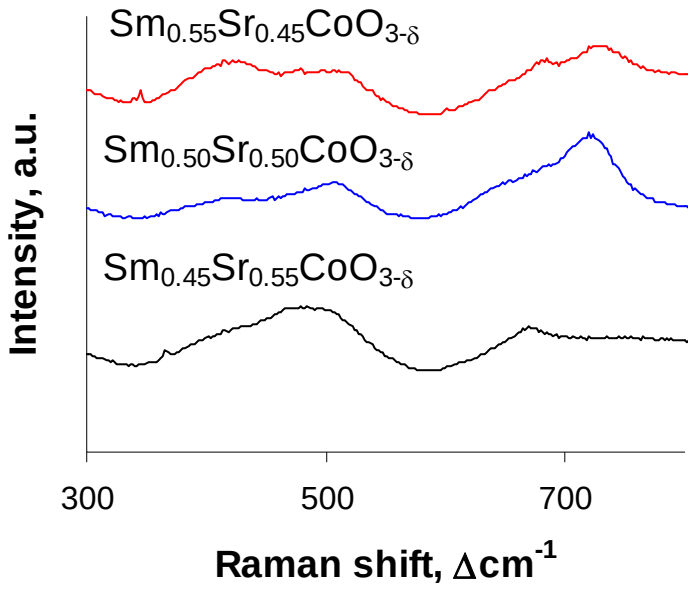

Figure 2.6. Raman spectra of various $SmCoO_3$-$SrCoO_3$ (SSC) cathode compositions**.** Spectra were collected in air using a 488 nm laser source.

Regarding the specific contamination processes being studied within this work, Raman spectroscopy is particularly useful for both the carbon and chromium studies, as compounds associated with either area are strongly Raman active. Carbon deposition on the anode lends itself readily to in situ measurements. All major carbon allotropes (diamond, graphite, graphene, carbon nanotubes, carbon black, diamondlike carbon) are all Raman-active.[33-36] Based on the presence and relative intensity of different first order and second order peaks, these phases can be distinguished from one another using Raman spectroscopy. Figure 2.7 compares representative Raman spectrum collected from highly ordered graphite compared with amorphous carbon (disordered graphite). While both phases share the 1580 cm^{-1} peak (due to sp^2 carbon bonding and often referred to as the 'G' peak), the peak around 1340 cm^{-1} in the amorphous carbon (due to sp^3 carbon bonding and often referred to as the 'D' peak) increases as graphite becomes more disordered. This disordered graphite is the primary form of carbon that forms within SOFC anodes using hydrocarbon fuels. Walker *et al*., at the University of Maryland were the first to develop and demonstrate a Raman system for studying carbon formation on nickel SOFC anodes.[37, 38]

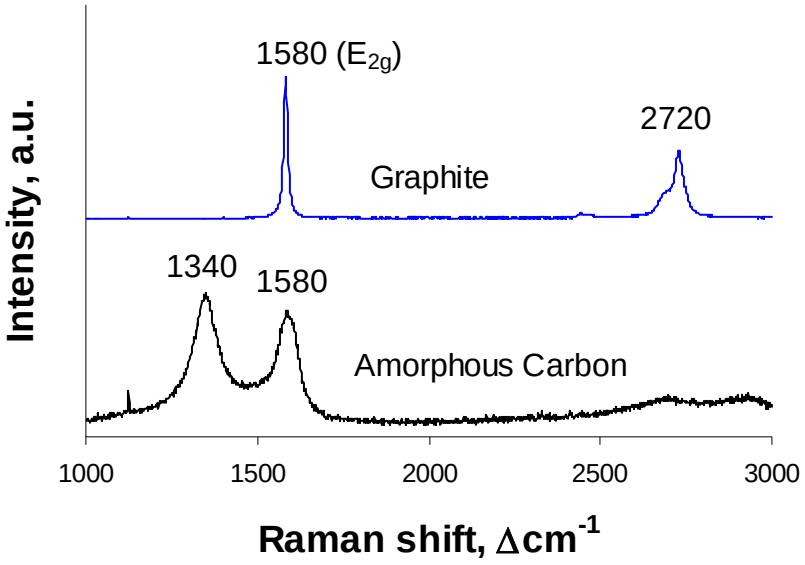

Figure 2.7. Raman spectra of amorphous carbon and graphite, two allotropes of carbon. Spectra were collected in air using a 514 nm laser source. The 1580 cm^{-1} E_{2g} is a first order peak, while the 2720 cm^{-1} is a higher order peak.

For chromium contamination, Figure 2.8 demonstrates the Raman activity and distinguishability of the expected Cr contaminant phases: Cr_2O_3, $SrCrO_4$, and the $(Mn/Cr)_3O_4$ spinel. See Appendix A for a full list of the Raman-active modes of these compounds. The $Mn_{1.5}Cr_{1.5}O_4$ sample is the composition used to generate a reference spectrum for the $(Mn/Cr)_3O_4$ spinel. Changing the relative amounts of manganese and chromium would change the width and relative intensities of the labeled peaks. While no previous Raman Cr contamination studies of these compounds have been performed on SOFCs, Raman spectroscopy has been used to monitor *in situ* the formation of Cr_2O_3 and MnCr2O4 (the spinel) scale on stainless steel.[39-41] With regard to SOFC research, Ingram *et al.*, at Argonne National Laboratory used Raman spectroscopy to confirm *ex situ* the formation of $K_2Cr_2O_7$ during their Cr contamination studies.[42] This contamination formed

as a reaction between the Cr- containing vapor being used for their experiment with a ceramic sealant being used to seal their reaction chamber.*

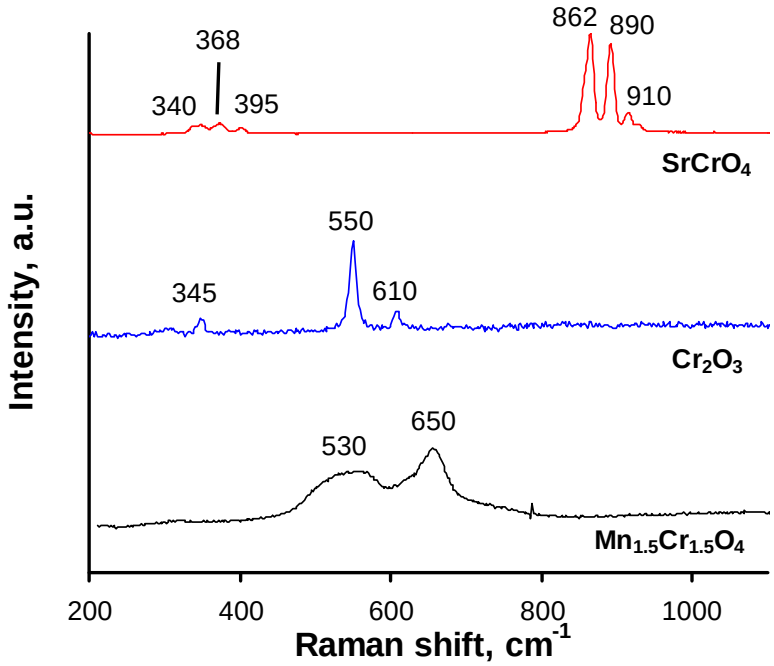

Figure 2.8. Raman spectra of typical Cr contaminants found within SOFC cathodes used in conjunction with stainless steel interconnect layers. The $Mn_{1.5}Cr_{1.5}O_4$ compound has a spinel structure.

Even though it seems like a helpful and substantive technique well-suited for SOFC applications, Raman spectroscopy is not currently popular within the SOFC community. The author is only aware of Robert Walker's research group at the

* The Acknowledgements within the Ingram *et al.* paper recognize that I was the one who took the Raman measurements for their work. The phase identification was made from a yellow film deposited on the inside of a thin quartz exhaust tube used in their experiment. Since the quartz tube is visibly transparent and since our Raman microscope uses a visible (514 nm) light source, we were able to focus on the film through the wall of the tube and perform the analysis *nondestructively*. They were able to tell me that the deposit contained potassium only because they had broken up and ground a previously-tainted tube to perform elemental analysis.

University of Maryland and Meilin Liu's research group at the Georgia Institute of Technology as being groups that regularly rely on and publish Raman analysis of SOFC components. The author hopes that the results presented in the following chapters will offer strong evidence for convincing others of its utility in this field.

CHAPTER 3: RAMAN EXPERIMENTAL SETUP

The Raman microscope used for the work presented here is part of an advanced *in situ* characterization system assembled within the Center for Innovative Fuel Cell and Battery Technologies at the Georgia Institute of Technology. The system, detailed in Figure 3.1, is allows for simultaneous chemical and electrochemical analysis of an operating fuel cell system. A temperature- and atmosphere-controlled sample chamber (special order, Harrick Scientific, *vide infra*) can be interfaced with either a Bruker Equinox55 FTIR spectrometer (in reflectance or emission mode) or a Renishaw RM 1000 Raman microscope. Inlet gas flows are controlled by electronic mass flow controllers (Porter Instrument Company), and the exhaust gas from the chamber can be circulated through either a Varian 3800 gas chromatograph or a Hiden Analytical HPR20 mass spectrometer to analyze its composition. Electrochemical measurements can be performed on the sample while simultaneously recording Raman spectra by running lead wires through holes in the quartz window covering the sample chamber. We have two available electrochemical measurement systems: (1) A Princeton Applied Research Model 273 Potentiostat/Galvanostat coupled with a Model 100 Frequency Response Detector, and (2) a Solartron 1287 Electrochemical Interface coupled with a 1255 Frequency Response Analyser. Both systems can be used to perform impedance spectroscopy or to apply a potential across a sample. This comprehensive characterization system is unique in its flexibility and ease-of-use.

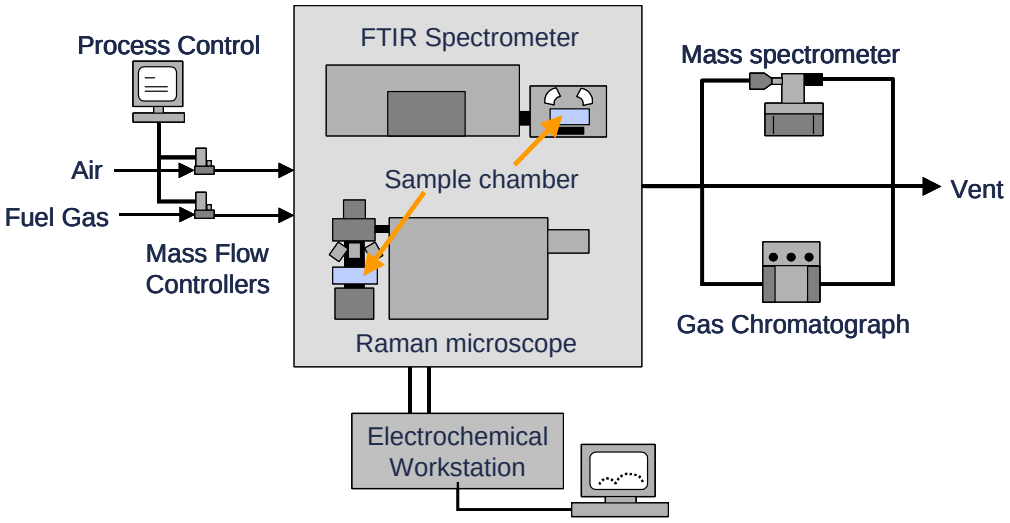

Figure 3.1. Schematic of the advanced *in situ* FTIR/Raman spectroscopy system within the Center for Innovative Fuel Cell and Battery Technologies.

3.1. Raman spectrometer

All Raman measurements were performed with the Renishaw RM 1000 Raman microscope mentioned above. The Raman microscope uses a Melles Griot 100 mW air-cooled argon-ion laser source. The spectrometer has optical filters to accommodate either the 488 nm or 514 nm line from the laser. All results presented here, unless otherwise noted, were collected using the 514 nm laserline. The Raman signal, 180º backscattered from the sample surface, is separated by a 1800 lines/mm diffraction grating and read by a thermoelectrically-cooled CCD detector.

The laser light can be focused through one of two 50X objective, depending on the experiment. For room temperature, in-air measurements a 1 mm focal length objective (0.75 numerical aperture) can be used. For measurements taken using the sample chamber, an 8 mm focal length objective (0.5 numerical aperture) must be used to accommodate the extra distance required by sample chamber cover. The longer focal

length objective could also be used for measurements performed in air; however, its lower numerical aperture lowers the amount of signal collected. Through the 50X microscope objective, the laser can be focused to a spot approximately 1 μm in diameter, giving an ideal sampling area of about 1 μm^2. The actual measured signal comes from a larger area (up to 5 μm away, depending on the species being studied) as the laser line is not always focused perfectly focused.

The sample sits upon a Prior Scientific ProScanTM motorized x-y-z stage with a 0.02 μm step size, so the sample can be moved precisely within the spatial resolution of the laser spot size. The system offers two options for generating position-dependent Raman data. For Raman mapping, a full Raman spectrum is collected from each designated point within a desired area. Depending on the time needed to record an individual spectrum, this method can be time consuming, but it generates a comprehensive picture of the desired area. The other method, Raman imaging, utilizes the global imaging configuration of the spectrometer to collect the intensity of a desired Raman shift from the area illuminated by the laser source. The Raman image is generated in the time necessary to record one spectrum, so this method is better suited for collecting quick, time-dependent data. However, there are two significant disadvantages. First, the Raman image only contains information about one particular Raman shift instead of the whole spectrum. Second, the size of the Raman image is limited to the illuminated sample area. To generate a larger image, the user must manually adjust the sample position, record another image, and paste the images together. With Raman mapping, the entire desired sample area can be selected initially and the computer will automatically adjust the motorized stage to record data outside of the current viewing area.

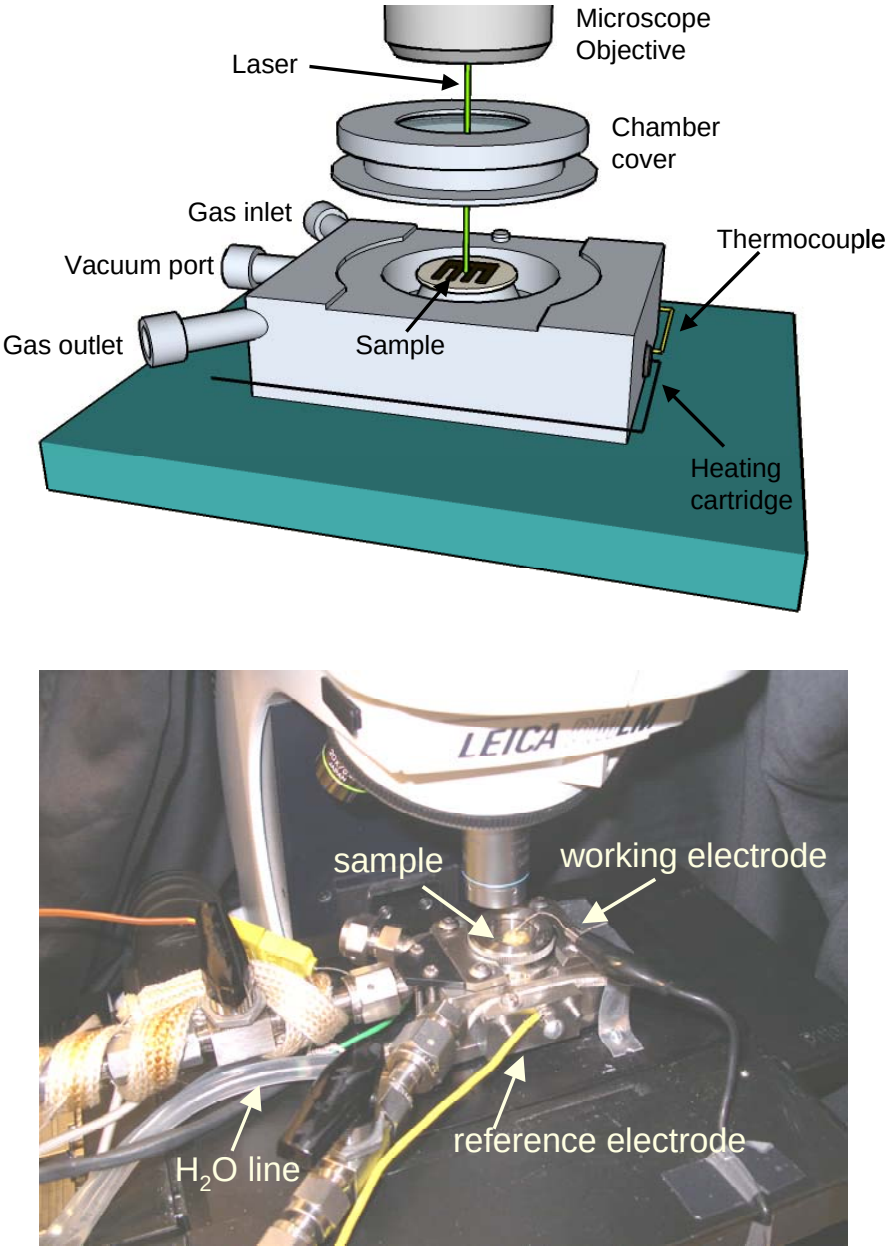

Figure 3.2. Schematic and photograph of Raman sample chamber. The photograph shows the chamber being used while a potential is being applied across the sample.

3.2. *in situ* Raman sample chamber

The Raman sample chamber, detailed in Figure 3.2 on the preceding page, is a modified version of a high temperature, low pressure, stainless steel sample chamber (HVC-DRP) made by Harrick Scientific. The maximum temperature obtainable, limited

by the heating cartridge housed under the sample cup, is currently 750ºC.* When sealed properly, the chamber can hold a vacuum of 10^{-6} torr. Originally designed for diffuse reflectance FTIR measurements, the original chamber cover was a dome with three angled IR-transparent windows for directing incoming and outgoing IR signals reflecting off the sample surface. Since our collected Raman signal is 180º backscattered off the sample surface, one horizontal, visibly-transparent window large enough to allow Raman mapping of the full sample surface was required. The screw-on top thus houses a 25x2 mm quartz window.

When polarization is required across a sample, electrical contact is made with the working electrode by running the lead wire through a small hole drilled through the quartz window using a diamond drill bit. For contact with the reference electrode there were two options. For symmetrical cells (when both sides of the sample were exposed to the same atmosphere), a small gap was left between the sample and part of the sample cup edge to run the lead wire from underneath the sample up through a second hole in the quartz window. When the reference electrode required a different atmosphere, which necessitated the sample completely cover the sample cup, the lead wire from the reference electrode was run out through the vacuum port, which opens up into the sample cup.

---

* This temperature is the temperature read from a thermocouple in contact with the heating cartridge. Since the chamber is made of stainless steel, the sample cup itself obtains a temperature close to that reading due to thermal conduction (depending on the gas flow rate through the chamber). The actual temperature on the sample surface depends on the thickness and thermal conductivity of a particular sample. As most of our samples were ceramic, this temperature difference was significant, varying from 50-150ºC from the cartridge temperature. Sample temperatures reported were obtained from a calibration curve generated from measuring the temperature of a thermocouple in direct contact with the surface of a sample YSZ pellet.

3.3. Raman mapping samples

Besides identifying *which* species are present on the electrode surface, another main goal is to discover *where* these species form. More specific than the overall electrode surface, it is desirable to probe general sample locations (e.g., near the gas inlet/outlet) as well as specific geometries (e.g., the triple phase boundary, or TPB, between the electrolyte, electrode, and gas phase). To this end, the motorized sample stage is used in conjunction with Raman microscope to produce maps detailing the intensity of a chosen Raman signal as a function of position. Due to the illumination area of the laser when focused through the available 50x objective, a generated map's resolution cannot be finer than 1 μm^2. Further, experimentation has revealed that a slight Raman signal can be detected from strong Raman scatterers from up to 5 μm away from the center of laser spot. Thus, samples should be designed such that particular locations of interest are located at least 5 μm away from other areas of interest to obtain cleaner data.

Two types of samples are used for the mapping experiments. The first type of sample, shown in Figure 3.3(a), is a dense pellet composed of a mixture of an electrolyte with the chosen electrode material. Each phase is made from polycrystalline particles with average diameters greater than 10 μm. The large particle size allows for the adequate separation of the signal from the TPB from that of the interior of the particle. The second type of Raman mapping sample consists of a cell made from a YSZ substrate with a painted metallic electrode on one side and a micropatterned electrode of the desired cathode material on the other side, as shown in Figure 3.3(b). The patterned electrode is deposited through standard lithographic techniques.[43-46] The widths of the

electrodes and the distances between the electrodes are on the order of 10 and 50 μm due to the resolution of the microscope.*

The composite samples can be made for any electrode material and can be used for experiments performed in different atmospheres and at different temperatures. The patterned electrodes can be used in these types of experiments, too, but they have the added flexibility of allowing a potential to be easily applied to the sample during the measurement. But while the patterned electrodes are more versatile, they are also more time consuming and expensive to fabricate, as they require access to a clean room and a sputtering target must be produced for each material to be deposited.

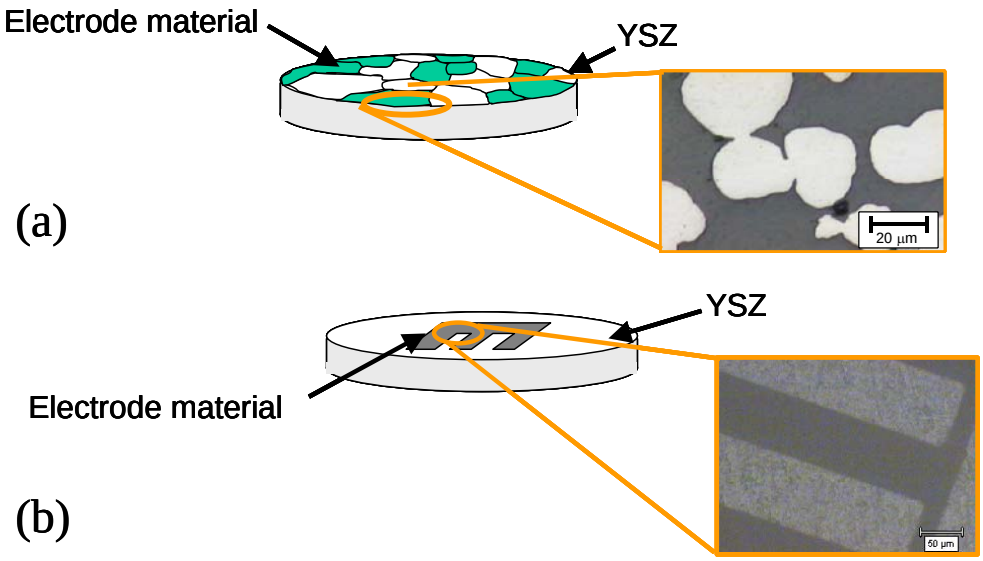

Figure 3.3. (a) Composite and (b) micropatterned electrode samples used for Raman mapping measurements. The electrode strips pictured in (b) are 50 μm wide.

* All micropatterned samples were fabricated by my colleague Dr. Erik Koep. For a better demonstration of the possible resolution of these techniques and the scientific merit of such samples, please see his publications and doctoral thesis.[43-46]

CHAPTER 4: RAMAN SPECTROSCOPY OF SURFACE OXYGEN

Overall SOFC performance in the intermediate temperature range (400-700ºC) is limited by the interfacial polarization resistance between the cathode and the electrolyte. Rational development of better SOFC cathodes thus relies upon a thorough understanding of the oxygen reduction process happening on the cathode surface. Direct spectroscopic observation of the species involved in this process would help identify the rate-limiting step and indicate what characteristics of the cathode must be improved, be it microstructure or electrode composition. The work in this chapter represents the efforts spent trying to observe surface oxygen species on the common cathode materials. Raman measurements were made first upon a model material, CeO_2, to compare experimental data with theoretical values predicted using quantum chemical calculations. Next, similar calculations and measurements were made for selected cathode materials.

4.1. Mixed conducting cathodes and the oxygen reduction process

Phenomenologically, cathodic interfacial polarization involves the reduction of an oxygen molecule to the oxygen anion (O^{2-}) and its incorporation into the electrolyte. Piecewise, the mechanism requires, in some order, the following processes: adsorption, reduction, dissociation, and incorporation. Figure 4.1 details different possible reduction mechanisms depending on whether the adsorbed oxygen molecules first dissociates or reduces. Debate exists over the exact order and nature of the rate-limiting factor.[8, 47-51]

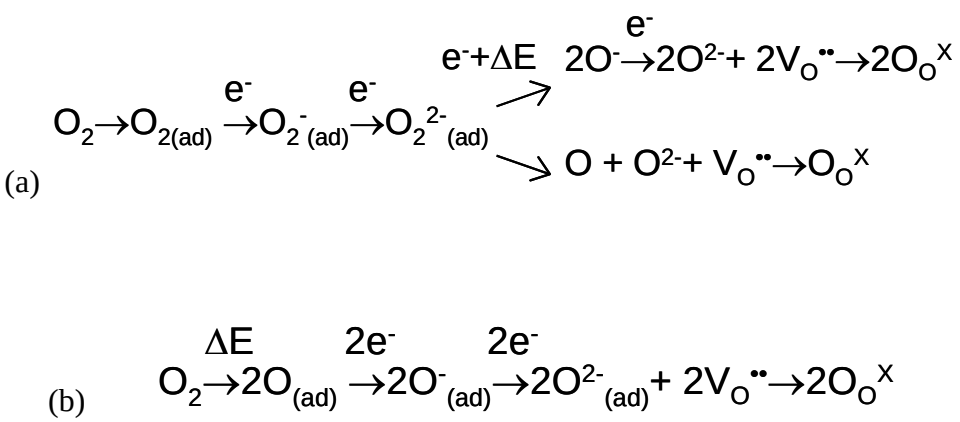

Figure 4.1. Possible oxygen reduction mechanisms occurring on the SOFC cathode in which (a) the oxygen molecule is reduced before dissociating or (b) the oxygen molecule dissociates before being reduced.

To improve cathode performance, one must first understand what exact processes occur at the cathode. Using Kroger-Vink notation[52], the overall cathode reaction can be summarized as

$$\tfrac{1}{2}O_2 + 2e' + V_O^{\bullet\bullet} \rightarrow O_O^X \tag{4.1}$$

in which an oxygen molecule is reduced by two electrons and incorporated into an oxygen vacancy in the lattice. If using a standard electronically-conductive cathode material, then the three reactants must by provided by three separate phases: electrons from the cathode, oxygen from the gas, and oxygen vacancies from the electrolyte. The intersection of these three phases is called the triple phase boundary (TPB) and has been known historically to be important for most forms of electrocatalysis.[53] Figure 4.1 shows a schematic of an SOFC cathode indicating the various two- and three-phase interfaces. Limiting the reaction to the TPB (region 3 in Fig. 4.1) eliminates the majority of available surface area at the cathode area. Extending the catalytically active area to

include surfaces away from the TPB would increase the cathode performance and thus allow the SOFC to operate at lower temperatures. To this effect, scientists have begun focusing on cathode materials that conduct not only electrons, but also oxygen ions – so-called mixed ionic electronic conductors (MIECs). The added ionic conductivity allows for the oxygen molecule to be reduced on the cathode surface and incorporated into the cathode lattice (regions 1 and 2 in Fig. 4.1) before being transported through the cathode to the electrolyte.

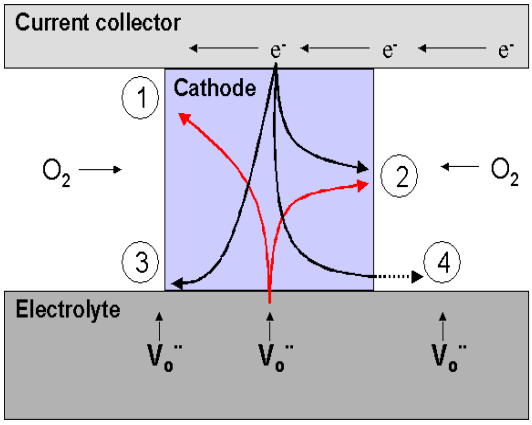

1. Gas / Electrode / Current collector
2. Gas / Electrode
3. Gas / Electrode / Electrolyte
4. Gas / Electrode

Figure 4.2. Various interfaces on an SOFC cathode. For fuel cell stacks, the interconnect material acts as the current collector.

Over the last 15 years, scientists have developed MIEC cathode materials such as $La_{1-x}Sr_xCoO_{3-\delta}$ (LSC), $La_{1-x}Sr_xFeoO_{3-\delta}$ (LSF), $La_{1-x}Sr_xCo_{0.2}Fe_{0.8}O_{3-\delta}$ (LSCF) and $Sr_{0.5}Sm_{0.5}CoO_{3-\delta}$ (SSC) that exhibit a significant amount of mixed conduction even below 600ºC.[48, 54-57] However, even with the mixed conduction in these materials, the interfacial resistance at the cathode is still the limiting factor in SOFC performance at lower operating temperatures.[7] To help discover the root of this problem, thorough theoretical analysis has been performed to model SOFC performance using MIEC cathode

materials.[15, 58, 59] The mixed conduction adds another level of complexity to the oxygen reduction mechanism described earlier. The adsorption, dissociation, and reduction of oxygen now occur at multiple locations on the cathode, and diffusion over the surface and through the bulk of the cathode must now also be considered.

4.2. Observing surface oxygen using Raman spectroscopy

Like IR spectroscopy, Raman spectroscopy has a history going back to the 1970's of being used to observe surface species and thin surface layers.[24, 60, 61] Typical surface contaminants like hydroxyl groups and carbonates are readily seen on most samples.[62, 63] With adequate surface cleaning and a controlled atmosphere, many other surface species can be observed: sulfur (thiols and sulfides), hydrogen (and hydrides), CO (and COOH), O_2 (and various reduced oxygen species), and NO_x.[24, 64-70] With regards to SOFCs, while no work has reported demonstrating oxygen on the surface of current candidate cathode materials, peroxide species have been located on the surface of a composite between silver and $La_{0.6}Sr_{0.4}MnO_3$ composite, a perovskite similar in composition to the standard $La_{0.85}Sr_{0.15}MnO_3$ (LSM) cathode.[71]

Like all forms of surface analysis, the key to getting a strong surface signal is the surface treatment method and the measurement conditions. Surface groups like hydroxyls and carbonates are very tenacious and must be removed through a suitable combination of heating, purging, and evacuation, or these groups will cover the sample surface and reduce the signal from the desired surface species. Temperature also plays an important role in observing surface species, as adsorbed and weakly-bonded species have a greater tendency to desorb as the temperature increases.[62] The greatest chance of success for

surface Raman measurements is at low temperatures in a well-controlled atmosphere. The ability to make high temperature *in situ* measurements is thus limited to the temperature range within which the signal for the desired surface species is strong enough to be discernible above the background.

4.3 Surface oxygen species on CeO_2

Before turning to SOFC cathode materials, it is helpful to turn to a material – in this case, cerium oxide CeO_2 – for which there exists some literature demonstrating the ability to observe surface oxygen using Raman spectroscopy.[62, 72-75] Ceria is a good test material for many reasons: (1) it's the base material for GDC, a leading low temperature electrolyte candidate material, (2) some research group are incorporating CeO_2 as an ionically- conducting ceramic phase for a cermet-based anode, and (3) its fluorite structure (with no dopants) is easy to simulate when doing test quantum chemical calculations to verify peak assignments in measured Raman spectra.[76-80]

Two microstructures of CeO2 were examined: (1) CeO_2 "microflowers", a unique microstructure with ~100 m^2/g specific surface area created by group member Yuelan Zhang using a hydrothermal process shown in Figure 4.3),[81, 82] and (2) CeO_2 nanoparticles of comparable specific surface area purchased from Sigma-Aldrich. The two samples were chosen to evaluate how morphology affects the types of oxygen species observed on the sample surface.

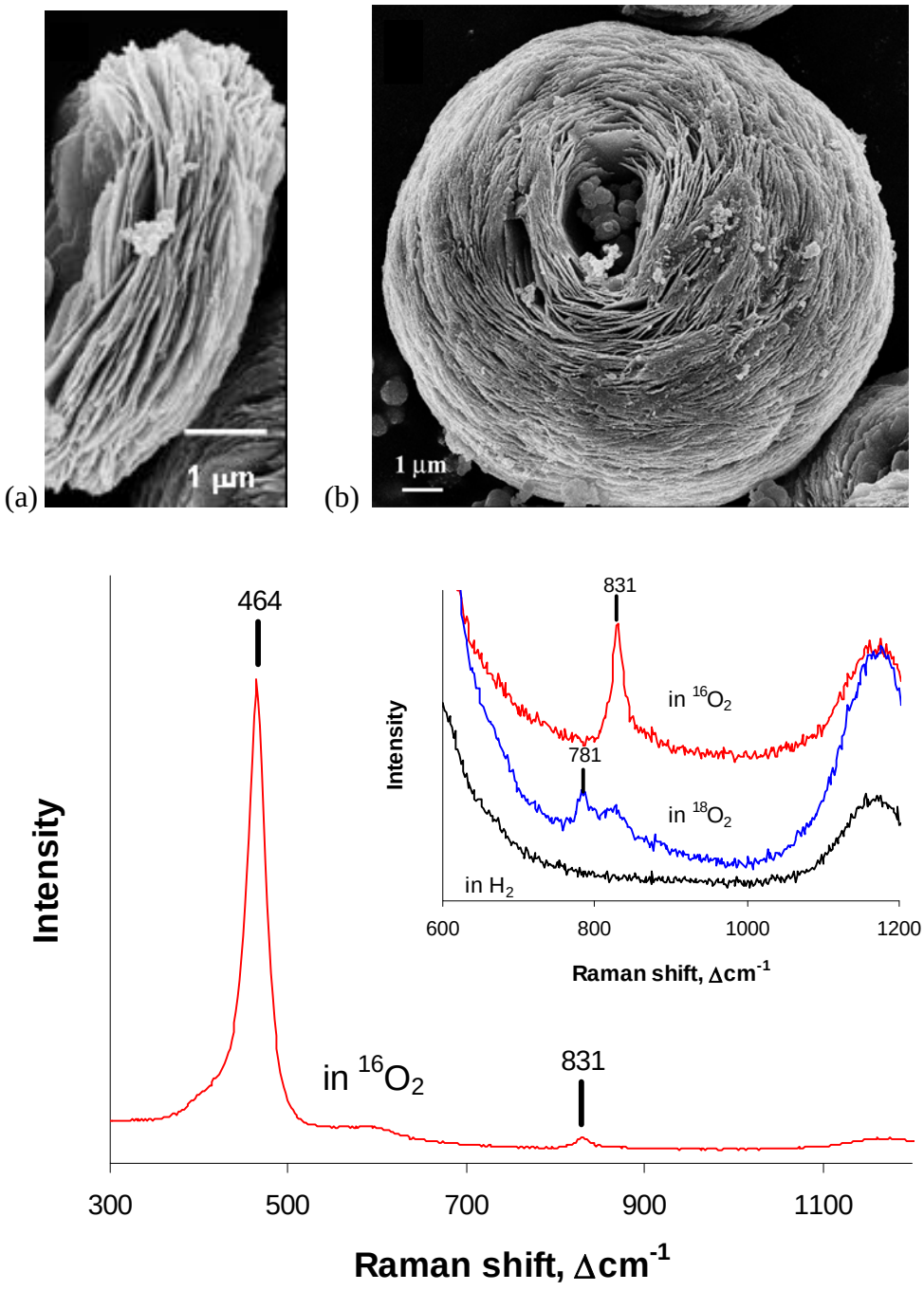

Figure 4.3. (a),(b) SEM images of ceria "microflowers". (c) Room temperature Raman spectra of microflowers collected after reduction in 10% H_2 at 425ºC and subsequent exposure to $^{16}O_2$ and then $^{18}O_2$. Micrographs reprinted from Zhang *et al.*[81]

The powders were pressed into a dry 10 mm diameter pellet and placed separately within the Raman sample chamber. Two surface treatments were used to remove unwanted species from the surface: (1) Evacuation at 50ºC for 4 hrs and (2) Reduction in 5% H_2 (balance argon) for 4 hrs at 400ºC. For ceria, both methods were found to sufficiently clean the surface. Raman spectra were then collected at room temperature from the cleaned surface before and after exposure to $^{16}O_2$. Typical spectra from the microflowers are shown in Figure 4.3(c). While the F_{2g} peak at 464 cm^{-1} (discussed in Chapter 2) is the prominent feature, closer examination between 800 and 1200 cm^{-1} reveals a peak at 831 cm^{-1} that emerged upon exposure to oxygen. To confirm that this peak was indeed from a biatomic oxygen species, the sample was exposed to the heavier isotope $^{18}O_2$ (95% $^{18}O_2$/5% $^{16}O_2$), which caused the 831 cm^{-1} peak to weaken and shift to 781 cm^{-1}. The ratio of these two peaks (831/781 = 1.06) is equal to the anticipated shift in peak position due to the mass difference of a species only containing two oxygen atoms ($\sqrt{\frac{m_{18-O2}}{m_{16-O2}}} = \sqrt{\frac{36}{32}} = 1.06$). Thus, the 831 cm^{-1} peak can be assigned to an O_2 species.

The nanoparticles also exhibited the 831 cm^{-1} peak upon oxygen exposure; however, another peak at 1128 cm^{-1} was also observed (see Figure 4.4). $^{18}O_2$/$^{16}O_2$ isotope exchange confirmed that this peak was also an O_2 species. The presence of these peaks is consistent with previously reported studies that assigned the 831 cm^{-1} and 1128 cm^{-1} peak to peroxo-like and superoxo-like reduced oxygen species, respectively.[62, 69] The assignments do not equate to an exact charge of –1 (superoxide) and –2 (peroxide); they only indicate that the 831 cm^{-1} species is more negatively charged than the 1128 cm^{-1} species, itself more negative than molecular oxygen (which vibrates at 1550 cm^{-1})

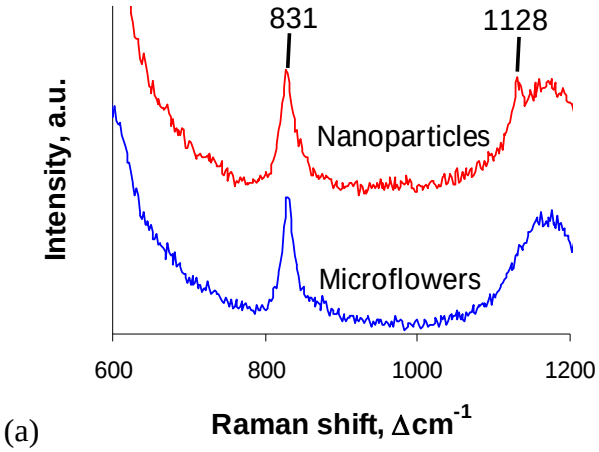

(a)

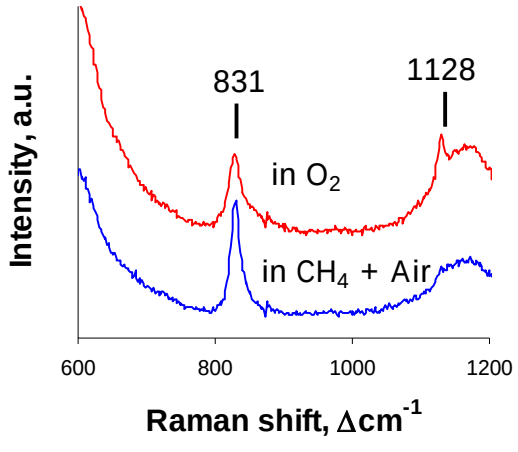

(b)

Figure 4.4. (a) Comparison of Raman spectra, in $^{16}O_2$,of microflowers with nanoparticles of similar specific surface area. (b) Raman spectrum showing loss of 1128 cm^{-1} superoxide peak from nanoparticle after exposure to mixture of air and CH_4.

To learn more about the nature of these oxygen species, a postdoctoral research associate within the author's research group, Dr. Yongman Choi, used DFT models to analyze possible structures for oxygen species adsorbed on a CeO_2 (111) surface.[83] The (111) surface was chosen because it had been previously shown to be the most energetically stable exposed surface for CeO_2.[84] To simulate the reduced CeO_2 structure, vacancies were added to the model slab, as the negative point defects created from

reducing a Ce^{+4} lattice sites are usually compensated by the creation of oxygen vacancies, a positively-charged point defect. Many possible conformations, with different adsorption energies, were calculated. The predicted vibrational frequencies of the different oxygen species did not match exactly the experimentally-observed values; however, two classes of species could be observed. One grouping had predicted vibration modes between 1100 and 1300 cm^{-1}, while another had values clustering between 900 and 1000 cm^{-1}. Since reliable correction factors to correlate theoretical and experimental values do not exist for CeO_2, an assignment of one particular theoretical arrangement to each peak could not be made. Instead, the 831 cm^{-1} peroxo-like species was concluded to be one of the species from the 900-1000 cm^{-1} group, while the superoxo-species was said to belong to the 1100-1300 cm^{-1} group. Figure 4.5 gives an example of a species from each class, along with its associated adsorption energy. The adsorption energy was calculated as the difference between the energy of the bonded state and the energy of the CeO_2 surface and free oxygen. The greater adsorption energy of the peroxo-like species reflects stronger, more stable bonding with the CeO_2, which is to be expected as the oxygen molecule draws more charge from the surface as it reduces.

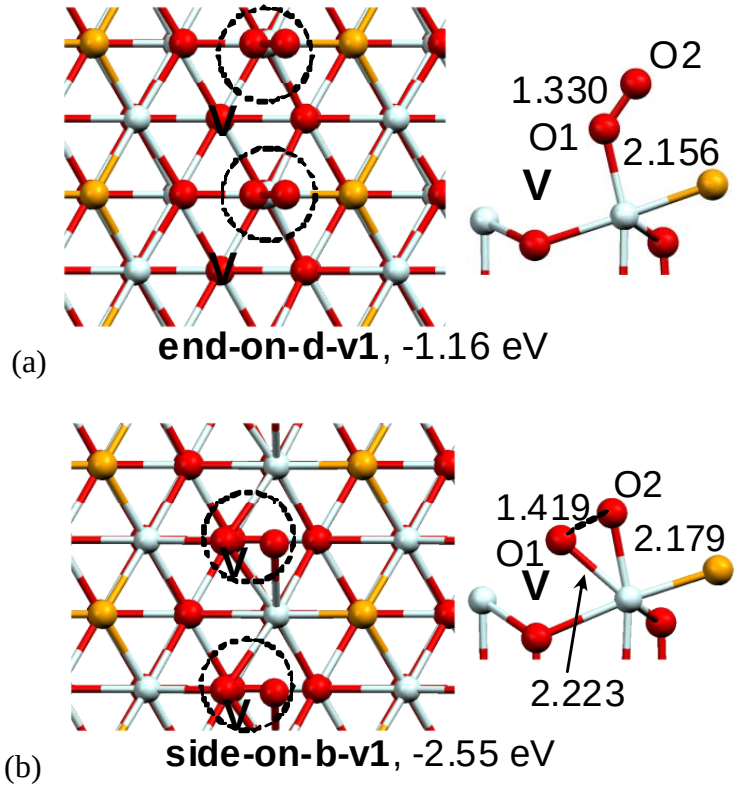

Figure 4.5. Geometric illustration of possible (a) superoxo- and (b) peroxo- arrangements of O_2 adsorbed on a reduced CeO2 (111) surface. 'V' indicates an oxygen vacancy. The reported adsorption energies were predicted using DFT calculations. Images reprinted from Choi *et al.*[83]

The abundance of available surface oxygen on ceria has led some scientists to use it as an oxidative catalyst. This is one reason why it has been considered for inclusion in SOFC anodes to help oxidize hydrocarbon fuels. As shown in Figure 4.4(b), the Raman spectrum of the CeO_2 nanoparticles was recorded during exposure to a mixture of 10% CH_4 in air. The superoxide peak decreases significantly while the peroxide peak remains strong. This selective response indicates that the less-tightly bound superoxide species is the species involved in oxidation of the methane. Thus, measurement of the 1128 cm^{-1} peak intensity can be used to gauge the effectiveness of CeO_2 catalyze towards the oxidation of methane. Such a rubrick leads to the conclusion that the synthesized microflowers would be less effective than nanoparticles with similar specific surface

area. TEM electron diffraction from the faces of the "petals" of the microflowers revealed a (100) orientation, while the nanoparticles showed a preference for the (111) face. One can infer that the (100) face is less reactive to oxygen reduction than the more stable (111) face. More DFT calculations could deny or confirm this conclusion by calculating the adsorption energies of oxygen on the (100) face and comparing them with those already calculated for (111).

It should be clarified that leak of a discernible signal at 1128 cm^{-1} does not mean that species is not present on the CeO_2 surface. Rather, if any of that superoxo-like species were present, then the concentration was so low that its Raman signal could not be adequately detected above the spectrum background. One could rationally assume that some equilibrium must exist between the superoxide and peroxide species, as the oxygen must go through the former state to get to the latter. The relative surface energy of the (100) is apparently high enough to push that equilibrium more towards the more strongly bound peroxide species.

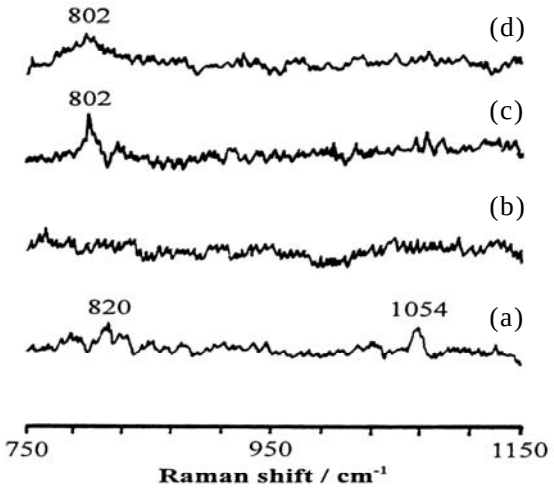

Figure 4.6. Raman spectrum of $La_{0.6}Sr_{0.4}MnO_3$ collected at (a) 25ºC in air, (b) 90ºC in a 0.2%/1.0%/98.8% mixture of $CH_3OH/O_2/N_2$; and of a 6% Ag / $La_{0.6}Sr_{0.4}MnO_3$ composite in a 0.2%/1.0%/98.8% mixture of $CH_3OH/O_2/N_2$ mixture at (c) 25ºC and (3) 50ºC. Spectra reprinted from Wang *et al.*[71]

4.3. Surface oxygen on SOFC cathode materials

With surface oxygen measurements thus being demonstrated with the assembled Raman system, attention is turned back towards observing surface oxygen on SOFC cathode materials. As stated previously, Wang *et al*. claimed to have detected oxygen from the surface of a $La_{0.6}Sr_{0.4}MnO_3$ / Ag composite.[71] Their data is shown in Figure 4.6. Spectra 4.6 (c) and (d) show a peak at 802 cm^{-1}, which they attribute to a peroxide species. The LSM used for a conventional SOFC cathode is either $La_{0.8}Sr_{0.2}MnO_3$ or $La_{0.85}Sr_{0.15}MnO_3$. The difference in composition from that used by Wang is significant because with the greater amount strontium, the $La_{0.6}Sr_{0.4}MnO_3$ composition is a rhombohedrally-distorted perovskite (as is $SrMnO_3$) and not the orthorhombically-distorted structure of $La_{0.85}Sr_{0.15}MnO_3$. Changing the structure can change the properties; however, one can consider that some candidate cathode materials (e.g., LSC and LSCF) are also rhombohedral perovskites.

As done with CeO_2 in the previous section, DFT calculations were performed on a model $La_{0.5}Sr_{0.5}MnO_3$ structure to find stable arrangements of oxygen adsorbed on the LSM surface and to predict the vibrational frequency of the adsorbed oxygen molecule. The 50:50 La:Sr composition was chosen due to the size of the model slab. To generate a 85:15 La:Sr composition, the slab would have had to be made larger, which would significantly increase the computational time necessary. The results of these calculations are summarized in Figure 4.7 and Table 4.1.

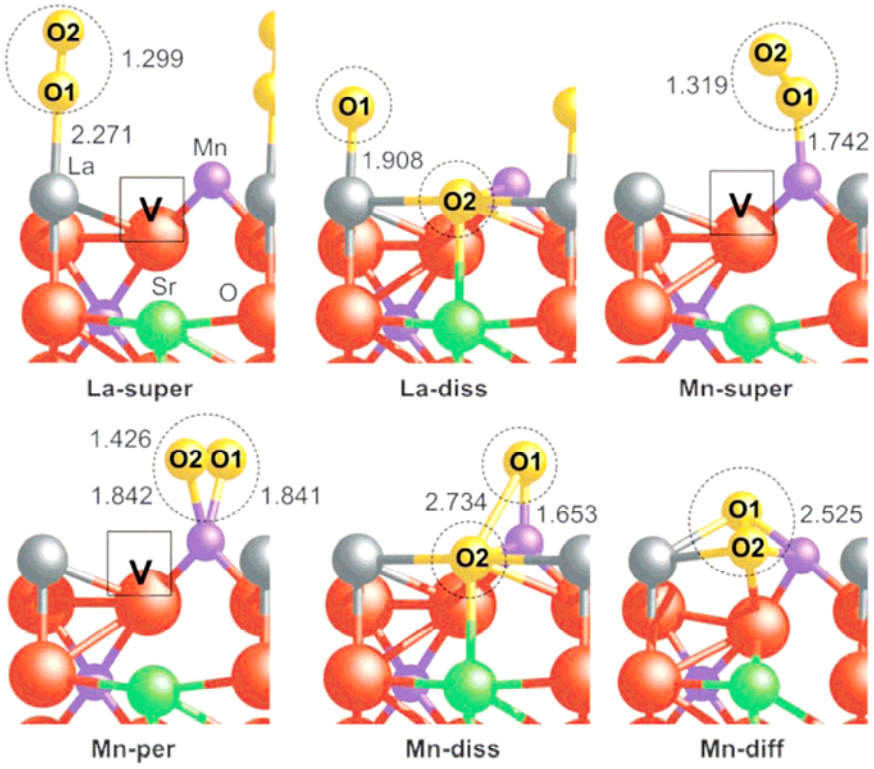

Figure 4.7. Structural representation of optimized oxygen species on $La_{0.5}Sr_{0.5}MnO_3$ via molecular adsorption. The species in dashed circles are adsorbed oxygen species. V denotes an oxygen vacancy. Figure reproduced from Choi *et al.*[85]

Table 4.1. Adsorption energies, bond lengths, and vibrational frequencies of adsorbed oxygen species on $La_{0.5}Sr_{0.5}MnO_3$ (LSM0.5). Table values reprinted from Choi *et al.*[85]

SPECIES	**ΔE, eV**	**r(O-O), Å**	**r(O-M), Å**	**ν_{O-O}, cm^{-1}**	**Remark**
LSM0.5 + O_2	0.00	—	—	—	—
O_2	—	1.235	—	1558	—
La-super	-1.10	1.299	2.271	1218	superoxo
La-diss	-5.20	—	1.908	—	—
Mn-super	-1.93	1.319	1.742	1182	superoxo
Mn-per	-2.79	1.426	1.842	909	peroxo
Mn-diss	-6.69	—	1.653	—	—
Mn-diff*	-8.47	—	—	—	—

* Final product in the mechanistic study

The arrangements in Fig. 4.7 show the possibility of both superoxo- and peroxo-like species bound to either lanthanum or manganese cations, with manganese being energetically favored, as evidenced by the adsorption energies calculated in Table 4.1. There is also a strong driving force for the dissociated states (**La-diss** and **Mn-diss**), meaning equilibrium may be shifted away from the reduced molecular species in favor of dissociated oxygen atoms. Nonetheless, supposedly stable arrangements should theoretically exist, with vibrational frequencies between 800 and 1200 cm^{-1}.

Initial Raman measurements do not reveal any such peaks. Test pellets of the model $La_{0.5}Sr_{0.5}MnO_3$ composition were pressed from powders made using the glycine-nitrate process (GNP). This process was used, as opposed to traditional solid state techniques, because the GNP is excellent at making complex compositions and it makes very fine powders with high specific surface area.[86] A high surface area powder was used to increase the specific concentration of surface species within the area illuminated by the Raman laser. To clean the surface, the pellet was evacuated to 10^{-3} torr for up to 12 hrs at either 200ºC, 350ºC, 500ºC, and 625ºC. Evacuation was chosen as a surface cleaning method in lieu of exposure to hydrogen due to the instability of the desired cathode materials in a reducing environment. The lower evacuation temperatures were attempted first, so as to reduce the chance of sintering or any secondary reactions inside the sample chamber. The evacuated samples were then cooled to room temperature and exposed to 10% $^{16}O_2$ (balance argon) or 10% $^{18}O_2$ (balance argon). Figure 4.8 shows that even with evacuation at 625ºC, no new peaks emerge when the treated surface is exposed to oxygen. The peaks indicated in the figure are from the bulk of the sample. As such, the surface treatment did not appear to noticeably change the powder, as the spectrum of the

evacuated powder matches that of the as-received powder (see Appendix B for reference spectra).

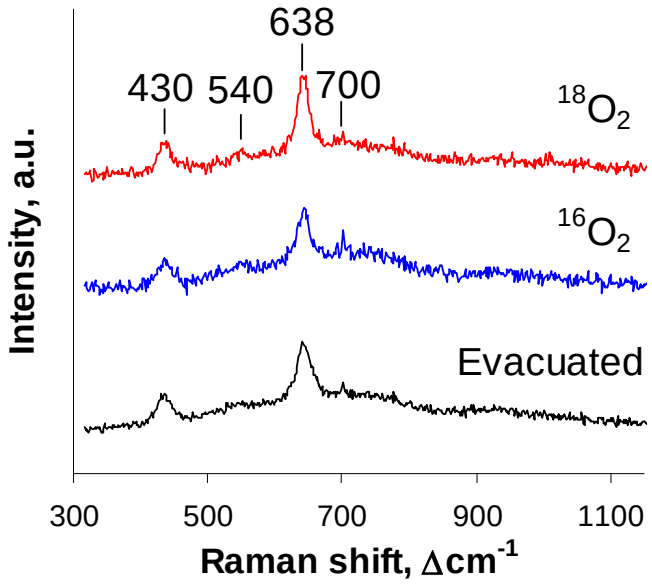

Figure 4.8. Raman spectra collected at room temperature from $La_{0.5}Sr_{0.5}MnO_3$ after evacuation at 625ºC, followed by exposure to $^{16}O_2$ or $^{18}O_2$.

Even though measurements performed on the model composition did not generate positive results, it is still important to try similar measurements on desired cathode materials. To this end, pellets were also tested from GNP powders of the following candidate cathode materials: LSC, LSF, LSCF, SSC, and LSM ($La_{0.85}Sr_{0.15}MnO_3$). For LSM and SSC, powders purchased from Rhodia were also used. Sample pellets were purged in argon gas and evacuated at either 100ºC, 350ºC or 625ºC before being cooled to room temperature for Raman analysis. All attempts were met with results similar to Figures 4.8 and 4.9, which shows an LSM sample that had been evacuated at 100ºC for 12 hrs and then exposed to oxygen. All that was observed was the weak Raman signal for the LSM substrate.

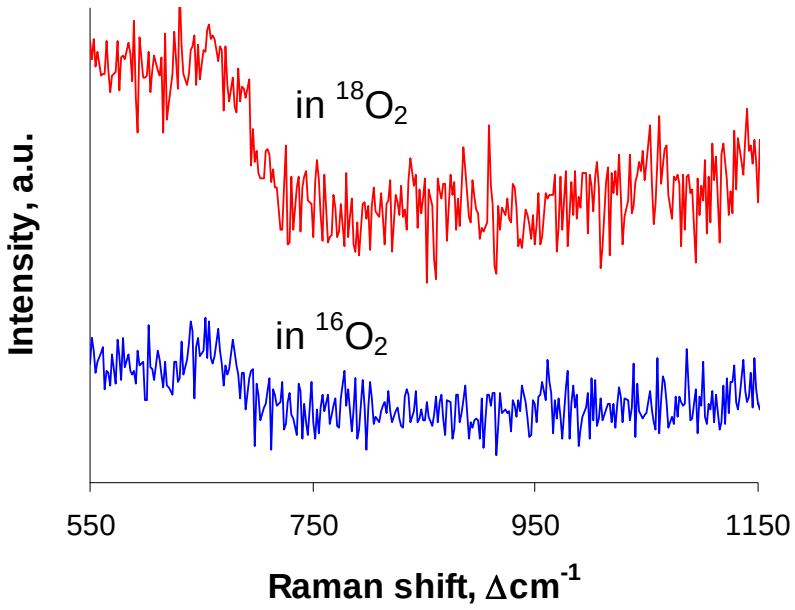

Figure 4.8. Raman spectra collected at room temperature from $La_{0.85}Sr_{0.15}MnO_3$ after evacuation at 100ºC, followed by exposure to $^{16}O_2$ or $^{18}O_2$.

There are a few possibilities for the lack of any surface oxygen signal. First, the surface treatment may not have effectively cleaned the surface, so the concentration of adsorbed oxygen on the exposed sample was not high enough to be detected. Second, even at room temperature, the equilibrium between adsorbed and desorbed oxygen may be such that the concentration of adsorbed species is too small to detect. This assertion could be tested by performing the measurements at cryogenic temperatures. Extra time and funding would be required to retrofit the sample chamber to accommodate such conditions. Finally, the Raman scattering cross section for the species on the cathode surface may be so low as to give a negligible signal-to-noise ratio. This explanation could be plausible, especially considering the weak Raman signal obtained from the bulk cathode compositions compared to that shown earlier by CeO_2.

In another attempt to increase the Raman signal from surface oxygen species, a symmetrical cell consisting of two porous LSCF electrodes painted onto a GDC electrolyte substrate was placed into the chamber and heated to 600ºC and then polarized. Silver lead wires had been attached to both electrodes using silver paste and fired previously at 600ºC for 2 hrs to cure the paste. Both wires were run out of the sample chamber through holes drilled in the quartz window covering the chamber. The holes were then sealed using J.B. Weld brand epoxy. The idea was to force the continual creation of reduced oxygen species on the cathode surface by operating the cell. Also, sometimes an electric field can increase the Raman scattering of a particular species.[24] Figure 4.9 demonstrates that neither anodic nor cathodic polarization produced a signal significantly different from that of the cell at open circuit voltage (OCV – no bias applied to the cell).

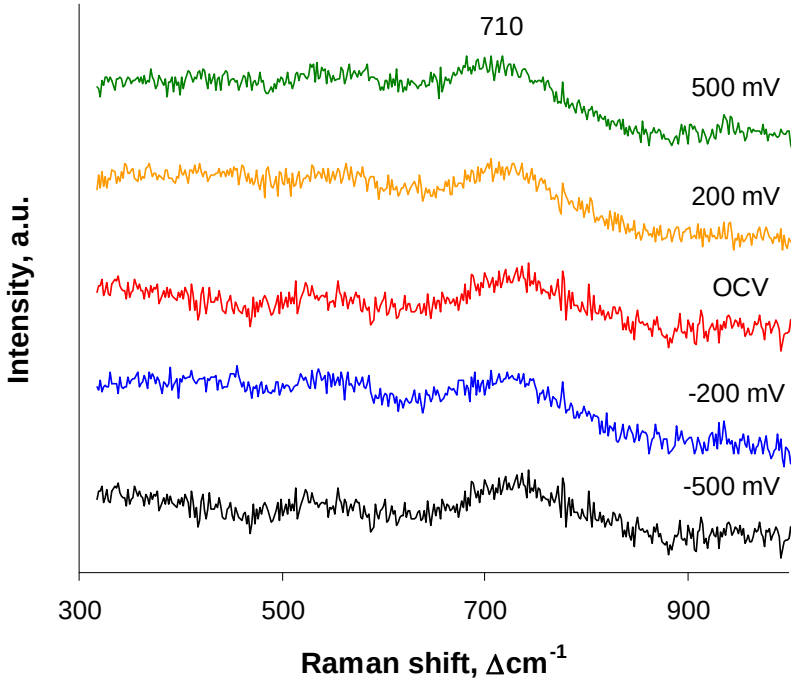

Figure 4.9. Raman spectrum from one electrode surface of an LSCF/GDC/LSCF symmetrical cell polarized at 600ºC in air. The sign of the potential is with respect to the electrode on the bottom surface of the sample (i.e., a negative potential represents cathodic polarization of the top surface).

4.4. Conclusions

From the results presented in this chapter, the author concludes that surface oxygen species cannot be readily observed on the selected perovskite-based SOFC cathode compositions using normal Raman measurements. Further, since the Raman measurements were unsuccessful at room temperature, observing such species under operating conditions is even less likely, since the signal broadens and weakens as the surface species are more likely to desorb as the temperature increases. Conversely, measurements made under cryogenic temperatures would have a greater chance of success. While the data obtained at lower temperatures may not accurately reflect what occurs under operating conditions (given the changes in stoichiometry and electrical properties that occur at higher temperatures), the data can still be used to confirm theoretical calculations. If proper correction factors can be obtained for low temperature data, the DFT models could be more accurately extrapolated to higher temperature conditions. This would allow for more reliable predictions, even if they could not be easily verified. Finally, while outside of the current capabilities of the Raman system used for these experiments, one could use a laser source in the UV region instead of the visible. Raman scattering intensity is proportional to the laser frequency to the fourth power (υ^4), so changing from a visible laser to a UV laser produces a substantial increase in the Raman signal. As long as the sample is not adversely affected by UV radiation, UV Raman spectroscopy is an excellent tool for *in situ* characterization of oxide surfaces.[87]

It must be emphasized that while no surface oxygen signals were detected from the perovskite cathode materials, the signal from the CeO_2 surface was very strong. Raman spectroscopy is still a valuable surface analysis tool for the right system.

An additional concern to address is the data cited in Fig. 4.6 from Wang *et al.* on the $Ag/La_{0.5}Sr_{0.5}MnO_3$ mixture.[88] Why were they able to detect oxygen on the surface of $La_{0.5}Sr_{0.5}MnO_3$ using the same laser wavelength used here? First, as no $^{18}O_2/^{16}O_2$ isotope exchange experiments were performed (or at least, none were reported), the peak may not originate from an oxygen species. Another possible explanation is that the 802 cm^{-1} peak is due to adsorbed oxygen, but from the silver surface and not the $La_{0.5}Sr_{0.5}MnO_3$. Indeed, other groups have found surface Ag-O bonds around 800 cm^{-1}.[68, 89] Finally, the presence of the silver may have enhanced the Raman signal beyond what is expected from normal Raman measurements. This possible phenomenon will be discussed in the next chapter.

CHAPTER 5: SURFACE ENHANCED RAMAN SCATTERING (SERS)

In the previous chapter, it was concluded that normal Raman measurements could not be used to detect oxygen species on the surface of the desired cathode materials. The intensity of the Raman signal was not strong enough to be detected above the sample background. UV Raman spectroscopy was offered as one solution for increasing the signal strength, but it requires purchase of a UV laser and UV optics to manipulate and detect the UV signal. In this chapter, an alternative method of increase the Raman signal is explored: surface enhanced Raman scattering, or SERS. With SERS, metallic nanoparticles (usually silver or gold) are placed on a substrate. These particles, when illuminated with a laser of proper wavelength can enhance the scattering signal of any species within a few nanometers of the particle by up to *15 orders of magnitude*. Possible methods of incorporating metal nanoparticles onto the cathode surface are proposed and initial results from two of these methods are presented.

5.1. The SERS mechanism

The effect known as SERS was first observed in 1974 by Fleishcmann *et al*. while studying the redox behavior of pyridine on roughened silver electrodes.[90, 91*] The

[*] Fleischmann *et al.* are given credit for first observing the SERS effect, but they did not recognize what it was when they measured it. They had roughened the silver electrode to increase the surface area of the electrode, and they attributed the increased signal to the greater surface area. It would take three years before others did the calculation to show that the enhancement was well beyond that which could be attributable to surface area alone and that another enhancement mechanism must be taken place. Still, that original paper has received almost 1200 citations at the time of this writing.

presence of the metal particles has been found to enhance the Raman scattering efficiency of the surrounding area on the order of 10^6.[92, 93] The bulk of the enhancement is thought to derive from the interaction of the surface species with a plasmon field generated around the metal nanoparticles in the presence of the laser's electromagnetic field.[22, 94] The key to the enhancement factor is the size and curvature of the nanoparticle. The orientation of the species with the plasmon field is also significant, as enhancement is greatest perpendicular to the field. Today, within certain systems, Raman enhancement factors as high as 10^{14} have been obtained, allowing for isolation of single molecules.[95] The enhancement effect quickly decays within a few nanometers from the nanoparticle, so it is an ideal technique for observing surface species and surface structures. Many factors such as the temperature, the laser excitation wavelength, and the nature of the sample ultimately control the amount of Raman enhancement available through SERS, so no standardized method currently exists for all applications.[96] Instead, a methodology must be tailored for each specific application.

5.2. SERS strategies for SOFC cathodes

Most SERS research involves looking at molecules in solution. For such applications, SERS-active substrates are now commercially available from companies such as D3 Technologies. These substrates consist of a uniform or patterned layer of nanoparticles (silver or gold) deposited on a substrate (such as quartz). Sometimes, a thin sub-nanometer layer of a nonreactive material such as Al_2O_3 is applied as a coating, thin enough to still provide signal enhancement through the layer while providing a protective layer against whatever solvents may be applied to the substrate.[97] A droplet of a desired

solution is applied to the substrate, and SERS measurements can be taken from molecules that physically or chemically adsorb to the substrate surface. Such an apparatus cannot work for studying SOFC materials; however, the overall concept can be applied to fuel cell electrodes by treating the cathode as the substrate and by somehow depositing metal nanoparticles onto the cathode surface.

The author had previously proposed using three different methods to apply metal nanoparticles to a cathode surface, demonstrated in Figure 5.1:

1. Silver or gold colloids are applied dropwise to the cathode and left to dry in air. After the colloid evaporates, the nanoparticles remain on the surface. Raman measurements can then be taken from areas with aggregates of nanoparticles, creating a SERS effect for cathode surface species in the immediate vicinity of the particles.
2. Combustion chemical vapor deposition (CCVD) is used to simultaneously deposit nanoparticles of the cathode material and of silver on an electrolyte substrate. In CCVD, a combustible solution containing precursors of the desired materials (usually nitrates) is sprayed through a nozzle with a flame at the end.[98, 99] The energy from the combustion of the solution is used to form the desired material, while the vapor phase reaction allows for the creation of nano-scale particles.
3. A thin, discontinuous gold or silver film is sputtered on the surface of a dense cathode substrate. The sputtering time must be short enough to form small (< 50 nm), unconnected metal islands that will be SERS-active.

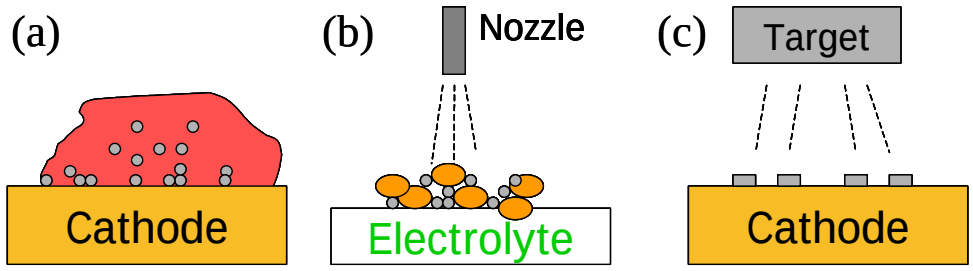

Figure 5.1. Depositing silver/gold nanoparticles on SOFC cathode surfaces for SERS measurements using (a) colloids, (b) CCVD, and (c) sputtering.

5.3. Initial SERS results

5.3.1. Silver and gold colloids

To better gauge an enhancement effect, an initial SERS measurement was attempted using CeO_2, as it already has an observable signal from surface oxygen (see section 4.3). Two drops from a 20 nm gold colloid purchased from British Biocell International (BBI) were applied to pressed pellet of CeO_2 nanopowder (Sigma-Aldrich) and allowed to dry in air. Figure 5.2 shows the effect of the colloid on the Raman signal from the powder. The top two spectra were collected from the discolored region that had been impregnated with the colloid. The overall spectrum intensity did increase (by less than one order of magnitude); however, the intensity of the 831 cm^{-1} peak, previously assigned to a surface peroxide species, did not significantly change. The reason for this broad-based enhancement is not known, but this author posits that it could result from a change in the overall polarizability of the first few layers of the ceria lattice brought about by the plasmon field generated around the gold nanoparticles. As for the lack of enhancement in the oxygen signal, applying the water-based colloid to the powder may have changed the surface composition, with surface oxygen being displaced with adsorbed water molecules or converted to hydroxyl groups.

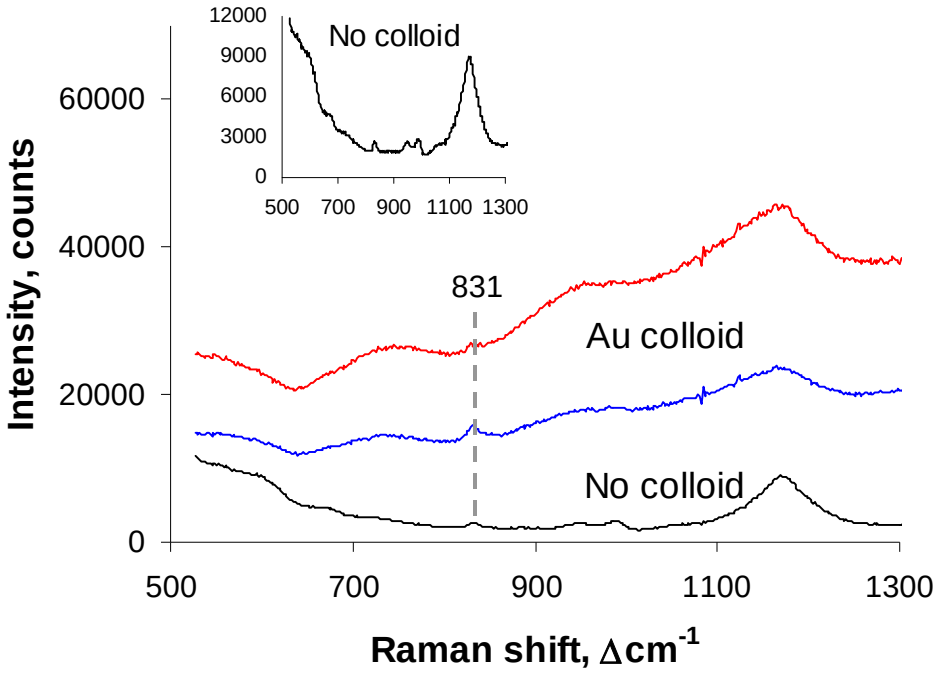

Figure 5.2. Raman spectrum collected in air from CeO_2 nanopowder before (bottom spectrum) and after (top two spectra) application of a 20 nm gold colloid. The 831 cm^{-1} peak has been previously assigned to a surface peroxide species.

The gold colloid particles may also have been too broadly distributed. The pellet was made of dry-pressed powder, so the drops of the colloid were quickly adsorbed into the pellet. Very few nanoparticles probably settled onto the pellet surface. To overcome this, further experiments were carried out on dense, sintered pellets, making it hard for the colloid to permeate into the pellets interior. For dense pellets, the colloid evaporates and leaves a visible ring on the pellet surface. This ring contains most of the nanoparticles, as the ring was the last portion of the colloid to evaporate, leaving the nanoparticles as a deposit. Figure 5.3 shows the ring area on the surface of a dense pellet of $Sm_{0.5}Sr_{0.5}CoO_3$ (a candidate cathode material) to which two drops of the 20 nm gold colloid had been applied. The surface is discolored and small aggregates of nanoparticles can be observed along the edges of the ring.

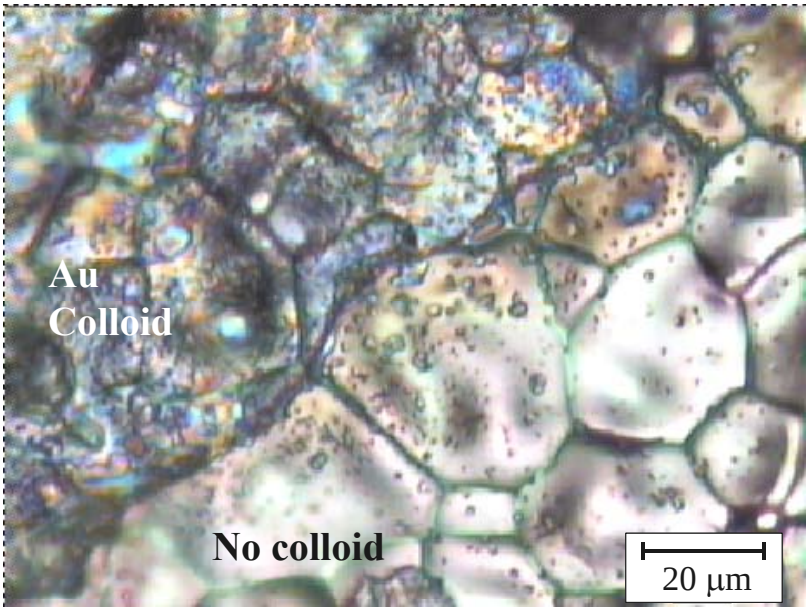

Figure 5.3. Optical micrograph showing the edge of the ring of gold nanoparticles left from the drop of 20 nm gold colloid placed on a dense SSC pellet. Some small aggregates of nanoparticles can be seen on the untreated SSC surface just outside of the ring.

Figure 5.4 shows Raman spectra collected from this ring of nanoparticles from the surface of a dense SSC pellet. The overall spectrum intensity increased by up to one order of magnitude, but of particular interest in varying intensities of the peaks observed in the spectra collected from different locations. The 513, 684, and 780 cm^{-1} peaks received large, but not uniform enhancements. Some of the variation may be caused by local changes in the surface orientation with respect to the nanoparticle, but with such a large sample area (~ 1 μm^2), one would assume that the large number of nanoparticles presumably within that area would average out this effect. However, it is often observed that only a few nanoparticles generate a strong SERS effect, even among those with the supposedly right particle size or shape.[92, 100] If this is true, then a recorded SERS signal

can be dominated by the signal from only a few select nanoparticles.* This use of the selected gold colloid did not cause any new peaks to emerge; all the peaks that were enhanced to different degrees could be found from the untreated sample. These peaks are due to lattice modes and not from surface species, so the colloid did not seem to generate a surface-specific signal.

When a 20 nm silver colloid was used instead of gold, the results were different. For SSC substrates treated with silver colloidal particles, the Raman spectrum generated a fluorescence signal from the silver particles. Similar to the spectrum in Figure 5.5(a), this strong signal was several orders of magnitude greater than that from SSC (see inset).

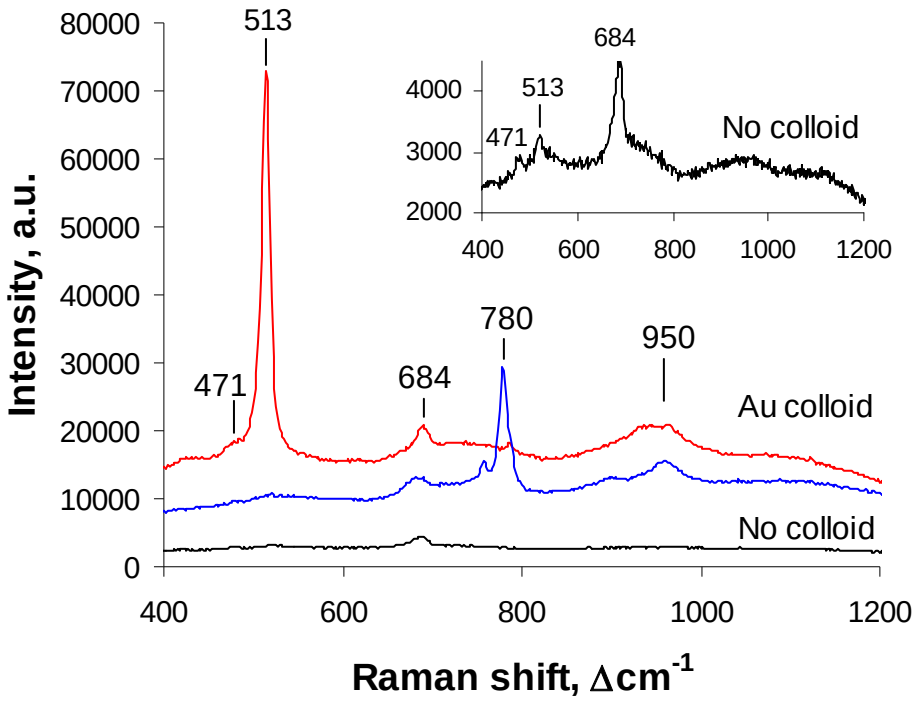

Figure 5.4. Raman spectrum collected in air from a dense SSC pellet before (bottom spectrum) and after (top two spectra) application of a 20 nm gold colloid. The inset from the untreated sample shows that the enhanced peaks were all present before the colloid was applied.

* Within the community of SERS researchers, these particles are known as "hot spots" or "hot sites". Identifying the exact shape and size of these particles and learning how to synthesize such particles with a high, uniform yield is the one of the most important objectives of current SERS research.

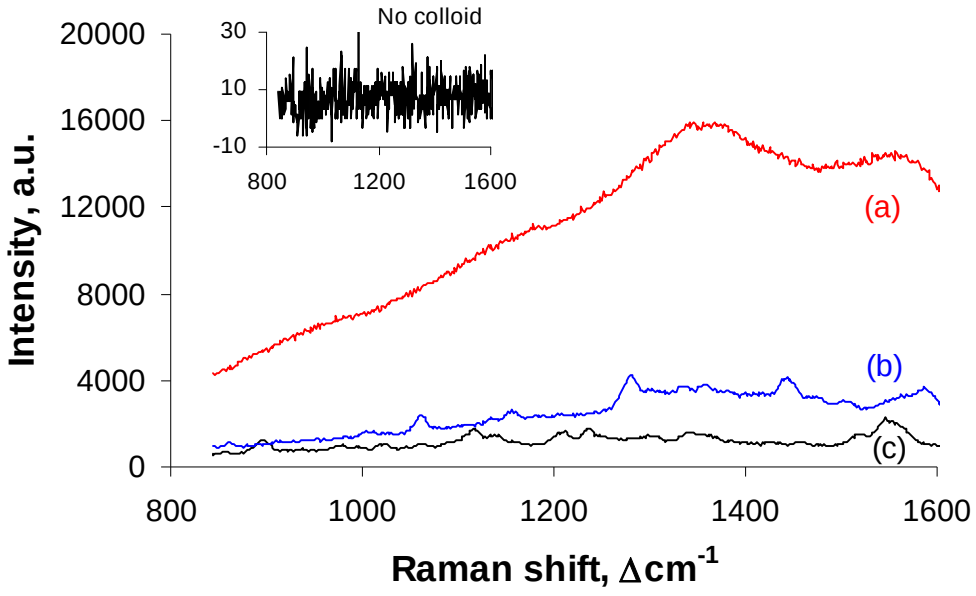

Figure 5.5. Raman spectrum collected at room temperature in air from a dense SSC pellet after application of a 20 nm silver colloid and firing the pellet for two hours at (a) 110ºC, (b) 225ºC, and (c) 310ºC. The inset from the untreated sample shows that the spectrum from the untreated pellet surface.

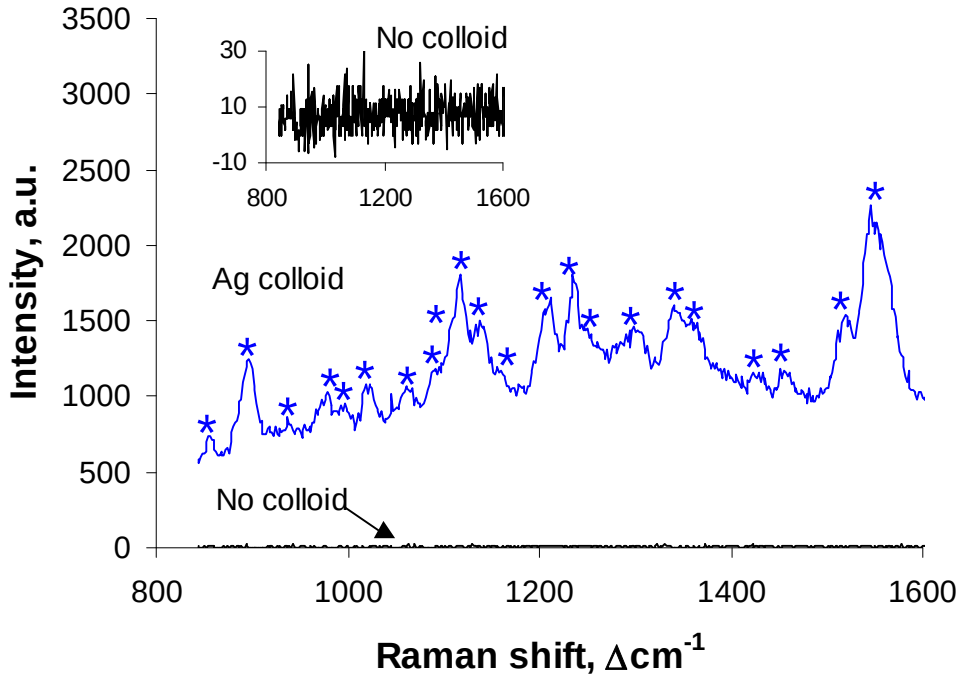

Figure 5.6. Comparison of room temperatures Raman spectrum from an untreated dense SSC pellet and from the pellet surface after application of 20 silver colloid followed by heat treatment at 310ºC. The features marked with an asterisk (*) are assumed to be peaks and occur at the following wavenumbers: 854, 893, 930, 977, 993, 1017, 1057, 1088, 1106, 1115, 1133, 1153, 1211, 1235, 1245, 1295, 1340, 1355, 1420, 1451, 1514, and 1546 cm^{-1}.

As the measured signal came almost entirely from the nanoparticles, an attempt was made to change the particles by firing the sample. The reasoning for this heat treatment was to possibly change the particle morphology and/or to burn off any capping agents used to create the colloids or any other species adsorbed on the silver surface. Figure 5.5 shows the effect of firing the sample with the nanoparticles for 2 hrs at 110ºC, 225ºC, and 310ºC. By 225ºC, new signals started to emerge from the spectrum, and by 310ºC, these new signals were of greater intensity than the fluorescence signal, which slowly decreased with firing temperature. Figure 5.6 compares a spectrum from the sample fired at 310ºC with that from an untreated sample (one with no colloid). For the same collection time (1 second, in this case) the signal from the treated sample was up to three orders of magnitude greater. A minimum of 21 peaks were identified from the wavenumber range sampled for this spectrum from the 310ºC sample: 854, 893, 930, 977, 993, 1017, 1057, 1088, 1106, 1115, 1133, 1153, 1211, 1235, 1245, 1295, 1340, 1355, 1420, 1451, 1514, and 1546 cm^{-1}. The large number of previously unseen peaks makes assigning structures to each individual peak difficult. Many more experiments coupled with theoretical quantum chemical calculations are necessary for any rational attempt at accomplishing this task.

It must be noted that the spectrum shown in Fig. 5.6 was atypical for the sample, in that most locations within the ring of nanoparticles returned spectra similar in shape to spectrum 5.5(a), only with a weaker intensity. Since the signal from the treated area was so strong, a one second collection time was sufficient for collecting a spectrum with an acceptable signal-to-noise ratio. With such a short collection time, it was possible to collect spectra from a large number of locations. After the SSC pellet was fired at a given

temperature, a rectangular mesh containing at least five hundred points spaced at 1 μm intervals on the border between the ring of nanoparticles and the clean SSC surface was sampled using the spectrometer's automated mapping features. For the 310ºC alone, Raman spectra from 1500 points were measured. Only about 5% of the points sampled generated a spectrum with a number of peaks comparable to the spectrum detailed in Fig. 5.6. This small population of strong SERS spectra reinforces the concept that only a small number of particles are strongly SERS-active.

The measured SERS spectrum also demonstrated temporal fluctuations. Figure 5.7 shows two one-second spectra recorded 10 seconds apart from the same location on the dense SSC surface. The signal fluctuates with time, a common SERS phenomenon known as "blinking."[101, 102] This occurrence further confirms that the measured signal is indeed the result of a SERS effect. Blinking also requires that measurements be restricted to a shorter timescale, as the signal fluctuations will average out over time and obscure the SERS effect.

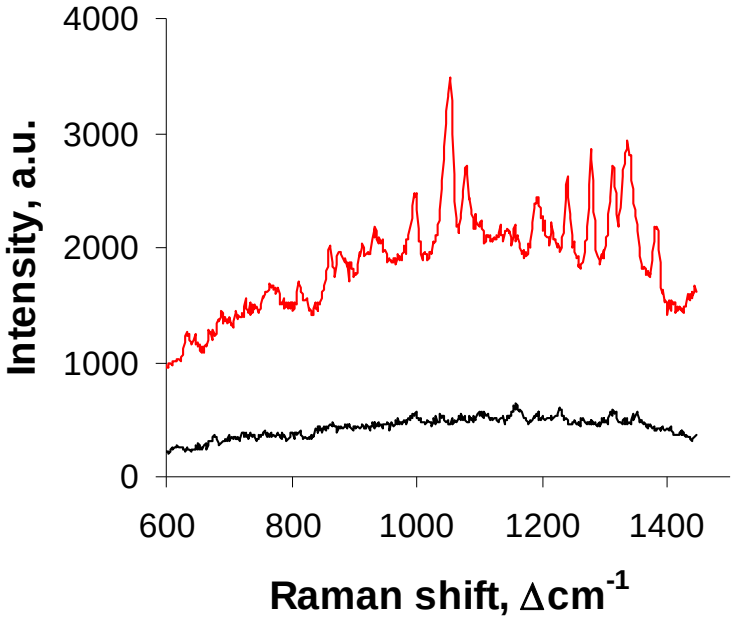

Figure 5.7. Raman spectra collected ten seconds apart from the same point on the SSC sample surface. The sample, treated with 20 nm silver colloid, had been previously fired in air at 310ºC for two hours.

As for why the heat treatment improved the SERS effect, one possible explanation is that the heat treatment changed the morphology of the particle. The strength of the SERS enhancement is wavelength-dependent, in that the strength of the surface plasmon generated around the metal nanoparticle depends on the absorption properties of the particle. The absorption maximum can vary with particle size and shape. Usually, the absorption maximum for a 50 nm silver nanoparticle is near 440 nm.[103] Since the incident wavelength was 514 nm, heating the nanoparticles may have changed the shape of the particle enough to bring the absorption maximum closer to 514 nm. Nanoparticles can begin to melt hundred of degrees below the melting point of the bulk material. Heating the particles to 300ºC may have been a high enough temperature to induce flow in the particles and create either small outcroppings and/or thin connections

between particles during the cooling process. The author recommends measuring the absorbance spectrum of the colloid particles as a function of firing temperature.

5.3.2. Combustion CVD of silver nanoparticles

To test the effectiveness of CCVD for codepositing SERS-active silver nanoparticles alongside candidate materials, test compositions of 50:50 (weight percentage) silver:cathode material were deposited onto YSZ substrates by Dr.Ying Liu, a former group member. Both $La_{0.6}Sr_{0.4}CoO_3$ (LSC) and $La_{0.8}0Sr_{0.2}MnO_3$ (LSM) were tested.[*] Figure 5.8 and 5.9 compare the spectra of the Ag/cathode samples with those from the cathode materials themselves.

[*] Cathode materials containing iron (e.g., LSF and LSCF) were excluded from these trials. Ying informed that iron-containing compounds, due to the iron nitrate precursor, for some reason clogged the spray nuzzle for the CCVD process. Also, gold nanoparticles were not deposited due to the cost of a soluble gold precursor (gold trichloride is ~$65/g and gold nitrate is ~$250/g).

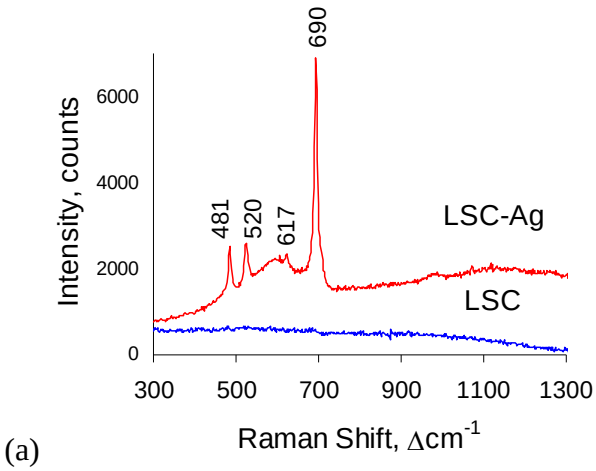

(a)

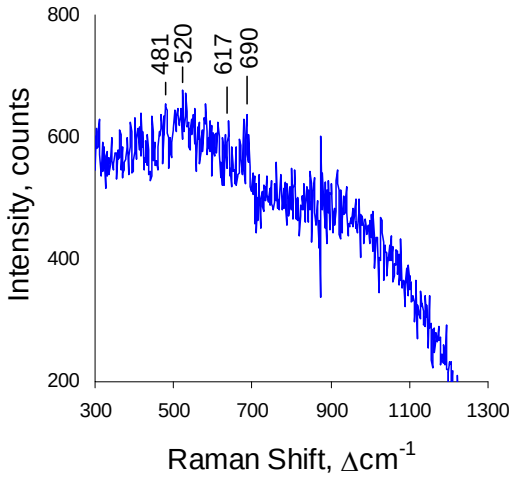

(b)

Figure 5.8. Raman spectrum of (a) codeposited LSC-Ag mixture and (b) LSC. The same collection time was used for both measurements.

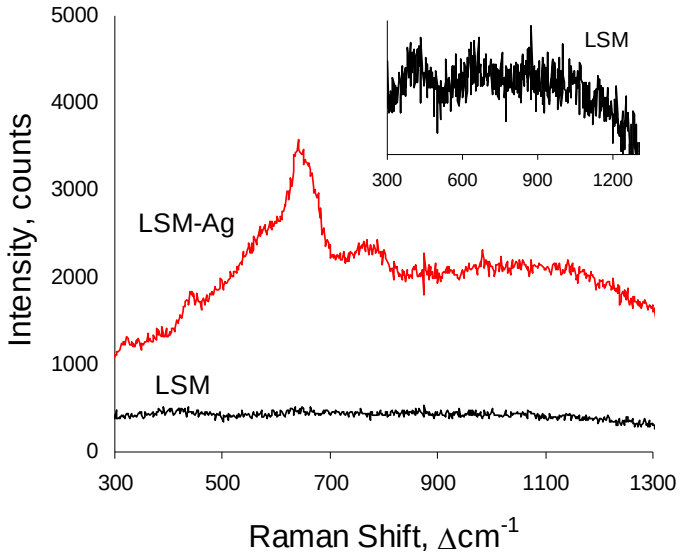

Figure 5.9. Raman spectrum of (a) codeposited LSM-Ag mixture and (b) LSM. The same collection time was used for both measurements.

For both materials, the peaks in the silver-containing sample peaks were magnified by at least one order of magnitude greater than those for the cathode materials alone. For LSC, the five Raman-active peaks indicated were previously very weak (if not arguably absent). As LSC, a rhombohedrally-distorted perovskite, has five theoretically Raman-active peaks (see Appendix A), these five peaks are most likely phonon modes from the lattice, and not from surface oxygen. Indeed, Figure 5.10 shows Raman spectra collected from an isotope exchange experiment as the LSC-Ag was evacuated to 10^{-3} torr for 4 hrs at 400ºC before being cooled to room temperature and exposed to either $^{16}O_2$ or $^{18}O_2$. There were no peak shifts with a ratio corresponding to the masses of the two isotopes.

The peaks in the LSM-Ag spectrum were strong, but they were broad instead of sharp as with the LSC-Ag sample. LSM is a orthorhombic perovskite, and thus has 24 theoretically Raman-active peaks compared with the five for LSC. As discussed in

section 2.3, extra distortions in the lattice brought about by replacing some of the lanthanum cations with strontium, as well as temperature effects, may make it impossible to discern the individual peaks at room temperature.

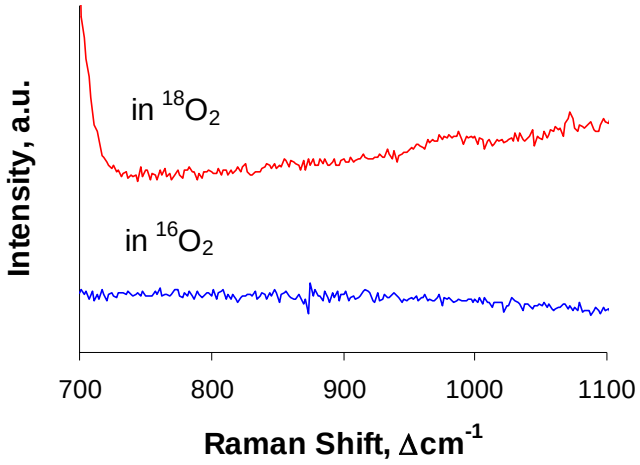

Figure 5.10. Raman spectra collected at room temperature in different oxygen environments from the LSC-Ag CCVD sample after evacuation at 400ºC.

In another CCVD experiment, a layer of silver and chromium oxide (Cr_2O_3) were codeposited onto a dense LSM substrate to see if the silver would enhance the signal from a thin Cr_2O_3 layer on a cathode surface. The results of this experiment are shown in Figure 5.11, which compares the Raman spectrum of a CCVD layer of Ag-Cr_2O_3 with a CCVD layer of Cr_2O_3 alone. The layer codeposited with silver had a weak 550 cm^{-1} peak (the strongest first order Raman peak for Cr_2O_3), but three new peaks at 775, 810, and 855 cm^{-1}. As CCVD is a high temperature synthesis method, the author considered the possibility of a reaction between silver and chromium during the CCVD process. Indeed, silver and chromium can react at high temperatures in air to form silver chromite, $AgCrO_2$, or silver chromate, Ag_2CrO_4. A reference Raman spectrum obtained from Ag_2CrO_4 powder purchased from Alfa Aesar revealed that the new peaks were indeed

from silver chromate. The reactivity of silver with the material being codeposited should thus be considered before attempting CCVD.

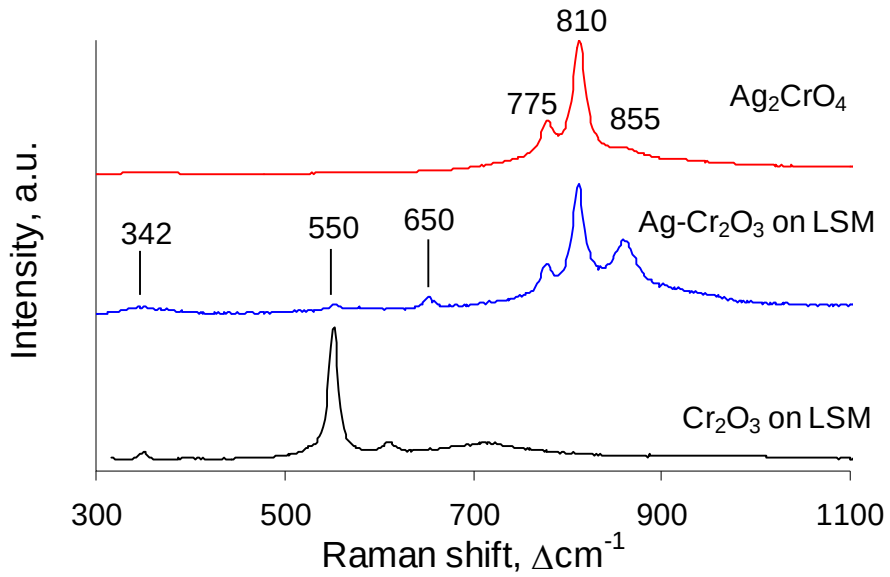

Figure 5.11. Raman spectrum taken from Cr_2O_3 and Ag-Cr_2O_3 CCVD layers deposited onto an LSM substrate.

5.2. Conclusions

Both colloids and CCVD were able to generate an enhanced Raman signal using silver; however, only the silver colloids were able to generate what may be a surface-specific signal. More experiments and theoretical calculations are necessary to better understand the multitude of peaks obtained in conjunction with the silver colloids. The heat treatment necessary to sufficiently activate the silver colloids is interesting and also requires further study. One positive aspect of the heat treatment is that it indicates that the silver nanoparticles can tolerate temperatures up to at least 310ºC. The upper temperature limit of the colloids must be found to see if silver nanoparticles can be used for true *in*

situ measurements. As the melting temperature of bulk silver metal is 962ºC, the nanoparticles will certainly melt and grow together in the 800-1000ºC range of conventional SOFCs, but the lower end of the 400-700ºC intermediate temperature SOFC may still be accessible. Even if true *in situ* SOFC operating conditions are not possible for silver, they may definitely be used for surface analysis in PEMFCs, which operate below 200ºC.

Similar heat treatment experiments need to be carried out with the gold colloid. Such additional testing is desirable since bulk gold metal melts at 1064ºC, which gives it a higher maximum operating temperature. Further, gold is much less reactive than silver, chemically and catalytically. Gold nanoparticles would not react with the cathode, nor would its surface catalyze the oxygen reduction reaction, which would taint any electrochemical and spectroscopic data obtained *in situ*.

The reactivity of silver is an important concern for two reasons. First, the high temperatures present inside the flame during CCVD greatly increases the chance of reaction between the silver and the material being codeposited with it. With respect to candidate SOFC cathode materials, silver phases exist that contain cobalt ($AgCoO_2$) and manganese (Ag_2MnO_4, $Ag_2Mn_8O_{16}$).[104-107] Not only would formation of secondary phases eliminate any chance of a SERS effect, but also the stoichiometry of the deposited cathode material would be changed. Second, even if silver colloids are used instead of CCVD, the silver may still react with other components at or under SOFC operating conditions. One case study with such a problem is presented in Chapter 7.

Finally, as some success was obtained with both CCVD and colloids, one could reasonably expect success with sputtering, the third proposed technique not explored in this chapter. Indeed, the literature supports the idea that discontinuous nanoscale silver islands can be sputtered onto substrates and that the islands can produce a strong surface plasmon field when illuminated with a laser source of the proper wavelength.[108]

CHAPTER 6: CARBON DEPOSITION ON SOFC ANODES

The heretofore-mentioned results were concerned with trying to observe surface oxygen species on an SOFC cathode. The goal of such measurements was to observe the species involved in normal fuel cell operation. Attention is now turned to characterizing species that prevent normal fuel cell operation. In this chapter, Raman spectroscopy is shown to be a useful tool for monitoring carbon deposition on an SOFC anode, a side effect of using hydrocarbons as a fuel source.

6.1. Hydrocarbon fuels and SOFC anodes

A distinct advantage of SOFCs over PEMFCs is the fuel flexibility of SOFCs. The high operating temperatures of SOFCs permit the use of hydrocarbons (methane, propane, etc.) and small-chain alcohols (methanol, ethanol) either through direct oxidation or through internal reforming (breaking the fuel source into hydrogen and carbon monoxide). Unfortunately, these fuel sources can break down to form carbon, either through direct pyrolysis or through disproportionation of the carbon monoxide formed during internal reformation of the fuel:[109]

$$\textbf{Pyrolysis: } CH_4 \rightarrow C + 2\ H_2$$

$$\textbf{Disproportionation: } 2\ CO \rightarrow C + 2\ CO_2$$

It has been shown that the performance of conventional SOFCs (those with nickel-YSZ anodes) running on hydrocarbon fuels experience degrades with time.[76, 110-113] The drop in performance is considered to result from the deposition of carbon on the anode surface, blocking catalytically-active surface area.[113]

In principle, the cell anode can oxidize a small amount of carbon during operation. Also, the rate of carbon formation can be curtailed by humidifying the fuel line. The steam present drives the water gas shift reaction, in which the CO formed during fuel reformation is converted to CO_2 and H_2, lowering the rate of disproportionation:

Water gas shift: $CO + H_2O \rightarrow CO_2 + H_2$

Further, some anode materials, such as copper, are less prone to carbon deposition than nickel and can thus handle longer-chain hydrocarbons.[114, 115] Finally, there are claims that a small amount of carbon deposition can slightly increase cell performance, as small carbon fibers improves electrical connectivity within the anode.[116] Questions still exist over how much carbon a particular anode material can tolerate before undergoing a significant drop in performance.

6.2. Monitoring carbon deposition on patterned electrodes

Correlations between carbon deposition and electrochemical performance can be *ex situ* by quenching multiple samples after various running times and examining the carbon deposits using electron microscopy. Such a method, however, is time-consuming and suffers from the possibility of artifacts produced during the cooling process. As stated in Chapter 2, all common allotropes of carbon are Raman-active, so Raman spectroscopy seems an ideal tool for simultaneous *in situ* spectroscopic/electrochemical measurements. Professor Robert Walker *et al.* at the University of Maryland were the first to develop and demonstrate a Raman microscope system for the *in situ* study of carbon formation on nickel SOFC anodes.[37, 38] However, their system lacks the ability to

perform high resolution Raman mapping since they cannot adroitly maneuver their sample since it is contained within a vertical clamp-style furnace. Further, while a microscope objective focuses the laser to a micron-sized spot, they lack the ability to see visually the spot on the sample on which they've focused. The Raman microscope system used here does not share these disadvantages, allowing for position-dependent Raman measurements to be taken under SOFC operating conditions.

The samples used for Raman mapping measurements consisted of a YSZ substrate onto which a micropatterned electrode (see section 3.3) of either nickel or copper had been deposited. These samples were heated inside Raman sample chamber and exposed to either CH_4 or CH_3H_8 fuel gases. Raman measurements were variously recorded *in situ* and *ex situ* as a function of time and position.

Figure 6.1 shows a patterned nickel sample before and after exposure to propane at 625ºC for two hrs. The nickel electrodes became black carbon. An *ex situ* Raman spectrum collected from the nickel surface contains two strong peaks at 1580 and 1330 cm^{-1}. The 1580 cm^{-1} peak is the E_{2g} lattice phonon mode of graphitic carbon, while the 1330 cm^{-1} indicates that the graphite is disordered, with some of the carbon exhibiting sp^2 character instead of sp^3.[35] A spectrum from the YSZ surface does not have a discernible carbon signal. The broad feature at 1600 cm^{-1} should not be confused with the carbon peak, as it results from the YSZ itself.

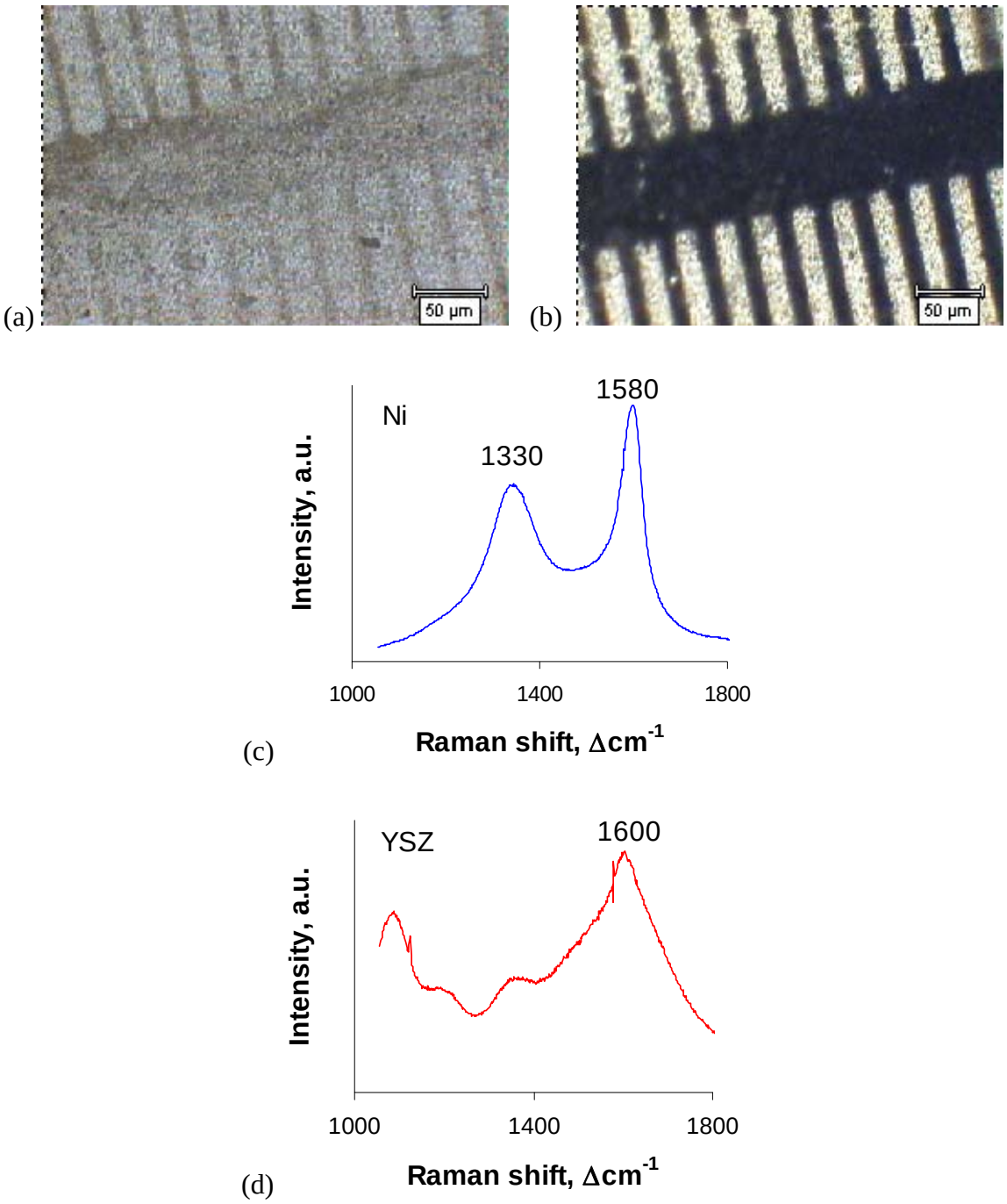

Figure 6.1. Optical micrographs collected *ex situ* from a patterned Ni electrode deposited on a YSZ substrate (a) before and (b) after exposure to propane at 625ºC for 2 hrs. The lighter regions are the YSZ substrate. Also shown are *ex situ* Raman spectra collected from the (c) nickel and (d) YSZ surfaces. The two peaks indicate in (c) are from defective graphite.

From the optical micrograph, it looks as if carbon only formed on the nickel surface, leaving the YSZ relatively clean. To confirm this observation, a Raman map showing the presence of carbon was constructed by collecting Raman spectra at various points within the grid shown in Figure 6.2. The integrated peak intensity of the 1580 cm^{-1} carbon peak was plotted as a function of position. The 1580 cm^{-1} peak was chosen instead of the 1330 cm^{-1} peak because it is generally the stronger of the two peaks. The Raman map confirms that the carbon preferentially formed on the nickel surface. Any small amount of carbon on the YSZ could have resulted from dusting, as the gas flow over the electrode blew less tenacious carbon off the nickel surface and onto the YSZ. Further, some of the presumed carbon signal on the YSZ could be an artifact of the YSZ signal at 1600 cm^{-1}. The lack of carbon on the YSZ is significant in that it indicates gas pathways over a YSZ surface within a Ni-YSZ cermet anode will not clog with carbon, unless there is significant spillover from a neighboring nickel surface.

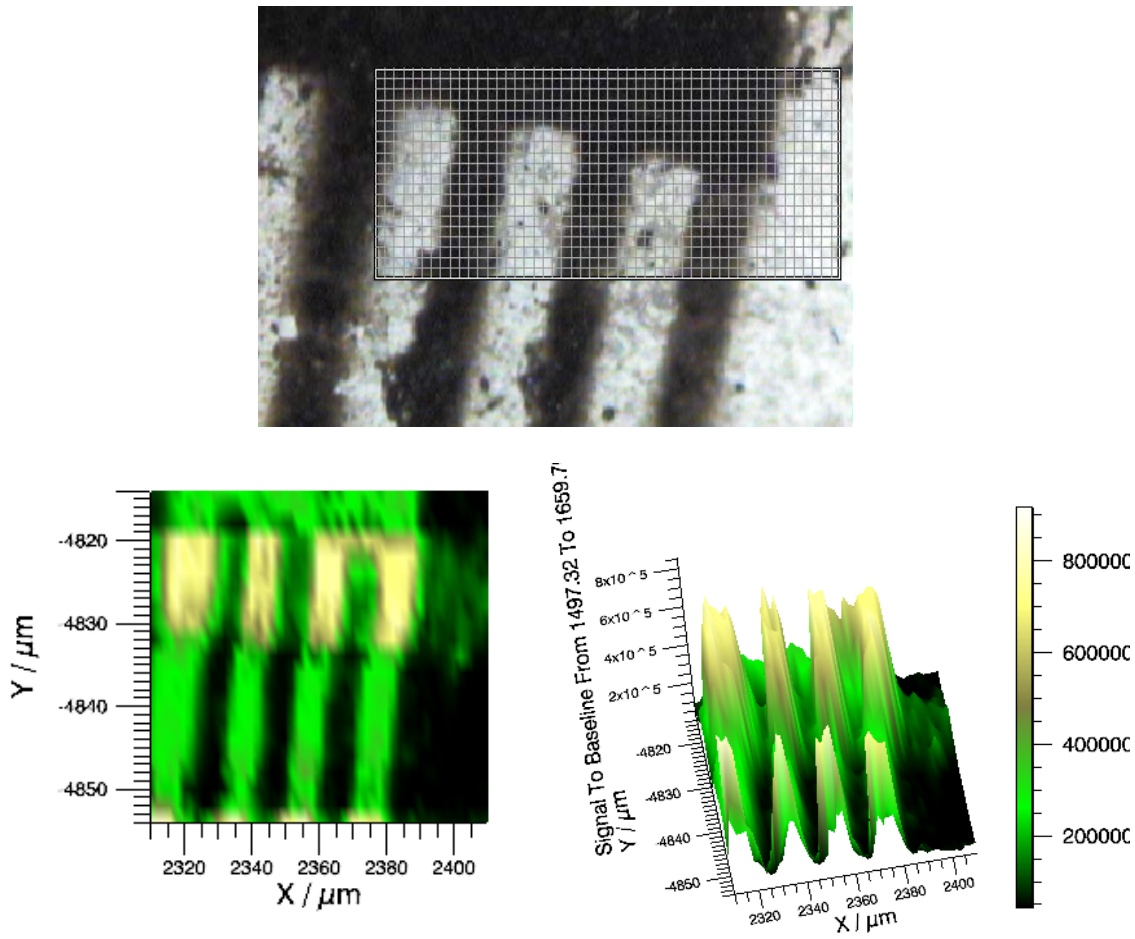

Figure 6.2. Raman map from the sample in Fig. 6.1 plotting the integrated peak intensity of the 1580 cm^{-1} carbon peak. Spectra were collected *ex situ* at 2 µm intervals within the indicated grid.

While the *ex situ* mapping data is interesting, the information gained from it could have been obtained using SEM/EDS analysis. The ultimate goal is to perform *in situ* Raman analysis of an SOFC anode. To this end, *in situ* Raman spectra were collected at 15 minute intervals from the Ni surface of a patterned Ni sample (on YSZ) exposed to CH_4 for 12 hrs at 625ºC. Figure 6.3 shows the emergence of carbon peaks as a function of time from the selected nickel location. There was a long delay of approximately ten hours before any discernible from carbon was observed. There are two explanations for this. First, the Raman system may not be sensitive enough to detect extremely thin layers of carbon. The threshold thickness could be determined by correlating Raman signal with sputtered thin films of graphite of known thickness. Second, as the selected location was not directly next to the gas inlet of the chamber, other regions of the sample may have began experiencing carbon formation before the selected location. The delay could have thus been caused by the slow growth of the deposited layer towards the selected spot. To judge this effect, more samples need to be run with spectra recorded as a function of time at different relative positions on each sample.

Once the carbon was detectable above the background, the signal strength reached a plateau after a few hours. At this point, the carbon layer was thicker than the skin depth of the graphite, meaning that the laser could only penetrate a certain depth into the carbon layer no matter how much thicker the layer grew. The author is not aware of the specific thickness value for graphite for this temperature. While these results indicate there is a window of opportunity within which meaningful time-dependent data can be recorded, the size of this window can be increased by adjusting the operating conditions of the cell (e.g., changing the temperature or diluting the fuel gas).

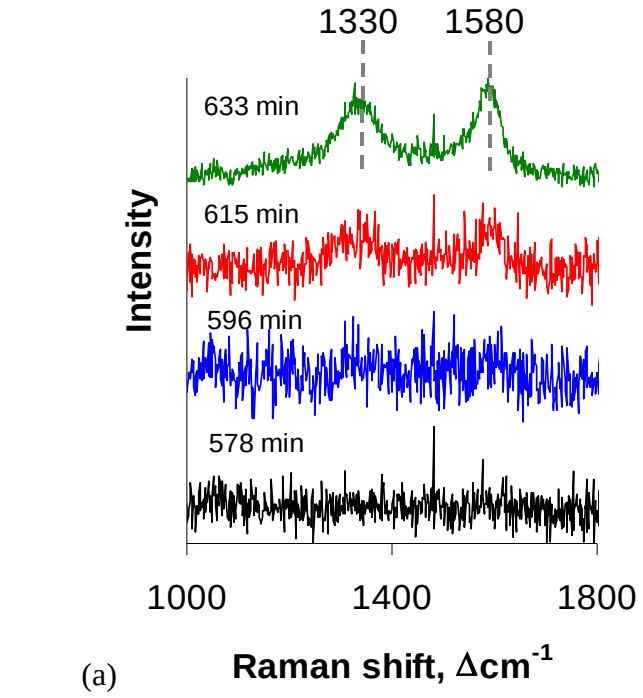

(a)

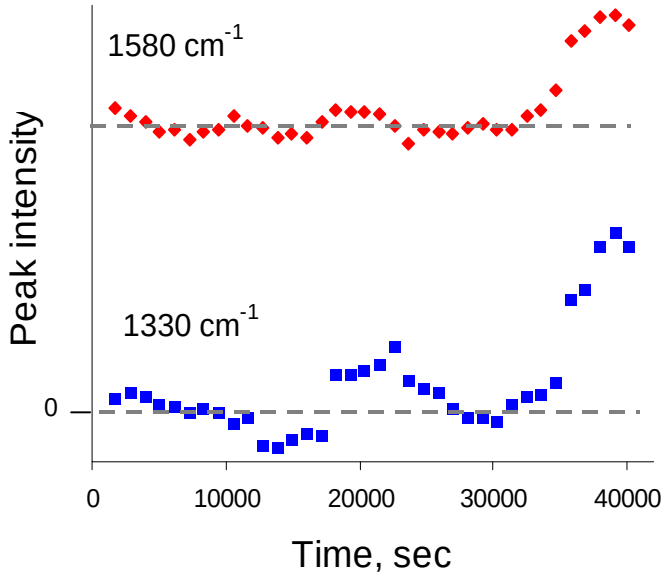

(b)

Figure 6.3. (a) Raman spectra recorded at approximately 15 minute intervals from one spot on a patterned nickel electrode exposed to 100% CH_4 at 625ºC for 12 hrs. (b) Plot of the integrated peak intensity of the 1330 and 1580 cm^{-1} carbon peaks as a function of time.

Once a significant carbon signal was detected, the *in situ* Raman map in Figure 6.4 was generated around the selected location by again plotting the 1580 cm^{-1} peak intensity as a function of position. Once again, the carbon was detected almost exclusively on the nickel surface. To confirm this observation, the sample was examined using an SEM. The micrograph in Figure 6.5 shows the presence of carbon nodules on the patterned electrode, but not the YSZ, surface. The largest of the carbon particles is approximately 500 nm, with many particles being on the order of 50-100 nm. While the carbon layer may not be completely continuous, the particle sizes are much smaller than the diameter of the Raman laser spot, so the spectrometer is not able to resolve individual particles.

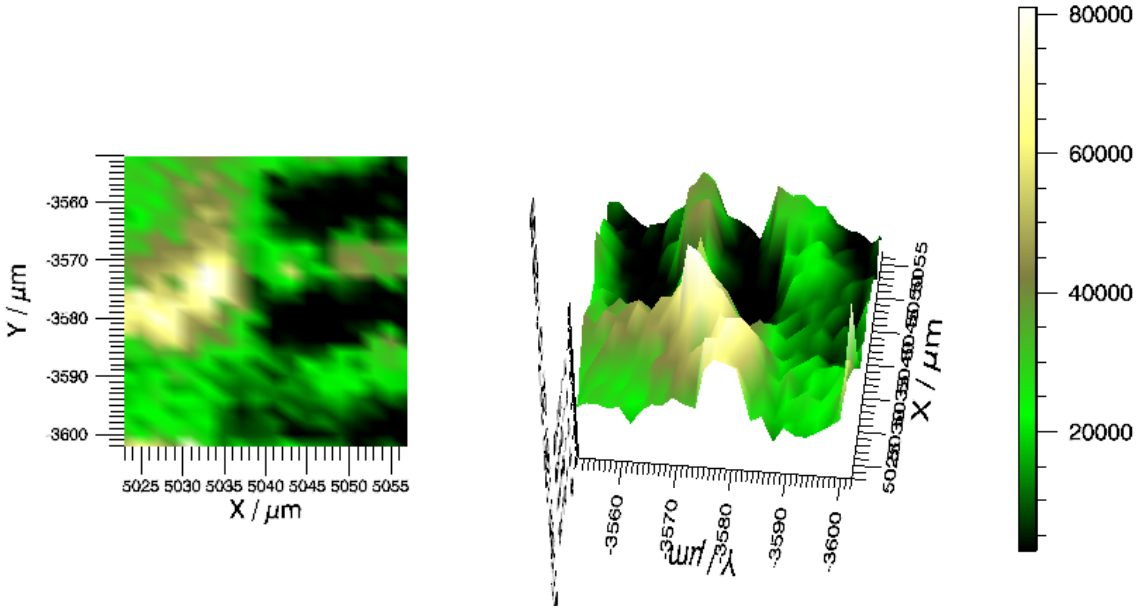

Figure 6.4. Raman map of the 1580 cm^{-1} peak intensity from carbon calculated from spectra collected from a patterned Ni sample exposed to CH_4 at 625ºC for 12 hrs.

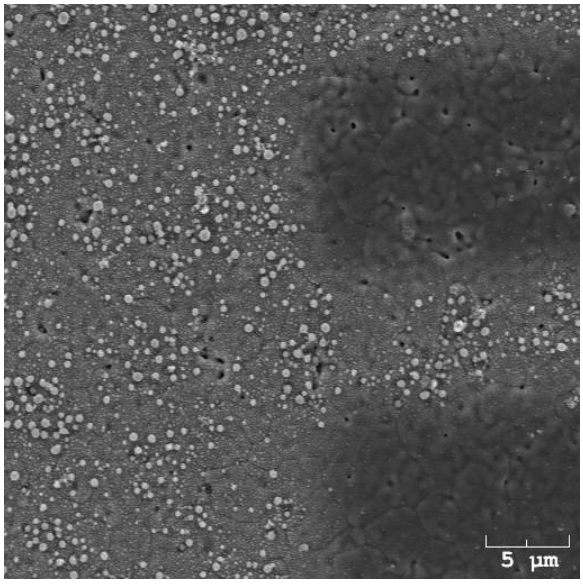

Figure 6.5. SEM micrograph showing the presence of carbon on a patterned Ni electrode on a YSZ substrate after exposure to CH_4 at 625ºC for 48 hrs. The darker regions are the YSZ substrate.

To provide a frame of reference for the nickel data, a patterned copper sample heated to 625ºC inside the chamber and exposed to methane for 12 hrs. Copper was chosen due to its known lack of strong catalytic activity towards carbon formation.[117] As shown in Figure 6.6, the same amount of exposure that left the nickel covered in carbon did not produce any carbon signal significantly greater than the background. To push the system, propane was then flowed through the chamber for six hours. At this point, carbon was finally detected on the copper surface; however, under these conditions, most of the chamber had filled with carbon black that had been depositing on the walls of the stainless steel chamber. The carbon detected may have indeed formed directly on the copper surface, but it may have instead resulted from dusting from carbon formed elsewhere in the chamber. The difference in carbon signal from the nickel and copper samples demonstrates the utility of Raman spectroscopy in the evaluation of anode materials with respect to susceptibility to carbon deposition.

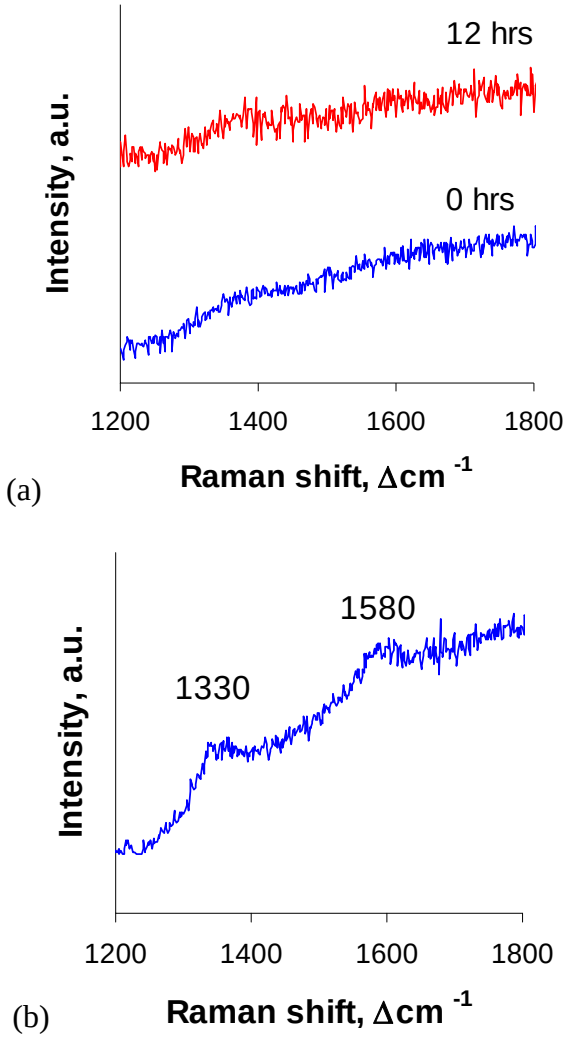

Figure 6.6. Raman spectrum collected *in situ* from a patterned copper electrode on a YSZ substrate exposed to (a) CH4 at 625ºC for 12 hrs and (b) propane for 6 hrs at 625ºC.

6.3. Conclusions

Raman spectroscopy was shown to have some utility in the *in situ* and *ex situ* evaluation of carbon deposition on different SOFC anode materials. The relative amount of carbon could be monitored as a function of operating condition and position. The position-dependent data adds another layer of system evaluation as the susceptibility of

different locations within a cell, such as the triple phase boundary or surfaces near the gas inlet/outlet, can be observed. One should note that the carbon deposition seen in the data presented here was a result of simple chemical exposure to the different fuel gases. No potential was applied to the cell. The flow of current through the cell should reduce the amount of carbon present, as some of it can be oxidized to CO or CO_2 by the anode.

An important consideration when taking *in situ* maps is the time necessary to collect the spectra for the map. For large map areas, or for large individual spectrum collection times, the sample can change between starting and finishing the map. Some maps can take hours to generate. As seen in Fig. 6.3, the thickness of a surface layer can go from undetectable to greater than the skin depth with a few hours. Taking too many data points or taking long scans will skew position-dependent data based on the viable measurement window for the system in question. If *in situ* maps cannot be quickly (relative to the timescale of the measurement window), then one should consider simply taking time-dependent measurements from only a few selected points. *In situ* maps become a better option when studying an obtained steady state or equilibrium position.

Finally, one big advantage of Raman spectroscopy for the study of carbon deposition is its ability to detect amorphous carbon. The strong 1330 cm^{-1} observed in the samples indicates a highly defective carbon structure. This disorder makes the carbon extremely difficult to detect using XRD diffraction, as the carbon is mostly amorphous. The same disordered nature that reduces the ability to detect the carbon with XRD instead provides another useful signal that can be detected and analyzed with Raman spectroscopy.

CHAPTER 7: CHROMIUM POISONING OF SOFC CATHODES

A large impetus behind lowering the SOFC operating temperature is to permit the use of stainless steel interconnect layers between individual cells.[118] Stainless steels are much less expensive than the exotic oxides needed for SOFCs operating near 1000ºC. Unfortunately, with the much cheaper metallic interconnects comes a much greater susceptibility to poisoning of the cathode by volatile chromium species from oxide scales on the metal's surface.[9, 119] Species such as CrO_3, Cr_2O_3, and $CrO_2(OH)_2$ are thought to travel through the vapor phase to the cathode and form secondary phases such as $SrCrO_4$ and a $(Mn/Cr)_3O_4$ spinel that reduce cathode performance.[120-122] Literature reports vary as to the exact contaminants that form, where they form, whether their formation is chemically- or electrochemically-driven, and the extent to which different cathode materials are susceptible to Cr contamination.[123-126] For example, chromium oxyhyrdoxide, $CrO_2(OH)_2$, could be reduced at the triple phase boundary to Cr_2O_3:

$$2\ CrO(OH)_2(g) + 6e' \rightarrow Cr_2O_3(s) + 2\ H_2O(g) + 3\ O^{2-}$$

Reaction of the Cr_2O_3 with an LSM cathode could produce strontium dichromate, $SrCr_2O_7$:

$$2\ Cr_2O_3 + 5\ La_{0.8}Sr_{0.2}MnO_3 + O_2 \rightarrow SrCr_2O_7 + 4\ LaMnO_3 + (Mn/Cr)_3O_4$$

Knowing which cathode materials (or which cations within a material) are prone to Cr contamination is crucial information for cathode material selection and design. As noted in section 2.3, most major chromium contaminants are Raman-active, meaning Raman spectroscopy should be able to supply some answers to the questions being asked about Cr poisoning. In this chapter, initial results are revealed that demonstrate the utility

of Raman spectroscopy towards studying Cr contamination of LSM cathodes. Additionally, reactions between Cr-containing vapor with silver are presented, raising design concerns for some proposed SOFC cathodes that contain silver.

7.1. Chromium poisoning experimental setup

To test the susceptibility of LSM to Cr contamination, Cr-containing vapor had to delivered to the sample inside the high temperature Raman chamber. Figure 7.1 details the Cr delivery process. Oxygen was blown through a bubbler held at 75ºC to humidify the gas. The water vapor was added to increase the amount of Cr vapor species as $CrO(OH)_2$ in order to accelerate the contamination process. The humidified oxygen then passed through steel tubing wrapped in heating tape (held at 90ºC to prevent water condensation) into the sample chamber. At the gas inlet, a small pellet of pressed Cr_2O_3 powder was placed, generating Cr-containing vapor as the oxygen blew over the top of the powder on its way to the sample. The gas exited the chamber through a stainless steel tube (also wrapped in heating tape held at 90ºC) before being run through a condenser to trap the cooling water vapor.[*] The samples used for these experiments consisted of a patterned LSM ($La_{0.8}Sr_{0.2}MnO_3$) electrode deposited onto an LSM substrate. To aid in application of a potential across the sample, a patterned platinum current collector was deposited on top of and perpendicular to the LSM pattern.

[*] I attempted to identify the Cr vapor species present by running mass spectrometry on the exhaust gas; however, no species were detected. Either the species concentrations were below the detection limit of the equipment, or the vapor phase species condensed in the exhaust tube before reaching the mass spectrometer. The formation of Cr-containing vapor was instead inferred from the formation of Cr species on the sample surface. Barring any miracles or stray nuclear reactions that could somehow create chromium wholecloth within the sample, the author feels that this is a reasonable inference.

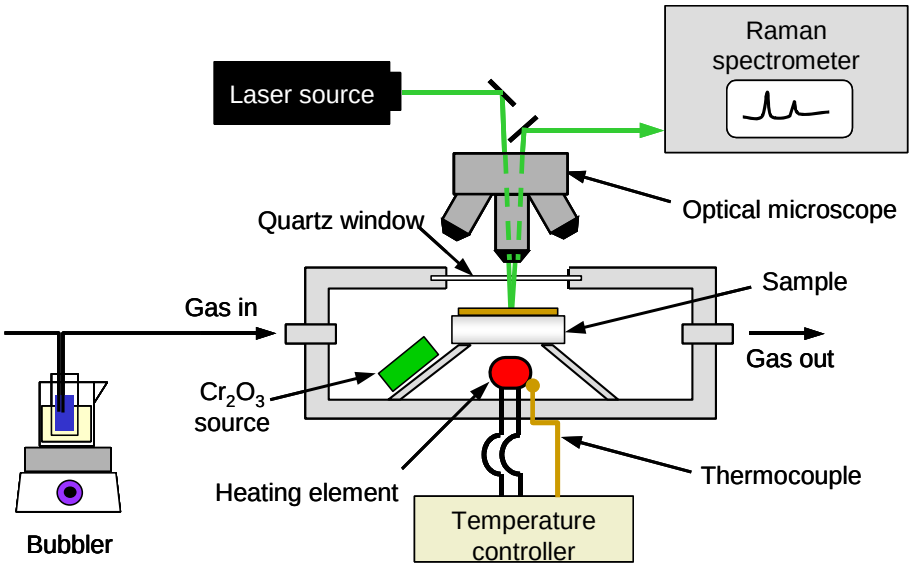

Figure 7.1. Experimental setup used for Raman studies of chromium poisoning of SOFC cathode materials.

7.2. Formation of $SrCrO_4$ on patterned LSM electrodes

Figure 7.2 shows how the surface of the patterned LSM electrode darkened within 24 hrs exposure to Cr-containing vapor (meaning humidified oxygen or air that had blown across the Cr_2O_3 pellet before reaching the sample). In coordination with the change, a new peak at 875 cm^{-1} emerged in the Raman spectrum from the LSM surface (see Fig. 7.2(c)). As the peak was broad and not very strong, the sample was cooled down to room temperature and examined *ex situ*, at which point the one broad peak spread into a family of peaks at 850, 885, and 920 cm^{-1}. Peaks could also be seen at 316 and 370 cm^{-1}. Comparison to reference spectra of possible Cr contaminants indicates that a surface layer of $SrCrO_4$ had formed on the LSM surface.[127] Some spectra collected at different locations on the LSM surface, as in spectrum (2) in Fig. 7.3(d), also contained a broad peak at 660 cm^{-1}, which may belong to the $(Mn/Cr)_3O_4$ spinel.

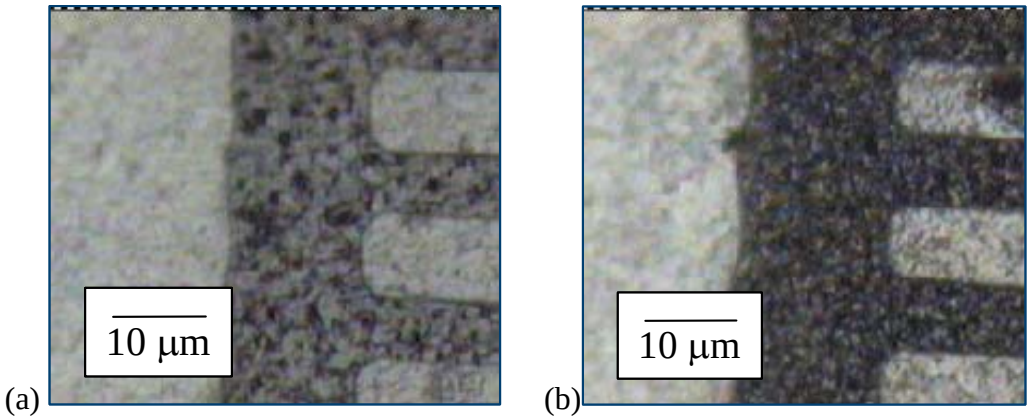

(a) (b)

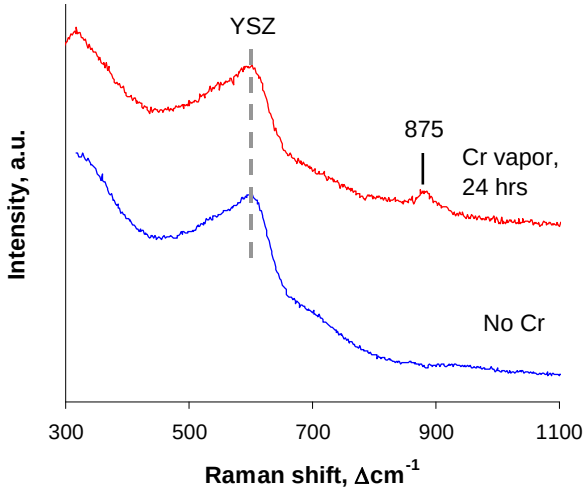

(c)

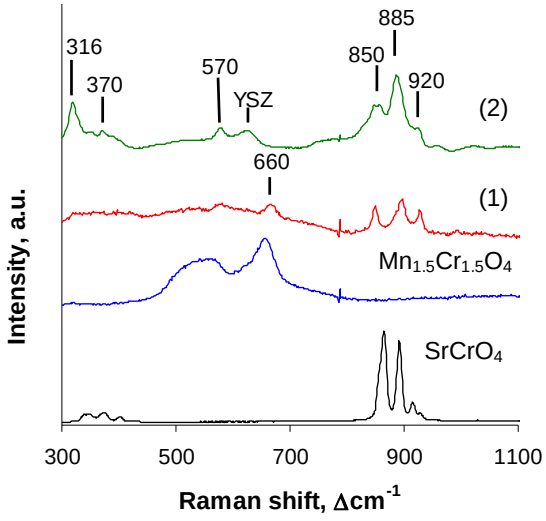

(d)

Figure 7.2. (a) Patterned LSM electrode on a YSZ substrate (a) before and (b) after exposure to Cr-containing vapor at 625ºC for 24 hrs. The lighter regions are the YSZ substrate. (c) Raman spectra collected *in situ* from the LSM surface with and without exposure to Cr vapor. (d) Typical Raman spectra collected *ex situ* from two spots – spectra (1) and (2) - on the LSM surface after the exposure. Reference spectra for $SrCrO_4$ and a $(Mn/Cr)_3O_4$ spinel provided for comparison.

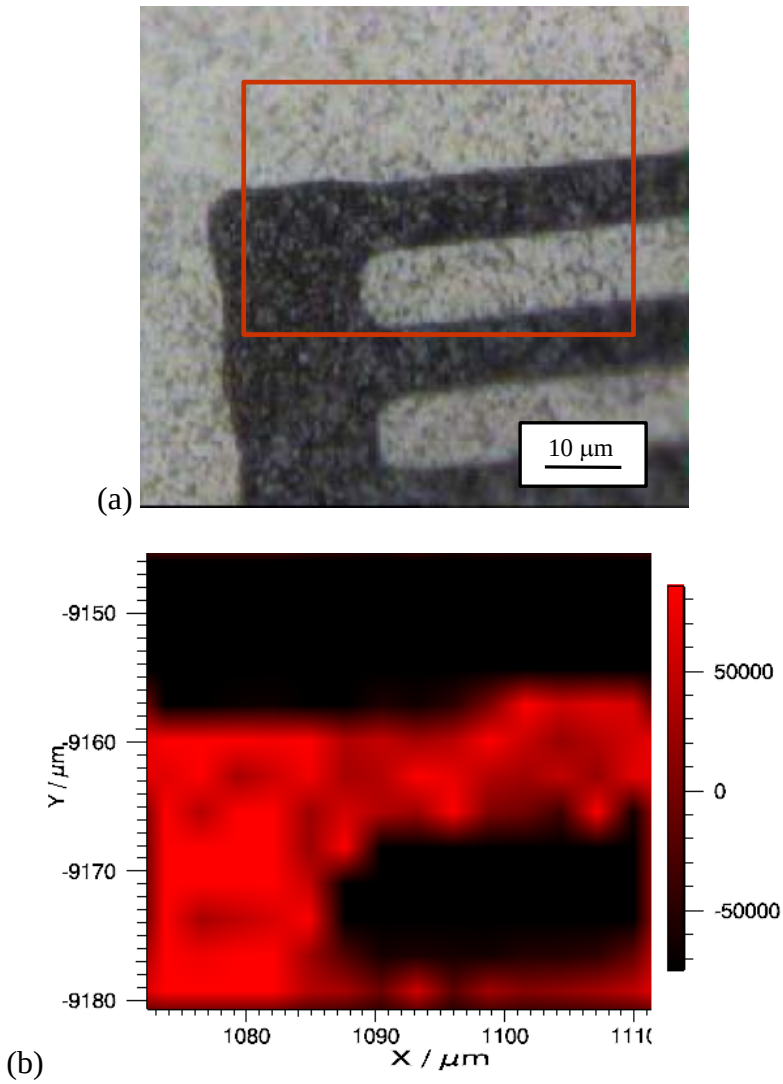

Figure 7.3. Raman map of the intensity of the 885 cm-1 SrCrO4 peak from a patterned LSM electrode on a YSZ substrate exposed to Cr-containing for 24 hrs at 625ºC. The map area is outlined in optical micrograph (a). The lighter regions are the YSZ substrate. A lighter shade in the map indicates a higher peak intensity.

To gauge the pervasiveness of the strontium chromate, the Raman map in Figure 7.3 plotting the integrated peak intensity of the 885 cm^{-1} $SrCrO_4$ peak was generated by collecting Raman spectra at 2 µm intervals within the region indicated in Fig. 7.3 (a). While $SrCrO_4$ was only found on the cathode surface, the phase was found across the

entire LSM surface. This result is reasonable, as the formation of the phase should have been chemically, showing no preference for the triple phase boundary between the cathode, electrolyte, and gas phase. SEM analysis revealed that the $SrCrO_4$ had formed needlelike deposits on the LSM surface, as shown in Figure 7.4. The EDS mapping of Cr and Sr shown in Fig. 7.4(b) was inconclusive. While the presence of Cr on the LSM surface was confirmed, its presence could not be correlated with that of Sr. The Sr EDS signal is contaminated by the presence of yttrium in the substrate. Strontium and yttrium only differ in atomic number by one and have similar atomic masses (87.6 g/mol for Sr vs. 88.9 g/mol for Y), so they are difficult to differentiate from one another using EDS.

(a)

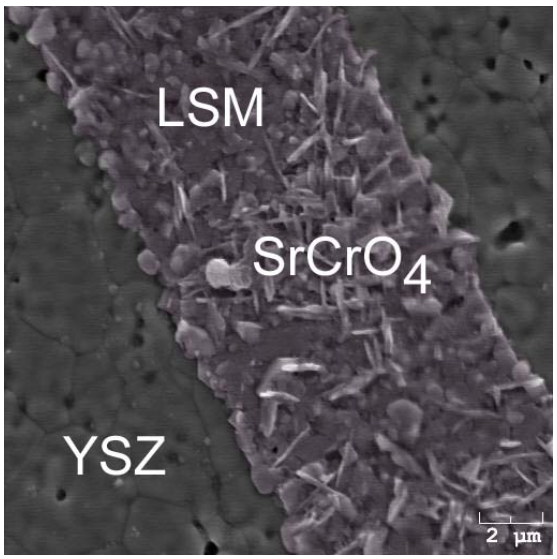

(b)

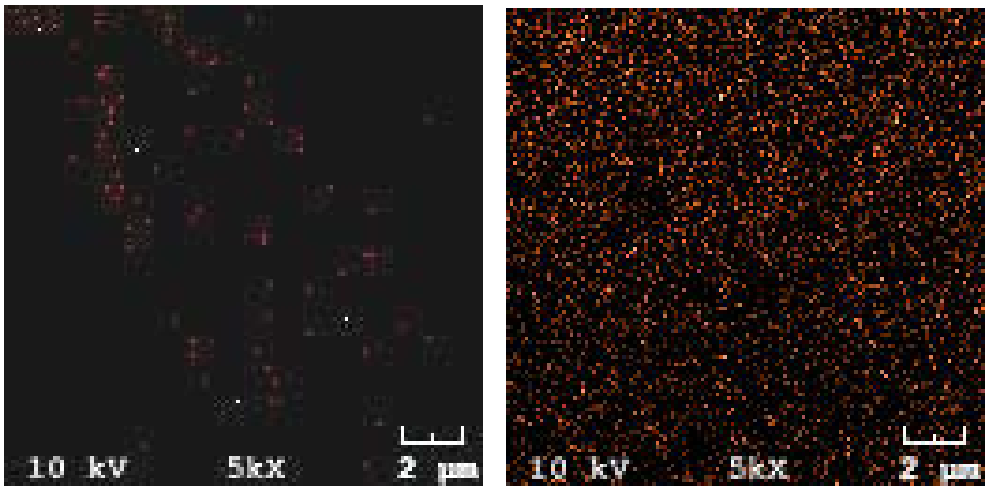

Figure 7.4. (a) SEM micrograph showing the presence of SrCrO4 on the patterned LSM electrode. (b) EDS mapping of Cr and Sr from the area shown in the micrograph.

These initial results indicate a chemical reaction between some Cr-containing vapor phase and LSM to form $SrCrO_4$ and possibly $(Mn/Cr)_3O_4$. The tested samples were not polarized, so it is not known whether different contaminants would form through a competing electrochemical pathway or through reduction of $SrCrO_4$ (a Cr^{+6} species).

7.3. Chromium poisoning of Ag-containing cathodes

7.3.1. The use of silver in SOFC cathodes

To improve cathode performance in the intermediate temperature range, alternative materials are being pursued to increase the cathode's catalytic activity towards oxygen reduction. As discussed in section 4.1, the guiding strategy for this goal has been to incorporate mixed ionic/electronic conduction into the cathode, extending the oxygen reduction reaction beyond the triple phase boundary (TPB) between the gas, cathode, and electrolyte phases to include the entire gas/cathode interface. Besides the perovskite-based cathode materials studied here (e.g., LSM, LSF, SSC), other single mixed conducting phases have been explored, including Ru-based pyrochlores[128, 129] and K_2NiF_4-type oxides.[130, 131]

Alternatively, two-phase cathodes have been studied that use a strictly ionic or mixed conducting oxide phase coupled with a noble metal such as Pd, Pt, or Ag.[132] The noble metal phase boosts the electronic conductivity of the cathode while still providing a surface that is active towards oxygen reduction. As cost is the driving force to lowering the SOFC operating temperature, silver is the preferred candidate amongst the noble metals. Silver had been previously disregarded as a cathode material due to its low melting point (962ºC), making it susceptible to vaporization at the higher operating temperatures of conventional SOFC systems,[133] but it once again becomes viable in the desired lower temperature range. So far, the addition of Ag to SOFC cathodes has generated mixed results. Haanapel, et al., reported that the sintering temperature restrictions imposed by silver lessens the performance of a cell compared to that of an optimized Ag-free cell.[132] Also, Camaratta, et al., observed unstable performances in their

Ag- and bismuth oxide-based cathodes due to silver grain growth under operating conditions.[134] In contrast, many groups have measured an improved cathode performance with the addition of small amounts of silver.[88, 135-139] In addition, silver is often used as current collector (mesh or paste), electrical contact (paste), or lead wire when measuring the electrochemical performance of low-temperature SOFCs.

The previous studies on the addition of silver to the cathode (or studies that used Ag elsewhere within an SOFC) only involved single cell tests. No serious consideration was given to possible interactions between the silver phase and a metallic interconnect layer. Since silver can react with Cr_2O_3 to form phases such as Ag_2CrO_4 and $AgCrO_2$,[140] the possible Cr contamination of silver phase poses a serious concern. Formation of secondary Ag-Cr phases reduces the electrical conduction throughout the cathode and the available surface area catalytically active towards oxygen reduction.

7.3.2. Formation of Ag_2CrO_4 on Ag-containing cathodes

To measure the effect of Cr-containing vapor on a silver, a piece of silver mesh was placed on top of a pellet of gadolinia-doped ceria (GDC), a candidate SOFC electrolyte material. The pellet was then placed on the sample cup inside the sample chamber and heated to 500ºC, holding the temperature every 50ºC to collect spectra from various locations on the silver surface. The GDC pellet acted as a buffer to prevent direct contact between the silver and stainless steel, eliminating solid-state reactions between the oxide layer on the stainless steel and the wire. Any chromium contamination observed on the mesh would thus result from reaction with Cr-containing vapor.

Figure 7.5 contains typical Raman spectra collected at different temperatures from the surface of the silver mesh exposed to Cr-containing humidified air. Raman spectra were collected in 50ºC intervals after 30 minutes at the desired temperature, with no anomalous Raman signals detected until the mesh reached 500ºC. At this temperature, a broad peak centered at 820 cm^{-1} was observed at certain points on the mesh. The sample was then cooled to room temperature, so that the chamber could be opened and the sample surface observed more clearly. Small brownish-red particles, the dark particles shown on the Ag surface in Fig. 7.5(b), had developed on the silver surface. The color matches that of silver chromate, Ag_2CrO_4.[141] The peaks in the Raman spectrum in Fig. 7.5(a) from one of the particles match those of orthorhombic Ag_2CrO_4, as reported by Clark and Dines.[142] The reference spectrum shown was collected at room temperature from Ag_2CrO_4 powder purchased from Alfa Aesar. The family of peaks centered around 810 cm^{-1} from the room temperature spectra shift, broaden, and merge together with increasing temperature, resulting in the single broad feature observed in the *in situ* spectrum collected at 500ºC. This effect was confirmed by measuring the Raman spectrum of a pressed Ag_2CrO_4 powder compact as a function of temperature within the Raman sample chamber (see Appendix C).

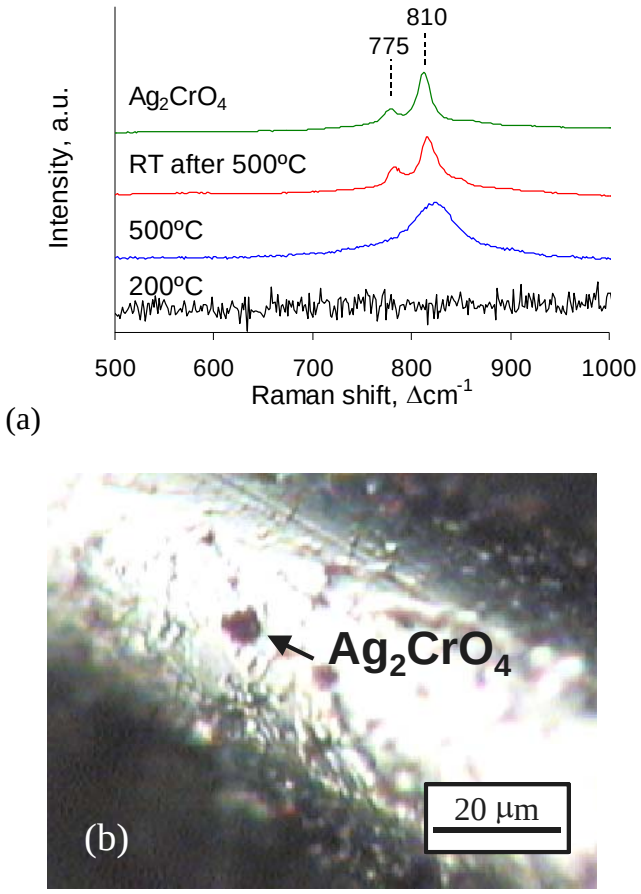

Figure 7.5. (a) Raman spectra from silver mesh exposed to Cr-containing vapor at different temperatures compared to that of Ag_2CrO_4 powder. (b) Optical micrograph of red deposit on silver mesh from which the room temperature spectrum in (a) after cooling from 500ºC.

Abu-Zied observed the formation Ag_2CrO_4 at 300ºC when reacting Cr_2O_3 and $AgNO_3$ in air through a CrOOH intermediate.[140] Our Raman measurements did not detect the presence of Ag_2CrO_4 until 500ºC. This discrepancy can be explained by the higher reactivity of $AgNO_3$, which decomposes at 500ºC, and by the more intimate contact between the Cr and Ag sources in Abu-Zied's experiments. Our experiment relied upon a gas-solid interaction, and the vapor pressures of chromia and chromium oxyhydroxides are low below 800ºC.[125] Also, during heating, our sample was only held for 30 minutes at each temperature before collecting a Raman spectrum. Longer exposure times at lower

temperatures may result in detection of Ag_2CrO_4 formation at these temperatures. As the objective of this study was to mimic intermediate temperature SOFC operating conditions, the presence of Ag_2CrO_4 at 500ºC, the lower end of intermediate temperature range, is significant.

If an SOFC stack utilizing stainless steel interconnects were operated at 500ºC, any exposed silver surface in the cathode transform into Ag_2CrO_4. Since Ag_2CrO_4 is conductive at this temperature, its formation does not interfere significantly with the use of Ag as an electronically conductive phase in the cathode. What may be impacted is the catalytic activity of the Ag towards oxygen reduction, which is lowered as the Ag surface converts to Ag_2CrO_4. Of greater concern is the melting point of Ag_2CrO_4, 658ºC.[143] Its melting point is lower than that of silver, 962ºC. Within even lower SOFC operating temperatures, the Ag_2CrO_4 could melt or volatilize. The continual loss of Ag_2CrO_4 to vaporization would eventually weaken the contact between the silver phase, the interconnect, and the other cathode phase. It could also contaminate other parts of the cell through condensation or chemical reaction.

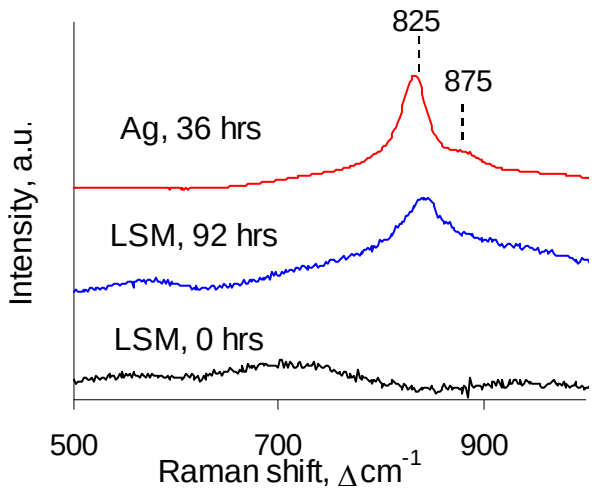

Figure 7.6. Raman spectra from a patterned LSM electrode on a YSZ substrate collected *in situ* at 625ºC during exposure to Cr vapor. The LSM spectra were measured on surfaces close to where the Ag wire was attached to the sample.

The effect of the vaporization of Ag_2CrO_4 was tested by performing Cr contamination experiments on patterned LSM cathode samples onto a silver wire had been attached using silver paste (Heraeus). Figure 7.6 contains Raman spectra collected *in situ* at 625ºC from such a sample exposed to Cr-containing vapor. Within 36 hours, the signal from Ag_2CrO_4 on the silver wire was very intense. The slight shoulder at 875 cm^{-1}, which was not detected on the Ag wire when heated without LSM present, is attributed to $SrCrO_4$.

Within four days exposure, reddish-brown Ag_2CrO_4 crystals, which could be observed visually on the Ag wire, began to form on the LSM electrode to which the Ag wire was attached. The Raman spectrum from the LSM had a broad peak centered at 830 cm^{-1}. The Ag_2CrO_4 deposited on the LSM through vaporization and condensation. The shift in the peak position could result from a defective structure caused by the deposition of the Ag_2CrO_4 onto the LSM perovskite surface.

Further evidence of Ag_2CrO_4 vaporization is shown in the optical micrograph in Figure 7.7(a) taken at room temperature after exposure to Cr vapor at 625ºC for three weeks. A room temperature micrograph obtained after cooling is shown here because the *in situ* images taken were blurry due to the sample temperature and to the quartz window between the objective and the sample. In the image, the silver wire crosses the upper left corner while the platinum current collector runs across the upper right corner. The lighter regions are the YSZ substrate. The red Ag_2CrO_4 phase can be seen visually on the LSM, but not on the YSZ regions between the LSM strips.

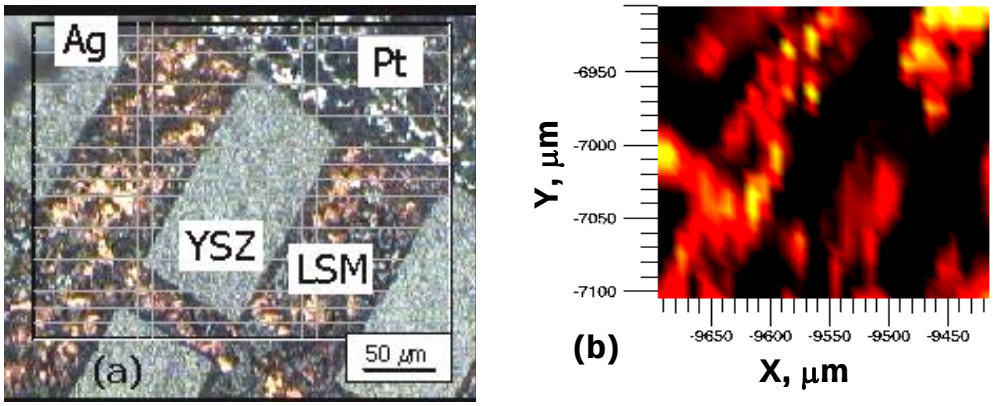

Figure 7.7. (a) Optical micrograph detailing area on patterned LSM sample to collect Raman map (b) plotting the integrated intensity of the 810 cm^{-1} Raman peak. The lighter regions are YSZ, the cross-hatched electrode is LSM, and the strip across the upper right corner is platinum. The Ag wire can be seen in the upper left corner. A lighter shade in the map indicates a higher intensity.

A Raman map of the Ag_2CrO_4 phase was generated by collecting a Raman spectrum every 10 μm within the 200 μm x 280 μm grid detailed in Fig. 7.7(a). The integrated peak intensity of the 810 cm^{-1} Ag_2CrO_4 peak was calculated from each spectrum and plotted as a function of position. The presence of the 810 cm^{-1} peak correlates with the presence of the red deposit on the LSM. The sample was further

examined *ex situ* using SEM. The SEM image in Figure 7.8(a) shows the morphology of the LSM surface. The corresponding Ag EDS map in Fig. 7.8(b) confirms the existence of a silver-containing phase on the electrode surface.

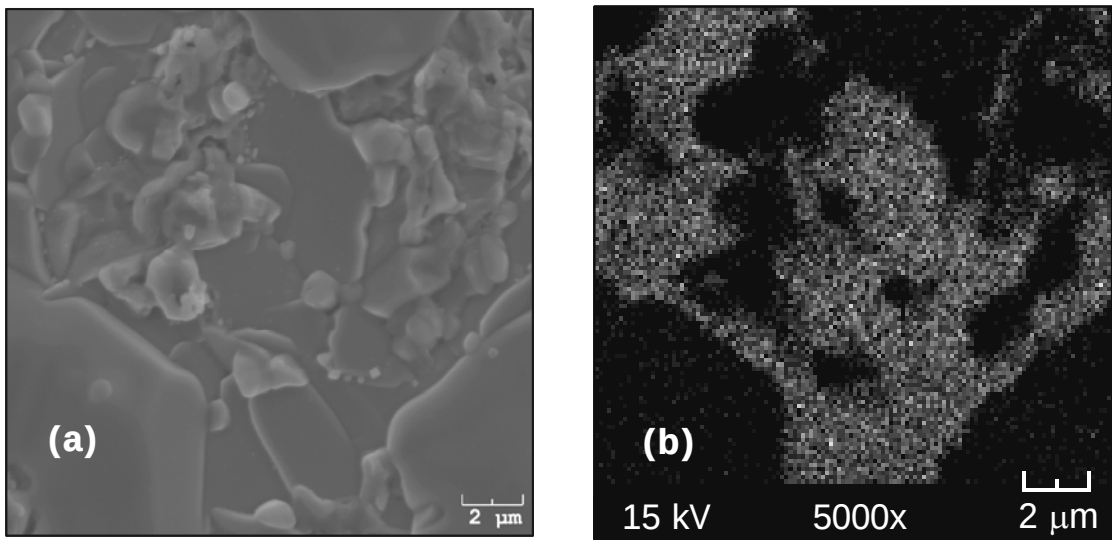

Figure 7.8. (a) SEM micrograph showing contaminated LSM surface. (b) EDS showing presence of silver from area shown in (a). The lighter areas indicate higher concentrations of Ag. A lighter shade indicates a greater Ag concentration.

The lack of any appreciable Ag_2CrO_4 signal on the YSZ surface eliminates the possibility of a surface diffusion mechanism, as some Ag_2CrO_4 would have been trapped on the YSZ during the quenching of the sample to room temperature. Instead, the Ag_2CrO_4 vaporized from the Ag wire surface and deposited preferentially on the LSM. The author cannot definitively explain the affinity between Ag_2CrO_4 and LSM. The positive driving force for $SrCrO_4$ formation (or some mixed Ag_2CrO_4-$SrCrO_4$ phase) may promote the adsorption of Ag_2CrO_4 to the LSM surface. To test this hypothesis, a similar experiment could be performed with a cathode material that does not contain a cation species such as strontium (or manganese) that reacts with chromium.

The deposition of Ag_2CrO_4 on LSM is significant since it eliminates active LSM surface area that could be used for oxygen reduction. For the sample shown in Fig. 7.7, Ag_2CrO_4 was detected up to 500 μm away from the silver source after the three weeks of exposure to Cr vapor. For SOFCs with stainless steel interconnects and cathodes containing a mixture of silver and another phase, Ag_2CrO_4 can quickly cover the surrounding surfaces throughout the entire cathode. Even if a layer of silver is used in an SOFC stack as a buffer layer between the interconnect and the cathode (in principle, to help prevent Cr contamination of the cathode), Ag_2CrO_4 vapor could still permeate throughout most of the cathode within 1000 hrs of operation, as most cathodes are between 10 and 100 μm thick.

Both sets of experiments detailed here involved *chemical* exposure of silver and an SOFC cathode to Cr vapor. While the temperature and atmospheric conditions of an intermediate temperature SOFC were duplicated in our sample chamber, the sample was not polarized electrically to observe *electrochemical* exposure. Although the formation of $SrCrO_4$ and the $(Mn/Cr)_3O_4$ spinel man be promoted electrochemically, Ag_2CrO_4 forms at such low temperatures that the effects of its formation will be felt before the cell reaches its operating temperature and a current is applied. Further, the formation of other Cr phases would only replace or add to the contamination caused by Ag_2CrO_4. However, as Ag_2CrO_4, like $SrCrO_4$, is a Cr^{+6} species, the possibility that silver chromate could be reduced to other phases such as $AgCrO_2$ or Cr_2O_3.

7.4. Conclusions

Raman spectroscopy was able to monitor the contamination of SOFC cathodes by volatile chromium species. Strontium chromate, $SrCrO_4$, formed on the surface of LSM. Its formation was chemically-driven, so the material is subject to contamination whether or not the cell is operating. Further, contamination would begin during the system heatup. Similar contamination tests should be performed other strontium-containing cathode materials (e.g., LSF, LSC) to see if strontium can be stabilized within the lattice by doping to hinder the formation of $SrCrO_4$. Silver chromate, Ag_2CrO_4, was formed on the surface of silver wire exposed to Cr-containing vapor at temperatures as low as 500ºC. By 625ºC, the Ag_2CrO_4 was already vaporizing and depositing on the surface of an LSM electrode. The volatility of Ag_2CrO_4 under the operating conditions of an intermediate temperature SOFC would weaken the electrical contact between the silver and the rest of the cell, as well as reduce the catalytic activity of the cathode by covering its surface. In light of these effects, one should avoid using silver within an SOFC cathode in contact with an interconnect layer that forms a Cr_2O_3 layer on its surface, as with most stainless steels. The use of silver in a low-temperature SOFC must be in conjunction with an interconnect material that does not form a Cr_2O_3 surface layer. Alternatively, conductive (but passive) coatings can be applied to the stainless steel surface to prevent the volatilization of chromium from the alloy.

CHAPTER 8: CONCLUSIONS AND RECOMMENDATIONS

There were two overall objectives of the research done in support of this thesis. First, the author wanted to demonstrate the utility of Raman spectroscopy with respect to solid oxide fuel cells, in particular, and, more generally, high temperature catalyst and electrochemical systems. The work presented here undeniably confirms this assertion. The bulk of the materials used in SOFCs are Raman-active, and as a minimum, Raman spectroscopy can serve as a quick, flexible method of characterizing the structure and composition of SOFC components. The optical nature of Raman measurements even allows for relatively straightforward *in situ* characterization of SOFC components by using a setup similar to the sample chamber described here. Such measurements are much more difficult to make with X-ray methods, and some materials (such as amorphous carbon and glassy sealant materials) are not even detectable using XRD. Further, the high operating temperatures of SOFCs makes IR spectroscopy (like Raman spectroscopy, another form of vibrational spectroscopy) difficult, as the sample itself emits a large amount of graybody IR radiation. While Raman spectroscopy cannot provide all the information desired by scientists and engineers, it does provide some unique structural information and can be used to confirm results obtained by other methods.

Besides characterizing SOFC components, Raman spectroscopy can be used (both *in situ* and *ex situ*) to monitor the stability of the components under a variety of operating conditions and in the presence of a variety of contaminants. As the Raman signal from a material can broaden and weaken with temperature, the results shown here (as with

carbon and the different chromium contaminants) indicate that these signals are still detectable within the desired temperature range of intermediate temperature SOFCs.

However, any Raman data must be understood within the limitations of the system. First, the absence of a signal is not necessarily indicative of the absence of a species. Not all materials (e.g., cubic perovskite materials) are Raman-active, so other methods are required to characterize them. Some materials, even though theoretically Raman-active, are still not detectable. The author was not able to successfully measure surface oxygen species on SOFC cathode materials. Surely there is oxygen on the cathode surface; oxygen is continually entering and leaving the lattice of these materials. Group theory and similar measurements with other materials dictates that these species are Raman-active. Only, for normal Raman spectroscopy methods, the signal is apparently not strong enough to be detected at room temperature or above. The initial results using colloids and vapor deposition methods to produce a SERS effect show some promise when it comes to boosting the Raman signal from cathode surfaces.

The second large objective of this research was to use Raman spectroscopy to provide valuable mechanistic information about various chemical and electrochemical reactions occurring within SOFCs. This information would be intended for use directly in the rational design of new SOFC materials and microstructures. The results regarding this objective were mixed. The species involved in the oxygen reduction mechanism at the cathode remain elusive. Again, SERS measurements may be able to overcome current system limitations, especially if the gold or silver nanoparticles can maintain their utility up to plausible SOFC operating temperatures. If not, SERS can be used for *ex situ* surface analysis. In terms of identifying thin films of contaminant species, this information could

still provide structural and compositional information that is sometimes difficult to obtain through XRD, EDS, and XPS. In terms of identifying surface species, low temperature data can be used to validate theoretical models and provide key parameters for these models. The models can then be used to calculate species and barriers present under operating conditions.

In terms of information readily applicable to SOFC system design, the chromium data stands as most relevant. As $SrCrO_4$ was found to quickly form in the presence of Cr-containing vapor, either strontium use should be limited within a cathode (unless it can be sufficiently stabilized within the lattice using other dopants) or the volatility of chromium from the metallic interconnect should be curbed. This could be done by altering the alloy composition or by applying a surface treatment to the metal, being mindful that any thin film applied to the interconnect must still be electronically-conductive. The Cr poisoning of silver also calls into question the use of silver inside the cathode unless chromium can be prevented from leaving the interconnect material.

All the results presented within this volume represent initial investigations into multiple applications of Raman spectroscopy. As such, there are many avenues of research that can be followed from here. For SERS measurements, initial experiments involving the sputtering of Ag/Au nanoparticles onto electrode surfaces should still be done. While colloids and CCVD have yielded some positive results, it would be even better to find another possible method for getting metal nanoparticles onto the electrode surface. The spectra obtained from SERS methods need to be studied more, possibly coupled with quantum chemical calculations to fully understand the nature of the large number of new peaks. The properties of the metal nanoparticles need to be measured as a

function of temperature and atmosphere (oxidizing and reducing) to define the operating conditions in which SERS can be used to monitor fuel cell reactions. Even if SERS measurements cannot ultimately be made in the upper range of SOFC operating temperatures, SERS should be seriously considered with respect to PEMFCs and other catalytic systems that operate below 300ºC.

For both carbon deposition and chromium contamination, the results reported here involved OCV conditions only. Fuel cells are electrochemical devices, and as such, the addition of a potential across a cell changes the system. Some contaminants can be eliminated, such as the oxidation of carbon, while others may transform to other species, such as the reduction of some of the chromium contaminants. Raman measurements need to be taken from polarized samples to gain a more accurate picture of the species present in an operating cell. A wider selection of electrode materials should be tested as well, to gauge the resilience or susceptibility of different compositions and crystal structures to different degradation processes.

The ability to simultaneously record spectroscopic and electrochemical data is an exciting development. This more relevant data can only help in the development of new materials using a more rational approach.

APPENDIX A: LATTICE PHONON MODES OF COMMON SOFC MATERIALS AND POSSIBLE CONTAMINANTS

Material	Space Group	Raman Modes*	IR Modes*	Silent Modes*
CeO_2 / GDC	225 ($Fm\bar{3}m$)	F_{2g}	F_{1u}	none
YSZ	225 ($Fm\bar{3}m$)	F_{2g}	F_{1u}	none
NiO	225 ($Fm\bar{3}m$)	none	F_{1u}	none
SSC	62 (Pnma)	$7 A_g + 5 B_{1g} + 7 B_{2g} + 5 B_{3g}$	$9 B_{1u} + 7 B_{2u} + 9 B_{3u}$	$8 A_u$
LSM	62 (Pnma)	$7 A_g + 5 B_{1g} + 7 B_{2g} + 5 B_{3g}$	$9 B_{1u} + 7 B_{2u} + 9 B_{3u}$	$8 A_u$
LSF	62 (Pnma)	$7 A_g + 5 B_{1g} + 7 B_{2g} + 5 B_{3g}$	$9 B_{1u} + 7 B_{2u} + 9 B_{3u}$	$8 A_u$
LSC	167 ($R\bar{3}c$)	$A_{1g} + 4 E_g$	$3 A_{2u} + 5 E_u$	$2 A_{1u} + 3 A_{2g}$
LSCF	167 ($R\bar{3}c$)	$A_{1g} + 4 E_g$	$3 A_{2u} + 5 E_u$	$2 A_{1u} + 3 A_{2g}$
$AgCrO_2$	166 ($R\bar{3}m$)	$A_{1g} + E_g$	$2 A_{2u} + 2 E_u$	none
Ag_2CrO_4	62 (Pnma)	$11 A_g + 7 B_{1g} + 11 B_{2g} + 7 B_{3g}$	$13 B_{1u} + 9 B_{2u} + 13 B_{3u}$	$10 A_u$
$(Mn/Cr)_3O_4$	227 ($Fd\bar{3}m$)	$A_{1g} + E_g + 3 F_{2g}$	$4 F_{1u}$	$2 A_{2u} + 2 E_u + F_{1g} + 2 F_{2u}$
$SrCrO_4$	14 ($P2_1/n$)	$18 A_g + 18 B_g$	$17 A_u + 16 B_u$	none
Cr_2O_3	167 ($R\bar{3}c$)	$2 A_{1g} + 5 E_g$	$2 A_{2u} + 4 E_u$	$2 A_{1u} + 3 A_{2g}$
C (graphite)	194 ($P6_3/mmc$)	E_{2g}	none	B_{2g}
C (diamond)	227 ($Fd\bar{3}m$)	F_{2g}	none	none

***** This table lists the phonon modes which are either Raman-active, IR-active, or neither (silent). It is also possible to have modes which are **both** Raman- and IR-active; however, none of the listed phases have any such modes.

APPENDIX B: RAMAN SPECTRA OF COMPOSITIONS WITHIN THE LAMNO3 – SRMNO3 SERIES

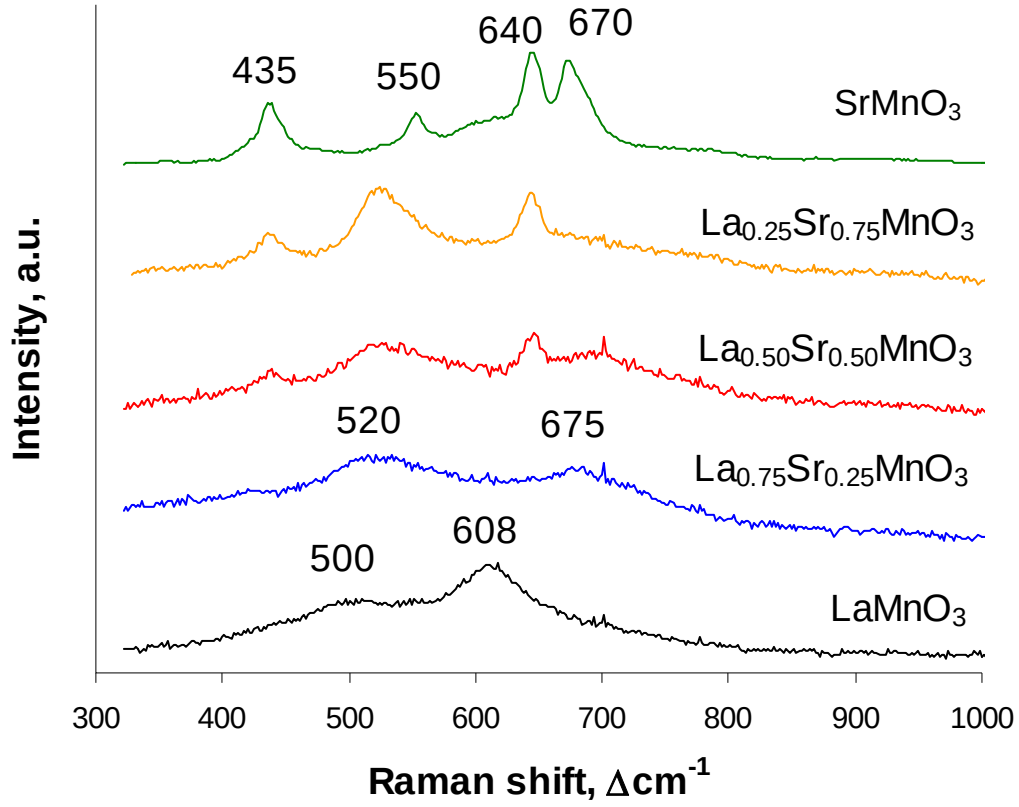

* Raman spectra were collected at room temperature in air using a 514 nm laser source. Sample powders were synthesized using the glycine-nitrate process.[86] Above ~30 mol% $SrMnO_3$, the crystal structure shifts from an orthorhombically-distorted perovskite ($LaMnO_3$ base structure) to a rhombohedrally-distorted perovskite ($SrMnO_3$ base structure).

APPENDIX C: RAMAN SPECTRA OF AG2CRO4 AS A FUNCTION OF TEMPERATURE

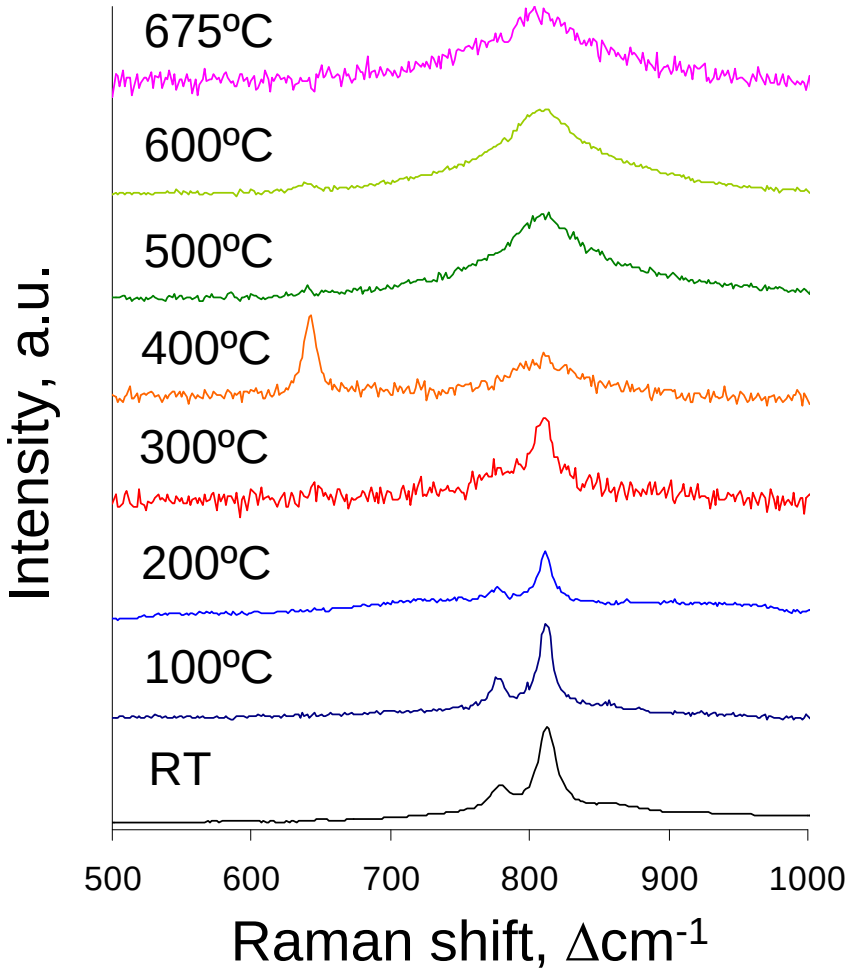

* Raman spectra were collected at the indicated heating cartridge temperature using a 514 nm laser source. The Ag2CrO4 source was powder purchased from Alfa Aesar. The same collection time was used for all spectra. The author believes the peaks at 640 cm^{-1} appearing in the 500-600ºC range correspond to oxygen deficiencies in the lattice, as the peak corresponds with the $AgCrO_2$ phase.

REFERENCES

1. Energy, U. S. D. o., Annual Energy Review 2006. In Administration, E. I., Ed. Washington, 2007; p 441.
2. Minh, N. Q.; Takahashi, T., *Science and Technology of Ceramic Fuel Cells*. Elsevier: Amsterdam, 1995.
3. Ormerod, R. M., "Solid oxide fuel cells," *Chemical Society Reviews* **2003** 32, (1), 17-28.
4. Gellings, P. J.; Bouwmeester, H. J. M., *The CRC Handbook of Solid State Electrochemistry*. CRC Press: New York, 1996; p 630.
5. Choy, K.; Bai, W.; Clarojrochkul, S.; Steele, B. C. H., "The development of intermediate-temperature solid oxide fuel cells for the next millennium," *Journal of Power Sources* **1998** 71, (1-2), 361-369.
6. McEvoy, A. J., "Thin SOFC electrolytes and their interfaces - A near-term research strategy," *Solid State Ionics* **2000** 132, (3-4), 159-165.
7. Xia, C.; Rauch, W.; Chen, F.; Liu, M., "$Sm_{0.5}Sr_{0.5}CoO_3$ cathodes for low-temperature SOFCs," *Solid State Ionics* **2002** 149, (1,2), 11-19.
8. Adler, S. B., "Factors governing oxygen reduction in solid oxide fuel cell cathodes," *Chemical Reviews* **2004** 104, (10), 4791-4843.
9. Badwal, S. P. S.; Deller, R.; Foger, K.; Ramprakash, Y.; Zhang, J. P., "Interaction between chromia forming alloy interconnects and air electrode of solid oxide fuel cells," *Solid State Ionics* **1997** 99, (3-4), 297-310.
10. Jiang, S. P.; Zhang, J. P.; Zheng, X. G., "A comparative investigation of chromium deposition at air electrodes of solid oxide fuel cells," *Journal of the European Ceramic Society* **2002** 22, (3), 361-373.
11. Kurokawa, H.; Kawamura, K.; Maruyama, T., "Oxidation behavior of Fe-16Cr alloy interconnect for SOFC under hydrogen potential gradient," *Solid State Ionics* **2004** 168, (1-2), 13-21.
12. Krumpelt, M.; Krause, T. R.; Carter, J. D.; Kopasz, J. P.; Ahmed, S., "Fuel processing for fuel cell systems in transportation and portable power applications," *Catalysis Today* **2002** 77, (1-2), 3-16.
13. Ray, E. R.; Maskalick, N. J.; Spengler, C. J. *Contaminant effects in solid oxide fuel cells*; Westinghouse Sci. Technol. Cent.,Pittsburgh,PA,USA.: 1991; pp 108-16.
14. Macdonald, J. R.; Barsoukov, E., *Impedance Spectroscopy: Theory, Experiment, and Applications*. 2nd ed.; Wiley-Interscience: Hoboken, N.J., 2005; p 595.
15. Liu, M. L., "Equivalent circuit approximation to porous mixed-conducting oxygen electrodes in solid-state cells," *Journal Of The Electrochemical Society* **1998** 145, (1), 142-154.
16. Michihisa, K.; Ching-ju, W.; Takuya, M.; Junichiro, O.; Hiroshi, F.; Koichi, Y.; Koichi, E.; Hiroshi, T., "The Mechanism of Porous Sm[sub 0.5]Sr[sub 0.5]CoO[sub 3] Cathodes Used in Solid Oxide Fuel Cells," *Journal Of The Electrochemical Society* **2001** 148, (7), A795-A801.
17. Cheng, Z.; Liu, M., "Characterization of sulfur poisoning of Ni-YSZ anodes for solid oxide fuel cells using in situ Raman microspectroscopy," *Solid State Ionics* **2007** 178, (13-14), 925-935.

18. Stierle, A.; Molenbroek, A. M., "Novel In Situ Probes for Nanocatalysis," *MRS Bulletin* **2007** 32, 1001-1005.
19. Cheng, Z. Investigation into the Interactions between Sulfur and Anodes for Solid Oxide Fuel Cells. Ph.D., Georgia Institute of Technology, Atlanta, GA, 2008.
20. Loudon, R., "RAMAN EFFECT IN CRYSTALS," *Advances in Physics* **1964** 13, (52), 423-&.
21. Long, D. A., *Raman Effect: A Unified Treatment of Raman Scattering by Molecules*. Wiley: Chichester, New York, 2002; p 597.
22. Smith, E.; Dent, G., *Modern Raman Spectroscopy: A Practical Approach*. Wiley: Hoboken, NJ, 2005; p 210.
23. Nakamoto, K., *Infrared and Raman Spectra of Inorganic and Coordination Compounds Part A: Theory and Applications in Inorganic Chemistry*. 5th ed.; John Wiley & Sons, Inc.: New York, 1997; Vol. A, p 387.
24. Banares, M. A., Raman Spectroscopy. In *In Situ Spectroscopy of Catalysts*, Weckhuysen, B. M., Ed. American Scientific Publishers: USA, 2004; p 332.
25. Bishop, D. M., *Group Theory and Chemistry*. Dover Publications, Inc.: New York, NY, 1973; p 300.
26. Fateley, W. G., *Infrared and Raman Selection Rules for Molecular and Lattice Vibrations: The Correlation Method*. Wiley-Interscience: New York, NY, 1972; p 222.
27. Rousseau, D. L.; Bauman, R. P.; Porto, S. P. S., "NORMAL MODE DETERMINATION IN CRYSTALS," *Journal of Raman Spectroscopy* **1981** 10, (JAN), 253-290.
28. Hahn, T., *International Tables for Crystallography*. 5th ed.; Kluwer: Dordrecht, 2002; Vol. A, p 911.
29. Pomfret, M. B.; Stoltz, C.; Varughese, B.; Walker, R. A., "Structural and compositional characterization of yttria-stabilized zirconia: Evidence of surface-stabilized, low-valence metal species," *Analytical Chemistry* **2005** 77, 1791-1795.
30. Gupta, R. K.; Whang, C. M., "Structural study of a sol-gel derived novel solid oxide fuel cell perovskite: (La1-xSrx)(Cr0.85Fe0.05Co0.05Ni0.05)O3-delta," *Journal of Physics-Condensed Matter* **2007** 19, (19).
31. Iliev, M. N.; Litvinchuk, A. P.; Abrashev, M. V.; Ivanov, V. G.; Lee, H. G.; McCarroll, W. H.; Greenblatt, M.; Meng, R. L.; Chu, C. W., "Raman monitoring of the dynamical Jahn-Teller distortions in rhombohedral antiferromagnetic LaMnO3 and ferromagnetic magnetoresistive La0.98Mn0.96O3," *Physica C* **2000** 341, 2257-2258.
32. Podobedov, V. B.; Weber, A.; Romero, D. B.; Rice, J. P.; Drew, H. D., "Effect of structural and magnetic transitions in La1-xMxMnO3 (M=Sr, Ca) single crystals in Raman scattering," *Physical Review B* **1998** 58, (1), 43-46.
33. Nemanich, R. J.; Glass, J. T.; Lucovsky, G.; Shroder, R. E., "RAMAN-SCATTERING CHARACTERIZATION OF CARBON BONDING IN DIAMOND AND DIAMONDLIKE THIN-FILMS," *Journal of Vacuum Science & Technology a-Vacuum Surfaces and Films* **1988** 6, (3), 1783-1787.
34. Ferrari, A. C.; Meyer, J. C.; Scardaci, V.; Casiraghi, C.; Lazzeri, M.; Mauri, F.; Piscanec, S.; Jiang, D.; Novoselov, K. S.; Roth, S.; Geim, A. K., "Raman spectrum of graphene and graphene layers," *Physical Review Letters* **2006** 97, (18), 4.

35. Schwan, J.; Ulrich, S.; Batori, V.; Ehrhardt, H.; Silva, S. R. P., "Raman spectroscopy on amorphous carbon films," *Journal of Applied Physics* **1996** 80, (1), 440-447.
36. Dresselhaus, M. S.; Dresselhaus, G.; Saito, R.; Jorio, A., "Raman spectroscopy of carbon nanotubes," *Physics Reports-Review Section of Physics Letters* **2005** 409, (2), 47-99.
37. Pomfret, M. B.; Owrutsky, J. C.; Walker, R. A., "High-temperature Raman spectroscopy of solid oxide fuel cell materials and processes," *Journal of Physical Chemistry B* **2006** 110, (35), 17305-17308.
38. Pomfret, M. B.; Owrutsky, J. C.; Walker, R. A., "In situ studies of fuel oxidation in solid oxide fuel cells," *Analytical Chemistry* **2007** 79, (6), 2367-2372.
39. Farrow, R. L.; Benner, R. E.; Nagelberg, A. S.; Mattern, P. L., "Characterization of Surface Oxides by Raman-Spectroscopy," *Thin Solid Films* **1980** 73, (2), 353-358.
40. Maslar, J. E.; Hurst, W. S.; Bowers, W. J.; Hendricks, J. H.; Aquino, M. I.; Levin, I., "In situ Raman spectroscopic investigation of chromium surfaces under hydrothermal conditions," *Applied Surface Science* **2001** 180, (1-2), 102-118.
41. Wijesinghe, T.; Blackwood, D. J., "Characterisation of passive films on 300 series stainless steels," *Applied Surface Science* **2006** 253, (2), 1006-1009.
42. Ingram, B. J.; Cruse, T. A.; Krumpelt, M., "Potassium-assisted chromium transport in solid oxide fuel cells," *Journal of The Electrochemical Society* **2007** 154, B1200-B1205.
43. Koep, E.; Compson, C.; Liu, M. L.; Zhou, Z. P., "A photolithographic process for investigation of electrode reaction sites in solid oxide fuel cells," *Solid State Ionics* **2005** 176, (1-2), 1-8.
44. Koep, E.; Jin, C.; Haluska, M.; Das, R.; Narayan, R.; Sandhage, K.; Snyder, R.; Liu, M., "Microstructure and electrochemical properties of cathode materials for SOFCs prepared via pulsed laser deposition," *Journal of Power Sources* **2006** 161, (1), 250-255.
45. Koep, E.; Mebane, D. S.; Das, R.; Compson, C.; Liu, M., "Characteristic thickness for a dense $La_{0.8}Sr_{0.2}MnO_3$ electrode," *Electrochemical and Solid State Letters* **2005** 8, (11), A592-A595.
46. Koep, E. A quantitative determination of electrode kinetics using micropatterned electrodes. Ph.D., Georgia Institute of Technology, Atlanta, GA, 2006.
47. Fleig, J., "Solid oxide fuel cell cathodes: Polarization mechanisms and modeling of the electrochemical performance," *Annual Review Of Materials Research* **2003** 33, 361-382.
48. Choi, Y. M.; Mebane, D. S.; Lin, M. C.; Liu, M., "Oxygen Reduction on $LaMnO_3$-Based Cathode Materials in Solid Oxide Fuel Cells," *Chemistry of Materials* **2007** 19, (7), 1690-1699.
49. Kilner, J. A.; DeSouza, R. A.; Fullarton, I. C., "Surface exchange of oxygen in mixed conducting perovskite oxides," *Solid State Ionics* **1996** 86-8, 703-709.
50. McEvoy, A. J., "Materials for high-temperature oxygen reduction in solid oxide fuel cells," *Journal Of Materials Science* **2001** 36, (5), 1087-1091.
51. Singhal, S. C., "Advances in solid oxide fuel cell technology," *Solid State Ionics* **2000** 135, (1-4), 305-313.
52. Kroger, F. A., *The Chemistry of Imperfect Crystals*. 2nd ed.; American Elsevier: New York, 1974; Vol. 2.

53. Vetter, K. J., *Electrochemical Kinetics, Theoretical and Experimental Aspects*. Academic Press: New York, 1967; p 789.
54. Takeda, Y.; Kanno, R.; Noda, M.; Tomida, Y.; Yamamoto, O., "Cathodic Polarization Phenomena Of Perovskite Oxide Electrodes With Stabilized Zirconia," *Journal Of The Electrochemical Society* **1987** 134, (11), 2656-2661.
55. Chen, C. C.; Nasrallah, M. M.; Anderson, H. U., "IMMITTANCE RESPONSE OF LA0.6SR0.4CO0.2FE0.8O3 BASED ELECTROCHEMICAL-CELLS," *Journal of The Electrochemical Society* **1995** 142, (2), 491-496.
56. Ishihara, T.; Honda, M.; Shibayama, T.; Minami, H.; Nishiguchi, H.; Takita, Y., "Intermediate temperature solid oxide fuel cells using a new LaGaO3 based oxide ion conductor - I. Doped SmCoO3 as a new cathode material," *Journal of The Electrochemical Society* **1998** 145, (9), 3177-3183.
57. Sunde, S., "Simulations of composite electrodes in fuel cells," *Journal Of Electroceramics* **2000** 5, (2), 153-182.
58. Liu, M., "Distributions of charged defects in mixed ionic-electronic conductors. I. General equations for homogeneous mixed ionic-electronic conductors," *Journal of The Electrochemical Society* **1997** 144, (5), 1813-1834.
59. Liu, M.; Winnick, J., "Fundamental issues in modeling of mixed ionic-electronic conductors (MIECs)," *Solid State Ionics* **1999** 118, (1,2), 11-21.
60. Suetaka, W.; Yates, J. T., "Surface Infrared and Raman Spectroscopy: Methods and Applications," **1995**, 270.
61. Davydov, A. A., *Molecular Spectroscopy of Oxide Catalyst Surfaces*. First ed.; John Wiley & Sons, Ltd.: West Sussex, England, 2003; p 668.
62. Pushkarev, V. V.; Kovalchuk, V. I.; d'Itri, J. L., "Probing defect sites on the CeO2 surface with dioxygen," *Journal of Physical Chemistry B* **2004** 108, (17), 5341-5348.
63. Lunsford, J. H.; Yang, X. M.; Haller, K.; Laane, J.; Mestl, G.; Knozinger, H., "IN-SITU RAMAN-SPECTROSCOPY OF PEROXIDE IONS ON BA/MGO CATALYSTS," *Journal of Physical Chemistry* **1993** 97, (51), 13810-13813.
64. Cheng, Z.; Abernathy, H.; Liu, M., "Raman Spectroscopy of Nickel Sulfide Ni_3S_2," *Journal of Physical Chemistry C* **2007** 111, (49), 17997-18000.
65. Zhang, H. B.; Schrader, G. L., "CHARACTERIZATION OF A FUSED IRON CATALYST FOR FISCHER-TROPSCH SYNTHESIS BY INSITU LASER RAMAN-SPECTROSCOPY," *Journal of Catalysis* **1985** 95, (1), 325-332.
66. Matsuo, Y.; Kostecki, R.; McLarnon, F., "Surface layer formation on thin-film LiMn2O4 electrodes at elevated temperatures," *Journal of The Electrochemical Society* **2001** 148, (7), A687-A692.
67. Uy, D.; O'Neill, A. E.; Weber, W. H., "UV Raman studies of adsorbed oxygen and NOx species on Pt/gamma-alumina catalysts," *Applied Catalysis B-Environmental* **2002** 35, (3), 219-225.
68. Waterhouse, G. I. N.; Bowmaker, G. A.; Metson, J. B., "Oxygen chemisorption on an electrolytic silver catalyst: a combined TPD and Raman spectroscopic study," *Applied Surface Science* **2003** 214, (1-4), 36-51.
69. Guzman, J.; Carrettin, S.; Corma, A., "Spectroscopic evidence for the supply of reactive oxygen during CO oxidation catalyzed by gold supported on nanocrystalline CeO2," *Journal of the American Chemical Society* **2005** 127, (10), 3286-3287.

70. Hess, C.; Lunsford, J. H., "Mechanism for NO2 storage in barium oxide supported on magnesium oxide studied by in situ Raman spectroscopy," *Journal of Physical Chemistry B* **2002** 106, (25), 6358-6360.
71. Wang, W.; Zhang, H. B.; Lin, G. D.; Xiong, Z. T., "Study of Ag/La0.6Sr0.4MnO3 catalysts for complete oxidation of methanol and ethanol at low concentrations," *Applied Catalysis B-Environmental* **2000** 24, (3-4), 219-232.
72. Spanier, J. E.; Robinson, R. D.; Zheng, F.; Chan, S. W.; Herman, I. P., "Size-dependent properties of CeO2-y nanoparticles as studied by Raman scattering," *Physical Review B* **2001** 64, (24), 8.
73. Soria, J.; Coronado, J. M.; Conesa, J. C., "Spectroscopic study of oxygen adsorption on CeO2/gamma-Al2O3 catalyst supports," *Journal of the Chemical Society-Faraday Transactions* **1996** 92, (9), 1619-1626.
74. Soria, J.; Martinezarias, A.; Conesa, J. C., "Spectroscopic Study of Oxygen-Adsorption as a Method to Study Surface-Defects on Ceo2," *Journal of the Chemical Society-Faraday Transactions* **1995** 91, (11), 1669-1678.
75. Zhan, Y. Y.; Cai, G. H.; Xiao, Y. H.; Zheng, Q.; Wei, K. M., "The relationship between structure and oxygen storage capacity of CexZr1-mO2 solid solution," *Spectroscopy and Spectral Analysis* **2007** 27, 2266-2269.
76. Zha, S.; Moore, A.; Abernathy, H.; Liu, M., "GDC-Based Low-Temperature SOFCs Powered by Hydrocarbon Fuels," *Journal of The Electrochemical Society* **2004** 151, (8), A1128-A1133.
77. He, H. P.; Gorte, R. J.; Vohs, J. M., "Highly sulfur tolerant Cu-ceria anodes for SOFCs," *Electrochemical and Solid State Letters* **2005** 8, (6), A279-A280.
78. Ye, X. F.; Huang, B.; Wang, S. R.; Wang, Z. R.; Xiong, L.; Wen, T. L., "Preparation and performance of a Cu-CeO2-ScSZ composite anode for SOFCs running on ethanol fuel," *Journal of Power Sources* **2007** 164, (1), 203-209.
79. Qiao, J. S.; Sun, K. N.; Zhang, N. Q.; Sun, B.; Kong, J. R.; Zhou, D. R., "Ni/YSZ and Ni-CeO2/YSZ anodes prepared by impregnation for solid oxide fuel cells," *Journal of Power Sources* **2007** 169, (2), 253-258.
80. Molenda, J.; Swierczek, K.; Zajac, W., "Functional materials for the IT-SOFC," *Journal of Power Sources* **2007** 173, 657-670.
81. Zhang, Y.; Kang, Z.; Dong, J.; Abernathy, H.; Liu, M., "Self-assembly of cerium compound nanopetals via a hydrothermal process: Synthesis, formation mechanism and properties," *Journal of Solid State Chemistry* **2006** 179, (6), 1733-1738.
82. Zhang, Y. Synthesis and characterization of nanostructured electrodes for solid state ionic devices Ph.D., Georgia Institute of Technology, Atlanta, GA, 2006.
83. Choi, Y. M.; Abernathy, H.; Chen, H.-T.; Lin, M. C.; Liu, M., "Characterization of O_2-CeO_2 interactions using in situ Raman spectroscopy and first-principle calculations," *ChemPhysChem* **2006** 7, (9), 1957-1963.
84. Yang, Z. X.; Woo, T. K.; Baudin, M.; Hermansson, K., "Atomic and electronic structure of unreduced and reduced CeO2 surfaces: A first-principles study," *Journal of Chemical Physics* **2004** 120, 7741-7749.
85. Choi, Y. M.; Lin, M. C.; Liu, M., "Computational study on the catalytic mechanism of oxygen reduction on $La_{0.5}Sr_{0.5}MnO_3$ in solid oxide fuel cells," *Angewandte Chemie, International Edition* **2007** 46, (38), 7214-7219.

86. Chick, L. A.; Pederson, L. R.; Maupin, G. D.; Bates, J. L.; Thomas, L. E.; Exarhos, G. J., "GLYCINE NITRATE COMBUSTION SYNTHESIS OF OXIDE CERAMIC POWDERS," *Materials Letters* **1990** 10, (1-2), 6-12.
87. Stair, P. C., In Situ Ultraviolet Raman Spectroscopy. In *In-Situ Spectroscopy in Heterogeneous Catalysis*, Haw, J. F., Ed. Wiley-VCH: Weinheim, 2002; pp 121-138.
88. Wang, S. R.; Kato, T.; Nagata, S.; Honda, T.; Kaneko, T.; Iwashita, N.; Dokiya, M., "Performance of a La0.6Sr0.4Co0.8Fe0.2O3-Ce0.8Gd0.2O1.9-Ag cathode for ceria electrolyte SOFCs," *Solid State Ionics* **2002** 146, (3-4), 203-210.
89. Wang, C. B.; Deo, G.; Wachs, I. E., "Interaction of polycrystalline silver with oxygen, water, carbon dioxide, ethylene, and methanol: In situ Raman and catalytic studies," *Journal of Physical Chemistry B* **1999** 103, (27), 5645-5656.
90. Fleischmann, M.; Hendra, P. J.; McQuilla, A. J., "RAMAN-SPECTRA OF PYRIDINE ADSORBED AT A SILVER ELECTRODE," *Chemical Physics Letters* **1974** 26, (2), 163-166.
91. Moskovits, M., "Surface-Roughness and Enhanced Intensity of Raman-Scattering by Molecules Adsorbed on Metals," *Journal of Chemical Physics* **1978** 69, (9), 4159-4161.
92. Kneipp, K.; Moskovits, M.; Kneipp, H., *Surface-enhanced raman scattering : physics and applications*. Springer: New York, 2006; Vol. 103, p 464.
93. Nikoobakht, B.; El-Sayed, M. A., "Surface-enhanced Raman scattering studies on aggregated gold nanorods," *Journal of Physical Chemistry A* **2003** 107, (18), 3372-3378.
94. Aroca, R., *Surface Enhanced Vibrational Spectroscopy*. Wiley: Hoboken, NJ, 2006; p 233.
95. Nie, S. M.; Emery, S. R., "Probing single molecules and single nanoparticles by surface-enhanced Raman scattering," *Science* **1997** 275, (5303), 1102-1106.
96. Hering, K.; Cialla, D.; Ackermann, K.; Dorfer, T.; Moller, R.; Schneidewind, H.; Mattheis, R.; Fritzsche, W.; Rosch, P.; Popp, J., "SERS: a versatile tool in chemical and biochemical diagnostics," *Analytical and Bioanalytical Chemistry* **2008** 390, (1), 113-124.
97. Zhang, X. Y.; Zhao, J.; Whitney, A. V.; Elam, J. W.; Van Duyne, R. P., "Ultrastable substrates for surface-enhanced Raman spectroscopy: Al2O3 overlayers fabricated by atomic layer deposition yield improved anthrax biomarker detection," *Journal of the American Chemical Society* **2006** 128, (31), 10304-10309.
98. Liu, Y.; Zha, S.; Liu, M., "Novel nanostructured electrodes for solid oxide fuel cells fabricated by combustion chemical vapor deposition (CVD)," *Advanced Materials (Weinheim, Germany)* **2004** 16, (3), 256-260.
99. Liu, Y. Fabrication of nanostructured electrodes and interfaces using combustion CVD. Georgia Institute of Technology, Atlanta, GA, 2006.
100. Braun, G.; Pavel, I.; Morrill, A. R.; Seferos, D. S.; Bazan, G. C.; Reich, N. O.; Moskovits, M., "Chemically patterned microspheres for controlled nanoparticle assembly in the construction of SERS hot spots," *Journal of the American Chemical Society* **2007** 129, (25), 7760-+.
101. Emory, S. R.; Jensen, R. A.; Wenda, T.; Han, M. Y.; Nie, S. M., "Re-examining the origins of spectral blinking in single-molecule and single-nanoparticle SERS," *Faraday Discussions* **2006** 132, 249-259.

102. Kudelski, A., "Some aspects of SERS temporal fluctuations: analysis of the most intense spectra of hydrogenated amorphous carbon deposited on silver," *Journal of Raman Spectroscopy* **2007** 38, 1494-1499.
103. Naik, R. R.; Stringer, S. J.; Agarwal, G.; Jones, S. E.; Stone, M. O., "Biomimetic synthesis and patterning of silver nanoparticles," *Nature Materials* **2002** 1, (3), 169-172.
104. Kucharczyk, B.; Tylus, W., "Effect of Pd or Ag additive on the activity and stability of monolithic LaCoO3 perovskites for catalytic combustion of methane," *Catalysis Today* **2004** 90, (1-2), 121-126.
105. Gulari, E.; Guldur, C.; Srivannavit, S.; Osuwan, S., "Co oxidation by silver cobalt composite oxide," *Applied Catalysis a-General* **1999** 182, (1), 147-163.
106. Chang, F. M.; Jansen, M., "Syntheses and Crystal-Structure of Ag2mno4," *Zeitschrift Fur Anorganische Und Allgemeine Chemie* **1983** 507, (12), 59-65.
107. Li, L. Y.; King, D. L., "Synthesis and characterization of silver hollandite and its application in emission control," *Chemistry of Materials* **2005** 17, (17), 4335-4343.
108. Xu, G.; Tazawa, M.; Jin, P.; Nakao, S., "Surface plasmon resonance of sputtered Ag films: substrate and mass thickness dependence," *Applied Physics a-Materials Science & Processing* **2005** 80, (7), 1535-1540.
109. Takeguchi, T.; Kani, Y.; Yano, T.; Kikuchi, R.; Eguchi, K.; Tsujimoto, K.; Uchida, Y.; Ueno, A.; Omoshiki, K.; Aizawa, M., "Study on steam reforming of CH₄ and C₂ hydrocarbons and carbon deposition on Ni-YSZ cermets," *Journal of Power Sources* **2002** 112, (2), 588.
110. Lin, Y. B.; Zhan, Z. L.; Liu, J.; Barnett, S. A., "Direct operation of solid oxide fuel cells with methane fuel," *Solid State Ionics* **2005** 176, (23-24), 1827-1835.
111. Atkinson, A.; Barnett, S.; Gorte, R. J.; Irvine, J. T. S.; McEvoy, A. J.; Mogensen, M.; Singhal, S. C.; Vohs, J., "Advanced anodes for high-temperature fuel cells," *Nature Materials* **2004** 3, (1), 17.
112. Finnerty, C. M.; Coe, N. J.; Cunningham, R. H.; Ormerod, M. R., "Carbon formation on and deactivation of nickel-based/zirconia anodes in solid oxide fuel cells running on methane," *Catalysis Today* **1998** 46, (2-3), 137.
113. McIntosh, S.; He, H.; Lee, S.-I.; Costa-Nunes, O.; Krishnan, V. V.; Vohs, J. M.; Gorte, R. J., "An Examination of Carbonaceous Deposits in Direct-Utilization SOFC Anodes," *Journal of The Electrochemical Society* **2004** 151, (4), 604-608.
114. Gorte, R. J.; Kim, H.; Vohs, J. M. In *Novel SOFC anodes for the direct electrochemical oxidation of hydrocarbon*, London, 2002; Elsevier Science B.V.: London, 2002; p 10.
115. Costa-Nunes, O.; Vohs, J. M.; Gorte, R. J., "A study of direct-conversion SOFC with n-butane at higher fuel utilization," *Journal of The Electrochemical Society* **2003** 150, (7), 858-863.
116. McIntosh, S.; Vohs, J. M.; Gorte, R. J., "Role of hydrocarbon deposits in the enhanced performance of direct-oxidation SOFCs," *Journal of The Electrochemical Society* **2003** 150, (4), 470-476.
117. McIntosh, S.; Gorte, R. J., "Direct hydrocarbon solid oxide fuel cells," *Chemical Reviews* **2004** 104, (10), 4845.
118. Fergus, J. W., "Metallic interconnects for solid oxide fuel cells," *Materials Science and Engineering A* **2005** 397, (1-2), 271.

119. Hilpert, K.; Das, D.; Miller, M.; Peck, D. H.; Weiss, R., "Chromium vapor species over solid oxide fuel cell interconnect materials and their potential for degradation processes," *Journal of The Electrochemical Society* **1996** 143, (11), 3642-3647.
120. Yokokawa, H.; Horita, T.; Sakai, N.; Yamaji, K.; Brito, M. E.; Xiong, Y. P.; Kishimoto, H., "Thermodynamic considerations on Cr poisoning in SOFC cathodes," *Solid State Ionics* **2006** 177, (35-36), 3193-3198.
121. Jiang, S.-P.; Zhang, J.-P.; Apateanu, L.; Foger, K., "Deposition of chromium species on Sr-doped LaMnO3 cathodes in solid oxide fuel cells," *Electrochemistry Communications* **1999** 1, (9), 394.
122. Matsuzaki, Y.; Yasuda, I., "Dependence of SOFC Cathode Degradation by Chromium-Containing Alloy on Compositions of Electrodes and Electrolytes," *Journal of The Electrochemical Society* **2001** 148, (2), 126-131.
123. Jiang, S. P.; Zhang, J. P.; Apateanu, L.; Foger, K., "Deposition of chromium species at Sr-doped LaMnO3 electrodes in solid oxide fuel cells. I. Mechanism and kinetics," *Journal of The Electrochemical Society* **2000** 147, (11), 4013.
124. Paulson, S. C.; Birss, V. I., "Chromium poisoning of LSM-YSZ SOFC catho des I. detailed study of the distribution of chromium species at a porous, single-phase cathode," *Journal of The Electrochemical Society* **2004** 151, (11), 1961-1968.
125. Tucker, M. C.; Kurokawa, H.; Jacobson, C. P.; De Jonghe, L. C.; Visco, S. J., "A fundamental study of chromium deposition on solid oxide fuel cell cathode materials," *Journal of Power Sources* **2006** 160, (1), 130-138.
126. Systems, G. E. H. P. G. *Investigation of chromium effects in solid oxide fuel cells*; US DOE/NETL: Pittsburgh, PA, 2006.
127. Scheuerm.W; Ritter, G. J.; Schutte, C. J. H., "VIBRATIONAL SPECTRA OF STRONTIUM CHROMATE (SRCRO4) AND LEAD CHROMATE (PBCRO4)," *Zeitschrift Fur Naturforschung Part a-Astrophysik Physik Und Physikalische Chemie* **1970** A 25, (12), 1856-&.
128. Bae, J. M.; Steele, B. C. H., "Properties of pyrochlore ruthenate cathodes for intermediate temperature solid oxide fuel cells," *Journal of Electroceramics* **1999** 3, (1), 37-46.
129. Zhong, Z. M., "Bismuth ruthenate-based pyrochlores for IT-SOFC applications," *Electrochemical and Solid State Letters* **2006** 9, (4), A215-A219.
130. Kharton, V. V.; Tsipis, E. V.; Yaremchenko, A. A.; Frade, J. R., "Surface-limited oxygen transport and electrode properties of $La_2Ni_{0.8}Cu_{0.2}O_{4+\delta}$," *Solid State Ionics* **2004** 166, (3-4), 327 - 337.
131. Aguadero, A.; Alonso, J. A.; Fernandez-Diaz, M. T.; Escudero, M. J.; Daza, L., "In situ high temperature neutron powder diffraction study of La2Ni0.6Cu0.4O4+delta in air: Correlation with the electrical behaviour," *Journal of Power Sources* **2007** 169, (1), 17-24.
132. Haanappel, V. A. C.; Rutenbeck, D.; Mai, A.; Uhlenbruck, S.; Sebold, D.; Wesemeyer, H.; Rowekamp, B.; Tropartz, C.; Tietz, F., "The influence of noble-metal-containing cathodes on the electrochemical performance of anode-supported SOFCs," *Journal of Power Sources* **2004** 130, (1-2), 119-128.
133. Tedmon, C. S.; Spacil, H. S.; Mitoff, S. P., "CATHODE MATERIALS AND PERFORMANCE IN HIGH-TEMPERATURE ZIRCONIA ELECTROLYTE FUEL CELLS," *Journal of The Electrochemical Society* **1969** 116, (9), 1170-&.

134. Camaratta, M.; Wachsman, E., "Silver-bismuth oxide cathodes for IT-SOFCs; Part I - Microstructural instability," *Solid State Ionics* **2007** 178, (19-20), 1242-1247.
135. Sasaki, K.; Hosoda, K.; Lan, T. N.; Yasumoto, K.; Wang, S.; Dokiya, M., "Ag-Zr(SC)O-2 cermet cathode for reduced temperature SOFCs," *Solid State Ionics* **2004** 174, (1-4), 97-102.
136. Wang, Y. S.; Wang, S. R.; Wang, Z. R.; Wen, T. L.; Wen, Z. Y., "Performance of Ba0.5Sr0.5Co0.8Fe0.2O3-delta-CGO-Ag cathode for IT-SOFCs," *Journal of Alloys and Compounds* **2007** 428, (1-2), 286-289.
137. Xia, C.; Zhang, Y.; Liu, M., "Composite cathode based on yttria stabilized bismuth oxide for low-temperature solid oxide fuel cells," *Applied Physics Letters* **2003** 82, (6), 901-903.
138. Uhlenbruck, S.; Tietz, F.; Haanappel, V.; Sebold, D.; Buchkremer, H. P.; Stover, D., "Silver incorporation into cathodes for solid oxide fuel cells operating at intermediate temperature," *Journal of Solid State Electrochemistry* **2004** 8, (11), 923-927.
139. Lee, K. T.; Manthiram, A., "Electrochemical performance of Nd0.6Sr0.4Co0.5Fe0.5O3-delta-Ag composite cathodes in intermediate temperature solid oxide fuel cells," *Journal of Power Sources* **2006** 160, (2), 903-908.
140. Abu-Zied, B. M., "Structural and catalytic activity studies of silver/chromia catalysts," *Applied Catalysis a-General* **2000** 198, (1-2), 139-153.
141. Robbins, D. J.; Day, P., "WHY IS SILVER CHROMATE RED - 4.2 K POLARIZED ELECTRONIC-SPECTRUM OF CHROMATE IN SILVER SULFATE," *Molecular Physics* **1977** 34, (3), 893-898.
142. Clark, R. J. H.; Dines, T. J., "Raman, Resonance Raman, and Infrared Spectroscopic Study of Silver(I) Chromate," *Inorganic Chemistry* **1982** 21, (10), 3585-3588.
143. Cieslakgolonka, M.; Raczko, M.; Staszak, Z., "Synthesis, Spectroscopic and Magnetic Studies of Chromium(Iii) Complexes Isolated from Invitro Reduction of the Chromium(Vi) Ion with the Main Cellular Reductants Ascorbic-Acid, Cysteine and Glutathione," *Polyhedron* **1992** 11, (19), 2549-2555.